University of Southampton

Faculty of Engineering and Physical Sciences

Engineering Materials & Surface Engineering

Mechanical Behaviour of 3D Printed Scaffolds for Bone Tissue Engineering

by

Cesar Faurat-Narkisian

ORCID ID 0000-0002-0149-9451

Thesis for the degree of Master of Philosophy

May 2023

University of Southampton

Abstract

Faculty of Engineering and Physical Sciences

Engineering Materials and Surface Engineering

Master of Philosophy

Mechanical Behaviour of 3D Printed Scaffolds for Bone Tissue Engineering

by

Cesar Faurat-Narkisian

Bone is the second most transplanted tissue in the world[1]. The current solution for bone grafts is autologous grafts in 80% of cases. As the tissue is harvested from the patient, there is limited availability. In up to 30% of cases, complications appear, like donor site morbidity or rejection. One answer to this problem is to create synthetic scaffold material with bone attributes. It should combine porosity, biocompatibility, stiffness, and strength similar to the surrounding tissues to avoid stress shielding. Here, the focus will be on fused filament fabrication (FFF). In this process, thermoplastic is extruded in a layer-by-layer manner creating complex architectures. FFF gradient scaffolds are known to improve cell seeding, help the differentiation of stem cells and allow the creation nutrient transport network. However, the impact of this complex architecture modifies the load paths inside the scaffold and the deformation mode, creating regions with different mechanical behaviours. These different regions are interesting to influence cell differentiation through mechanical stimulation. These parameters have not yet been studied, and this work will explore how the diameter of the filament, the spacing, the layer height and the offset between the filaments will impact the mechanical behaviour of FFF gradient scaffolds.

Micromechanical modelling is used on the different regions of a gradient scaffold to predict the mode and magnitude of microstructural deformation under compressive loading and the corresponding bulk mechanical response and properties. Predictions are compared to experimental data to validate the models and elucidate the key parameters for the design of bone scaffolds.

A systematic softening of the low porosity scaffolds compared to the models was observed. This phenomenon was attributed to the contact area between the filament which is overlooked in the micromechanical models. Even though the models are not yet able to capture the complexity of this architecture, two significant parameters were isolated. The first one is the porosity of the scaffold; it depends on the diameter, the layer height and the spacing. The second one is the contact area between the filaments; it is related to the diameter, the layer height, the position of the filaments and the material used. The contact area has been studied under the name of interlayer adhesion in general FFF. However, no studies have explored this parameter in the scaffold architecture studied. Therefore, the impact of the printing parameters on the contact area was of great interest, identifying the printing speed and the layer height as defining factors for the contact area. By modifying the diameter of the filaments, the spacing of the filaments, the layer height, the offset between the filaments, and the printing speed it is possible to fine tune the mechanical properties of FFF scaffolds for tissue engineering.

Table of Contents

Table of Tables

Table of Figures

Table of Figures

Table of Figures

Research Thesis: Declaration of Authorship

Print name: CESAR FAURAT-NARKISIAN

Title of thesis: Mechanical Behaviour of 3D Printed Scaffolds for Bone Tissue Engineering

I declare that this thesis and the work presented in it are my own and has been generated by me as the result of my own original research.

I confirm that:

1. This work was done wholly or mainly while in candidature for a research degree at this University;
2. Where any part of this thesis has previously been submitted for a degree or any other qualification at this University or any other institution, this has been clearly stated;
3. Where I have consulted the published work of others, this is always clearly attributed;
4. Where I have quoted from the work of others, the source is always given. With the exception of such quotations, this thesis is entirely my own work;
5. I have acknowledged all main sources of help;
6. Where the thesis is based on work done by myself jointly with others, I have made clear exactly what was done by others and what I have contributed myself;
7. None of this work has been published before submission

Signature: ..... Date: 08/05/2023

Acknowledgements

I would like to thank my supervisors Dr Andrew Hamilton and Prof. Martin Browne, for their help, support, and guidance on this project, helping me to become a better researcher. I would also like to thank Maria Stagno-Navarra for her help in this project.

Definitions and Abbreviations

ABS ..... Acrylonitrile Butadiene Styrene

AM ..... Additive Manufacturing

BTE ..... Bone Tissue Engineering

DBM ..... Decellularized Bone Matrix

DIC ..... Digital Image Correlation

FDM ..... Fused Deposition Modelling

FE ..... Finite Element

FEM ..... Finite Element Modelling

FEA ..... Finite Element Analysis

FFF ..... Fused Filament Fabrication

HAp ..... Hydroxy Apatite

HLH ..... High Low High

hMSCs ..... Human Mesenchymal Stem Cells

LHL ..... Low High Low

µ-CT ..... Micro-Computed Tomography

PCL ..... Poly(Capro) Lactone

PL ..... Point Load

PLA ..... Poly(Lactic) Acid

ROM ..... Rule Of Mixture

SEM ..... Scanning Electron Microscopy

TCP ..... TriCalcium Phosphate

Chapter 1 Introduction

The growing demand for engineered materials with tailored properties has spurred new developments in material design and manufacture. Controlling matter distribution within the component can produce materials with synergistic mechanical properties. Tissue engineering aims at restoring or regenerating a damaged tissue by combining cells with three-dimensional porous scaffolds[2]. Clinically, current therapies for bone replacement, such as autografts and allografts, are not yet completely successful, due to several drawbacks such as the donor site morbidity, the limited tissue availability and surgery complications, highlighting that this procedures are not always a possible option[3]. Optimizing and controlling the microarchitecture could lead to better implants when attempting to restore damaged tissues[2]. Additive manufacturing (AM) emerged in the past decade as an appealing tool to fabricate scaffolds with a controlled and completely interconnected pore network[4]. Woodpile structures are commonly used in biomedical scaffolds[5–8]. In the area of tissue engineering, woodpile scaffolds provide structural support for cell attachment, proliferation and differentiation[4,9]. These scaffolds require a certain degree of interconnected porosity to enable cellular processes, whereas their mechanical properties are of great interest as they should be capable to withstand mechanical loading[10,11]. The motivation and objectives of the research are presented below.

1.1 Motivation

According to the American National Cancer Institute, 3,450 new cases of primary bone cancer were diagnosed in the United-States, in 2018[89]. If no action is taken the cancer can metastasize. Already in 2008, 280,000 adults in the United States were living with metastatic cancer in bones. Surgery is the usual treatment for primary bone cancer[90]. Nowadays it is possible to avoid the removal of the entire limb and usually autologous grafts are used. Reconstructive surgery is still needed to regain limb function. It is common to harvest bone from the iliac crest to create the autologous graft which can be associated with donor site morbidity. Researchers tried to find a solution using synthetic grafts. However, due to mechanical properties too different from the bone they often fail[91]. Tissue engineering is an interesting alternative.

The purpose of Bone Tissue Engineering (BTE) is to induce the growth and regeneration of new bone tissue via the collaboration of cells, chemical signals, and scaffolds in which BTE scaffolds have

an important role. Voids are beneficial in biomedical applications where cell proliferation and growth need to be encouraged. The presence of voids results in properties that make them advantageous when compared to their homogeneous counterpart. In BTE, the scaffold acts as a structural matrix that gives support to the ingrowing tissue. Therefore, these scaffolds are required to have a certain degree of porosity and voids interconnectivity to favour cell growth.

Scaffolds should be biocompatible, bioresorbable and biodegradable, in order to be accepted by the body and gradually replaced by healthy tissue. As a result, different materials and fabrication methods have been investigated towards this end, leading to a deeper understanding of the geometrical, mechanical, and biological requirements associated with bone scaffolds. Many polymeric materials are biocompatible, have Young's moduli within the same range of porous cancellous bone and, most importantly, are bioresorbable. After being implanted, they will support cell growth and bone regeneration, and will be gradually replaced by new tissue, leaving no permanent implant once the healing process has finished[12]. Therefore, the associated risk of failure or infection is decreased. However, the mechanical properties of the scaffolds strongly (and inversely) dependent on porosity, that in turn must be appropriate to assure metabolic functions[13].

Different biomaterials processed in BTE scaffolds require different AM technologies. The performances of the obtained BTE scaffolds with different biomaterials, structures and additives also vary. Therefore, obtaining the optimal performance for BTE scaffolds fabricated by AM technologies is a research hotspot of BTE.

Control of the cellular micro-architecture inside the scaffolds is of great importance when developing BTE scaffolds[2]. Early studies suggest that the micro-architecture of scaffolds might influence cell attachment and orientation and induce different biological behaviours[14,15]. 3D scaffolds presenting a gradient structure could provide cues similar to the native environment and may guide stem cells to differentiate toward the lineage of the targeted tissue[4].

Additive manufacturing is frequently used to produce parts with a certain degree of porosity. AM techniques based on the extrusion of material are referred to as Fused Filament Fabrication (FFF), also commonly known as Fused Deposition Modelling (FDM). Parts fabricated with FFF are composed of an arrangement of extruded polymeric material. They are composed of a lattice

arrangement of filament materials, which in turn results in voids within the part. Examples of Fused Filament Fabricated parts are shown in Figure 1. The arrangement of material significantly influences the mechanical properties of the fabricated part. The porous inner structure has voids, saving material, reducing the weight of the printed component, and reducing the fabrication time. The dimension of the voids depends mainly on the spacing between the filaments. FFF allows the production of parts with tailored mechanical properties by controlling the distribution of matter throughout the part. By changing the spacing between the filaments, the porosity can be adjusted and therefore the mechanical properties. The porosity can be reduced or increased by controlling the distance between the filaments to fulfil the desired goal. This brings the filaments closer to each other or further apart, but the stacking of these invariably results in voids. Figure 1 shows examples of scaffolds with different spacings, resulting in different levels of porosity, and different arrangements of filaments (either aligned in the Z axis, the building direction, or offset). The effective properties of the scaffold will differ from those of the parent material due to the adjustable spacing and unavoidable porosity. For FFF, the temperature or the speed of the extruder can modify the mechanical properties of the scaffold[16–18]. This necessitates studying the mechanical properties of FFF parts to understand and predict the impact of these changes in spacing, porosity and printing parameters on the mechanical properties. While there has been significant effort in improving the manufacturing procedures to achieve a variety of complex shapes, the understanding of the mechanical properties of manufactured parts remains limited due to a lack of standards and the large number of variables affecting FFF process conditions and resulting properties. The modelling of these variables and their effects on the resulting microstructural features and mechanical properties have been attempted[19–21]. However, experimental validation is usually missing.

This work aims at providing an extensive overview of the parameters influencing the properties of porous parts, from the chosen scaffold geometry to the printing parameters used to produce them. Results from previous analytical micromechanical models and finite element models will be compared to experimental data. A combined approach based on numerical models will be used to predict the properties of gradient scaffolds. It will study the influence of porosity and filament bonding on the mechanical properties of the manufactured parts. The stiffness of the engineered scaffolds will be influenced by the spacing, the arrangement and the interlayer adhesion between the filaments. Processing parameters like printing speed, extruder temperature and layer height will be analysed and their influence on filament sintering will be assessed. The influence of each parameter on the stiffness will be discussed. Sets of parameters will be provided for rapid design and prototyping according to the required mechanical properties and porosity of the scaffold.

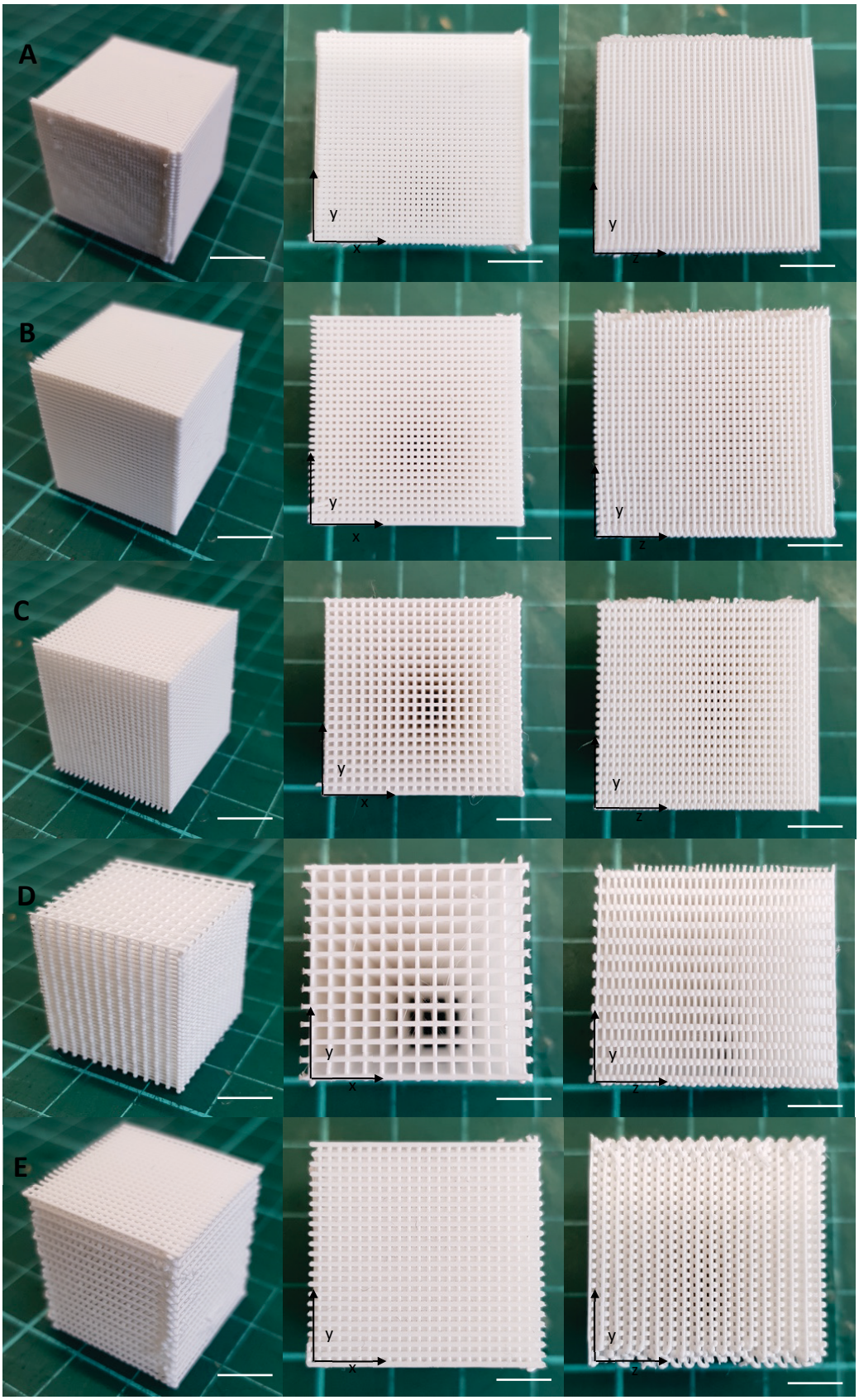

Figure 1 Cubic Scaffolds in thermoplastic polylactic acid (PLA): Isometric, top and side views of (A) aligned filaments with 54% porosity (B) 64% aligned (C) 73% aligned (D) 85% aligned (E) 73% offset. Scale bar: 10 mm

Chapter 2 Literature Review

2.1 Bone properties

The common goal of engineered bone scaffolds is to mimic the architecture and properties of bone. The architecture of the bone, its composition, its mechanical properties, and its healing process will be discussed successively. This section will address all the requirements to make a successful BTE scaffold.

2.1.1 Architecture

There are two main types of bone tissue: cortical bone and trabecular bone. The main difference between them is their porosity. This porosity difference creates a natural porosity gradient, which follows load paths (Figure 2), making the bone stiff and lightweight. Cortical bone has a porosity of 5 to 15%. It is found in the diaphysis of long bones surrounding trabecular bone located in the metaphysis and epiphyses. The metaphysis is the wide portion of long bones and where bone growth occurs. It is located between the diaphysis and epiphysis. The epiphysis is the expanded end of the long bones. Trabecular bone porosity ranges from 40 to 95%. The two types of bone are arranged according to load paths allowing a better distribution of the load inside the bone. The trabecular structure is composed of plate-like and rod-like struts[22]. The thickness of the tissue can vary from 300 µm in the healthy bone to 100 µm in the elderly bone[23]. Trabecular bone displays spatial heterogeneity in density and architecture, even within a given anatomic site. Its apparent density often characterizes the trabecular bone. It corresponds to the mass of the specimen divided by its apparent volume. Its value ranges from 0.05 to 1.1 g/cm^3. The bone tissue density (ratio of mass to volume of mineralized tissue) is approximately 2.0 g/cm^3 for cortical and trabecular bone. It does not vary a lot in the adult.

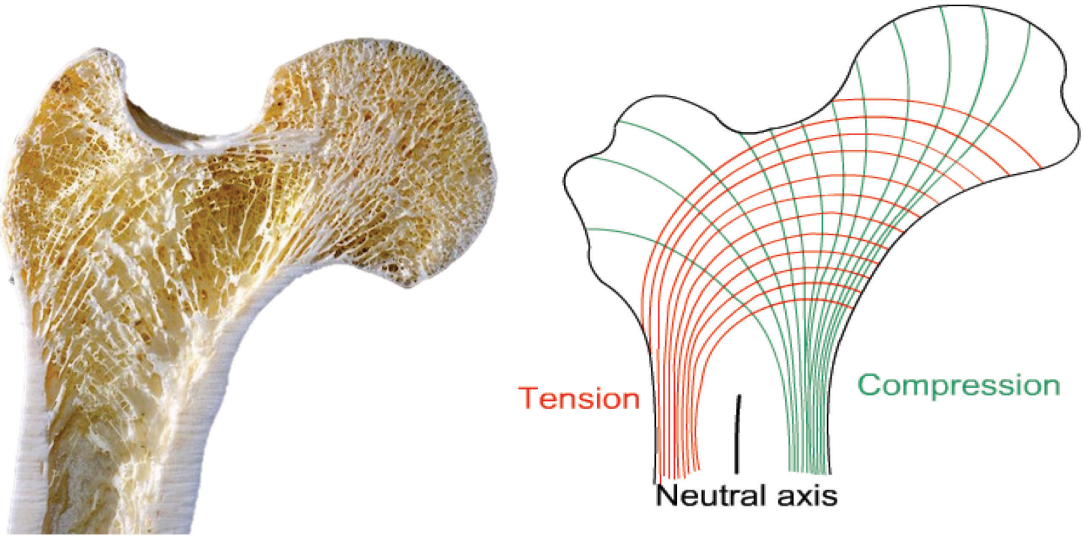

Figure 2 Femur head showing a natural porosity gradient. The gradient is the result of the load paths going through the femur, shown on the right[9].

2.1.2 Mechanical Behaviour

Bone properties vary according to the scale at which they are studied. At the millimetre scale (1-10 mm), bone tissue is anisotropic, depending on the direction of the measure the properties will be different. Bone tissue has higher strength, ability to withstand the stress of physical forces, and compressive moduli, ability to withstand changes in length when subjected to compressive loads, in the longitudinal direction compared to the radial and circumferential directions. Young's modulus can vary as much as 100-fold, and strength as 5-fold within a single epiphysis[24]. The modulus can range between 10 to 3,000 MPa. The strength which is linearly correlated to Young's modulus is generally two orders of magnitude smaller, range 0.1 to 30 MPa[25]. The variances observed can be explained by the apparent density.

At the millimetre scale, the strength of trabecular bone depends on the apparent density, its strength depends on its porosity. In a given anatomic site, the apparent density varies less than an order of magnitude, making the modulus and strength relations appear to be linear[26]. High-density trabecular bone, such as the human femoral neck, tends to have isotropic yield strains, uniform deformation. Ultimate strains, the strain corresponding to the maximum stress the material can withstand without failing, in trabecular bone appear to be isotropic and range from 1.0 to 2.5%. Yield strains, the limit between elastic and plastic behaviour, range from 0.70 to 0.77% in compression and from 0.65% to 0.71% in tension[26]. They can be considered relatively constant within a site but different among other sites. The differences in mechanical properties in

compression, tension and shear decrease with lower apparent density[27]. The Young's modulus can vary over tenfold among regions of the skeleton within the same individual. Trabecular bone is treated as a linear elastic material[28], the modulus is calculated from a linear or polynomial curve fit, and the yield point is defined by the 0.2% offset method, the amount of stress that will result in a plastic strain of 0.2%. Linear regression can be used when the range in apparent density is small[28,29]. Trabecular bone yields at a strain around 0.7% and can sustain compressive strains up to 50%. Cancellous bone strength is correlated with Young's Modulus. Its ultimate strength is correlated to yield strength. However, yield strain and ultimate strain are not correlated to apparent density[30]. The primary cause of cancellous bone anisotropy is the trabecular alignment. This impacts its mechanical properties. For example, if loading is applied transverse to the direction of alignment Young's modulus is 40 to 60% smaller. The same observation can be made for the ultimate strength, which is 30 to 45% smaller in this condition[31]**.** Bone strength is more sensitive to variation in the degree of mineralization of the tissue than to the variation in bone volume fraction[32].

2.1.3 Bone Healing Process

The healing process is subdivided into three overlapping phases[33]. During the initial inflammatory phase[34], the fracture zone is cleaned from dead material, activities that restore the blood supply are undertaken, and mesenchymal stem cells congregate. In the repair phase, additional tissue in the form of a fracture callus is formed[35]. With time, this callus turns from a soft callus to a hard callus eventually made of bone. In the final remodelling phase, the superfluous bone material is resorbed, leaving behind an intact healed bone. Despite the complexity of the healing process[36], bone healing can be described as a mechanobiological process[35]. Different to remodelling, the mechanical stimulus does not influence cell action, but instead cell differentiation, by which cells are formed from stem cells in the first place[35]. Molecular analyses revealed that bending stimulation induced upregulation of genes involved in cartilage development and cartilage matrix components and downregulation of several genes involved in bone formation[37]. These findings indicate that mechanical stimulation can selectively promote osteogenic and chondrogenic development[1]. The local mechanical loads resulting from the bone architecture will help this differentiation phenomenon.

2.2 Bone tissue scaffolds

In case of a bone defect, two main types of grafts can be used: natural bone grafts (autologous and allogeneic) or synthetic bone grafts (ceramics, metals, polymers, and bioorganic ions). Their main advantages and drawbacks are reviewed in the next section.

2.2.1 Autografts, Allografts and Xenografts

The "current gold standard" for bone grafts in clinics is the autologous graft, also called autograft. The bone used for the transplant is obtained from the patient. The autograft has all the properties of natural bone and does not trigger an immune response as it comes from the patient. The main limitation of autografting is bone availability, as the tissue typically collected from the iliac crest or the mandibular symphysis is limited in size and quantity[38].

Human living donors provide allogeneic grafts. They can be made of cortical or cancellous bone, or they can be processed bone derivatives (demineralized bone matrix (DBM)). The major limitations of these grafts are their immunogenicity and their high failure rate due to histocompatibility. It causes the necrosis of osteoprogenitor cells and can lead to a viral transmission. Besides, cancellous grafts offer poor healing capabilities and lead to the formation of fibrous tissue. In preparing allogeneic grafts, the demineralized bone matrix has at least 40% of its mineral content removed by acid, leaving only collagen, non-collagenous proteins, and growth factors (GFs) resulting in inferior structural integrity and poor mechanical properties compared to the original bone tissue. As demineralized bone matrix cannot be used as a structural supportive graft due to its mechanical properties, it is more likely to be used as a scaffold for cell proliferation and osteogenesis as the cell environment will be like bone tissue. The prepared DBM will then be used as a graft. Furthermore, as for autografts, the supply is limited.

Xenografts come from nonhuman species. The antigenicity is more significant than for allografts requiring more sterile processing, which can result in reduced osteoinductive properties, induction of the osteogenesis. The sterilization of the xenografts prevents any viral transmission and increases shelf life. Also, harvesting bone tissue for the grafts is convenient due to the abundance of donors. The most common xenograft used in orthopaedic surgery is bovine based[39]. Usually, the incorporation is less successful compared to autografts or allogenic grafts, and the integration time is longer (around 16 weeks for non-xenografts and 57 weeks for xenografts)[39].

2.2.2 Engineered Scaffolds

To overcome the limitations of autografts, allografts and xenografts, researchers have focused their interest on engineered bone scaffolds. These synthetic grafts can overcome supply problems and immunogenicity with a structure and properties like natural bone. In the next section, different engineered bone scaffolds will be reviewed according to the requirements for an ideal bone graft.

2.2.2.1 Porous Structure

A bone biomimetic structure would be desirable. The adequate porous structure should be like the one found in trabecular bone, the porosity should be between 40 and 95%. The use of a gradient with high porosity would improve bone formation. It will allow to balance the mechanical and biological functions. In the following paragraphs, the recommended porous structures are discussed.

The pore size is essential in the scaffolds knowing that the average size of mesenchymal stem cells can vary between 10 to 30 µm[40]. The minimum pore size is generally considered 100 µm for bone ingrowth. Pores with a diameter of 300 µm are recommended for better vascularization and bone formation. Smaller pores support osteochondral differentiation due to low vessel formation[41]. The heterogeneity of the scaffold is essential for cellular proliferation. For this purpose, the use of a gradient of porosity is interesting. Different materials will achieve different porous structure and will give different level of control on the architecture.

Glass-ceramics as a scaffold with 90% porosity and well interlinked pores with a diameter of 100 – 300 µm boost the bone growth in 3D interlinked pores[92]. In a study from Woodard et al. macroporosity (250 – 350 µm) and microporosity (2 – 8 µm) were achieved in hydroxyapatite scaffolds. After implantation, lamellar and woven bone formation was observed which was not seen in HA scaffolds without microporosity[93]. The use of ceramics with interlinked pores, macroporosity and microporosity favours cell adhesion, proliferation and differentiation.

Metallic porous scaffolds can have an extensive range of pore sizes and porosity, from 40% to 70% with a pore size ranging from 361 µm up to 896 µm. However, cellular growth has been observed with 50 µm holes on titanium triangular plates in a non-load-bearing case[42]. Furthermore, the shape of the pores can be optimized according to the related use of the scaffold[43,44].

Polymer scaffolds cover a wide variety of porosity. When they are manufactured by fused deposition modelling (FDM), their porosity can be designed to suit the requirements of the grafts. Grémare *et al.* .[45] demonstrated the possibility to print PLA scaffolds with pore size from several hundred micrometres to a few micrometres matching precisely the overall geometry of the patient's bone defect. Three pore sizes were printed (150, 200, 250 µm) with no significant differences in cell proliferation and adhesion between them. The three pore sizes had all high cell viability, and the cells had spread throughout the mesh and moved in the pores of PLA scaffolds. Gregor *et al.* .[46] printed two different designs: one type of PLA scaffold had a porosity of 30% with overlapping struts avoiding vertical gaps (ST1). The other one had a porosity of 50%, to test the cell attachment to individual fibres (ST2). The pore size ranged from 350 µm for ST1 and 700 µm for ST2 scaffolds[46], see figure 3. On day 7, there were visible cells "bridging" the gaps between individual fibres on ST1 scaffolds. On ST2 scaffolds, cells were grouped around the contact points between the layers; no bridging was observed. On day 14, fibres were confluently covered by cells, and the gaps between fibres were filled in both scaffolds. Cavo and Scaglione[47] found with the help of computational modelling that pores of the diameter 600 µm and interpore distances of 300 µm with 90° oriented interconnected pores formed scaffolds with a porosity of 52% were the best among other tested scaffolds with no interconnection of pores and 45° orientated interconnection. They demonstrated a better proliferation of primary meniscus cells compared to 900 µm pores on day 3 and 5 after seeding. Hutmacher *et al.* .[48] printed PCL scaffold with FDM, Fused Deposition Modelling. They reached a porosity of 61%. They were implanted in critical-sized bone defects in rabbits calvarium. The formation of new bone was more significant in PCL scaffolds compared to a sham surgery control site, a procedure performed as a control and that is similar to but omits a key therapeutic element of the treatment under investigation. Only the porous area of the scaffold allowed the regeneration of bone[47]. Scaffolds with a graduated porosity of 60% porosity in the middle and 15% in the proximal region were designed to mimic the anatomical porosity of femoral head closely. These scaffolds demonstrated excellent bone ingrowth eight weeks after implantation[49].

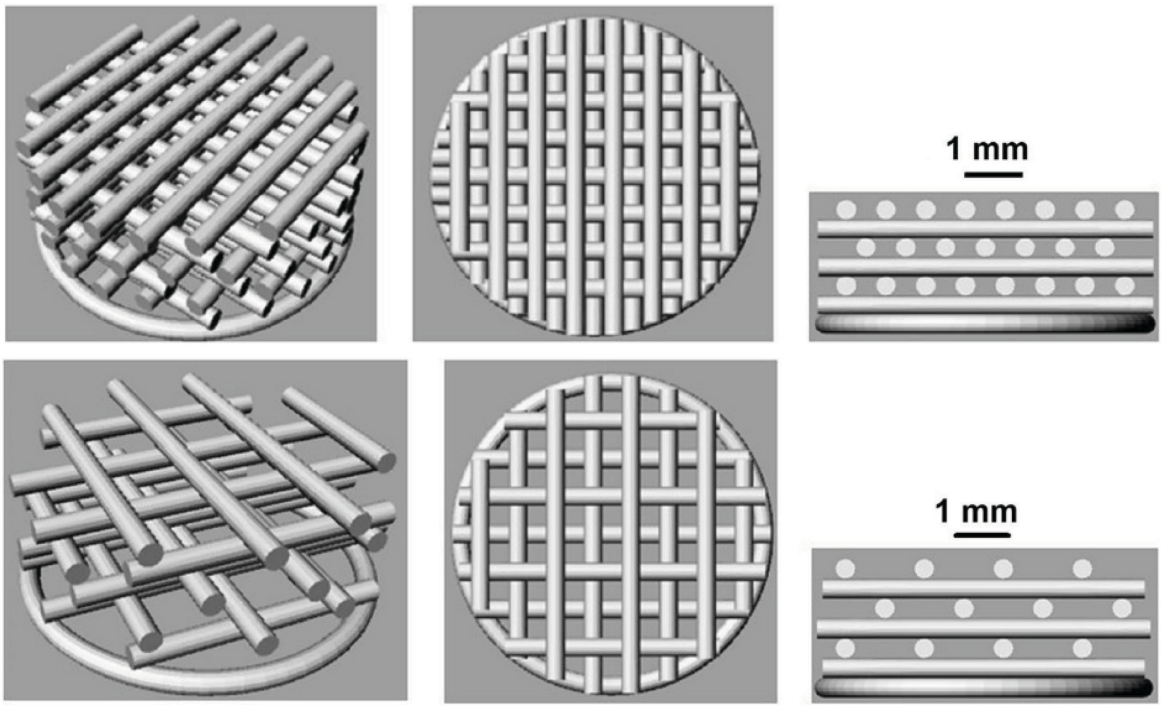

Figure 3 Gregor's scaffold design. At the top ST1 with a porosity of 30%. At the bottom ST2 with a porosity of 50%.

2.2.2.2 Mechanical Behaviour

Scaffolds can be made from a wide range of materials as seen in paragraph above: metals, plastics, ceramics, glasses, and composites. Their mechanical properties depend on two separate sets of parameters. The parameters that are describing the geometric structure of the scaffold, size and shape of the pores[50]. The parameters which describe the intrinsic properties of the material. Solid materials have mechanical values laying in specific characteristic ranges. Figure 4 shows Young's moduli plotted against the characteristic densities of a range of materials. Metals have high moduli and high stiffness. Engineering ceramics like alumina are stiffer than metals while being less dense on average. Polymers and elastomers, as they are made of light atoms, have the lowest densities of all solids and are less stiff than the other classes of engineering materials.

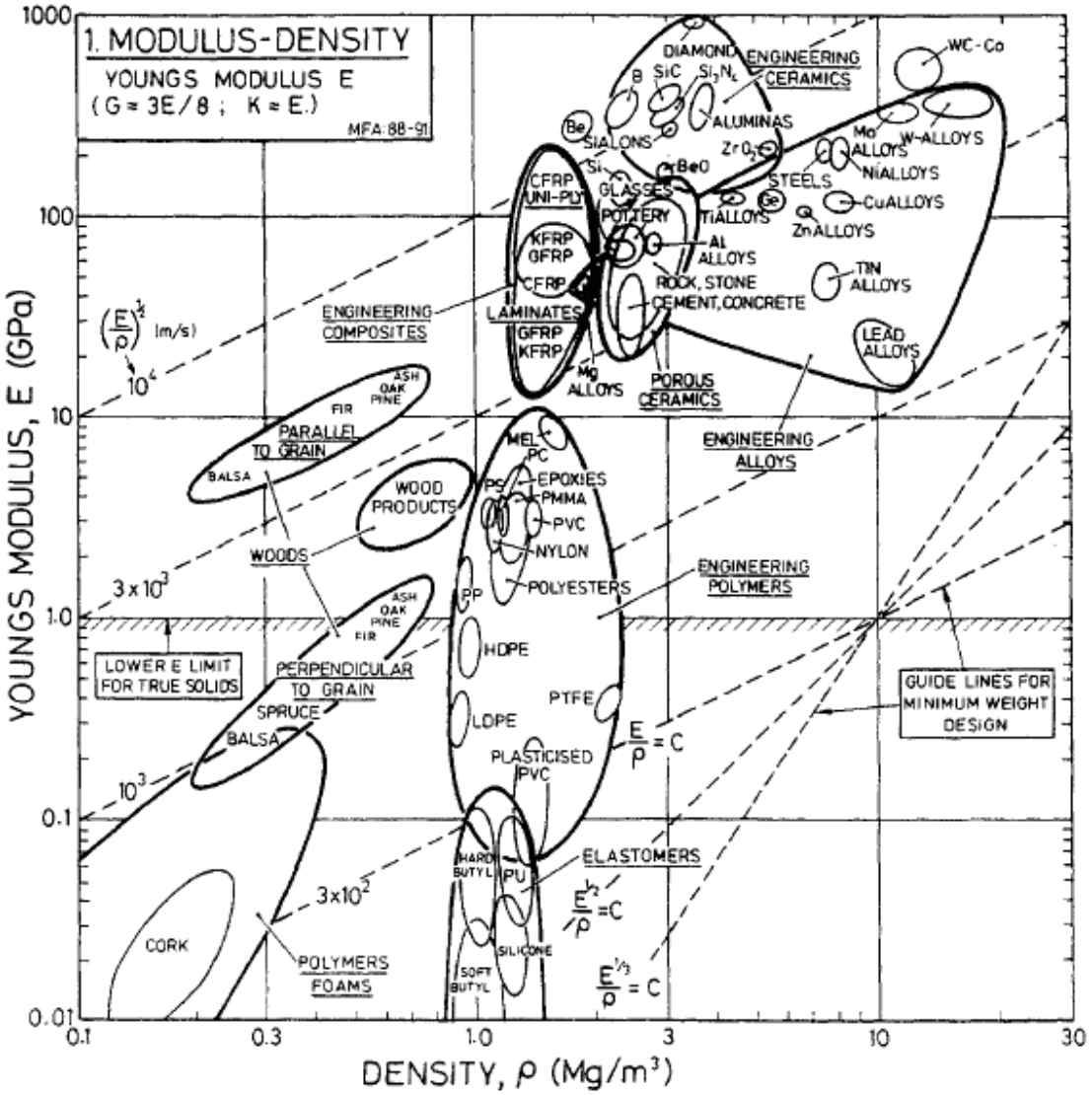

Figure 4 Chart showing Young's modulus E_s, and density, ρ_s, for materials. Each material class occupies a particular field on the chart. Ege et al. Experimental estimation of viscoelastic properties of multilayer damped plates in broad-band frequency range.

The mechanical properties of the scaffold must match bone properties at the implantation site. It is important to allow the mechanical stimulation of the cells to encourage new bone growth and to avoid stress shielding, resorption of the bone due to a lack of mechanical stimulation[51]. Ceramics usually have weak mechanical properties. Calcium sulphate has a weak internal strength. Calcium phosphate mechanical properties depend on the Ca/P ratio. For example, hydroxyapatite (HAp) has mechanical properties close to the cancellous bone, but they decrease by 30 to 40% after time[48], which is desirable for biodegradable implants. Tricalcium phosphates are also ceramics but have weak mechanical properties. However, biphasic calcium phosphate, by modulating the concentration of HAp and TCP, can increase mechanical properties. Due to the presence of HAp,

they are only used as coating[52]. The calcium phosphate cements are mechanically supportive, but they have low bending strength[53].

Metallic porous materials, such as titanium or tantalum, exhibit yield stress values close to cortical bone and higher than trabecular bone (92 to 276 MPa)[43]. In porous structures, when they are compressed, they start to buckle and the resistance to compression remains constant until densification, when the layers are in contact. This phenomenon is observed as a plateau on the stress-strain curves. The plateau stress is also higher compared to the compressive strength values reported for trabecular bone and cortical bone. The observed elastic moduli, between 3.2 and 6.4 GPa, are in the range of high density trabecular and cortical bone[54], Table 1. These materials combine a low elastic modulus, close to trabecular and cortical bone, with high yield stress and compressive strength. The relatively low elastic modulus prevents stress shielding and then bone resorption and implant failure[43]. However, they do not physically and mechanically degrade to allow new bone tissue to form and replace the scaffold.

Polymer scaffolds, despite reasonable control over porosity, have low mechanical properties, Table 1. The 30% porosity scaffolds made by Gregor *et al.* had a 45.61 MPa Young's Modulus, which decreased to 29.96 MPa for a porosity of 50%. The scaffolds made by Elomaa *et al.* achieving porosities of 55% 60% and 66% had, respectively, mechanical strengths of 13.25, 9.47 and 5.57 MPa[55]. PCL scaffold with a porosity of 61% reached a compressive strength of 41.9 MPa and which dropped to 29.4 MPa when soaked in a phosphate buffer solution [45], allowing a partial degradation of the PCL[45]. The scaffolds with a graduated porosity of 60% porosity in the middle and 15% in the proximal region, had a compressive strength of 2.2 MPa and 9.5 MPa, respectively[49]. These mechanical properties, among the lowest reported for scaffold materials, only match trabecular bone with the highest porosity reducing the area of use of these scaffolds.

Table 1 Young's Modulus in MPa for scaffolds used as bone grafts made of different materials.

Material	**Young's Modulus (MPa)**
Cortical Bone	1,150 to 15,000
Cancellous Bone	28 to 63[93]
Metals: Titanium, Tantalum	3,200 to 6,400

Ceramics: Alumina scaffold	2,000 to 5,000 (in compression)
Polymers: PLA, PCL	2.2 to 45.6

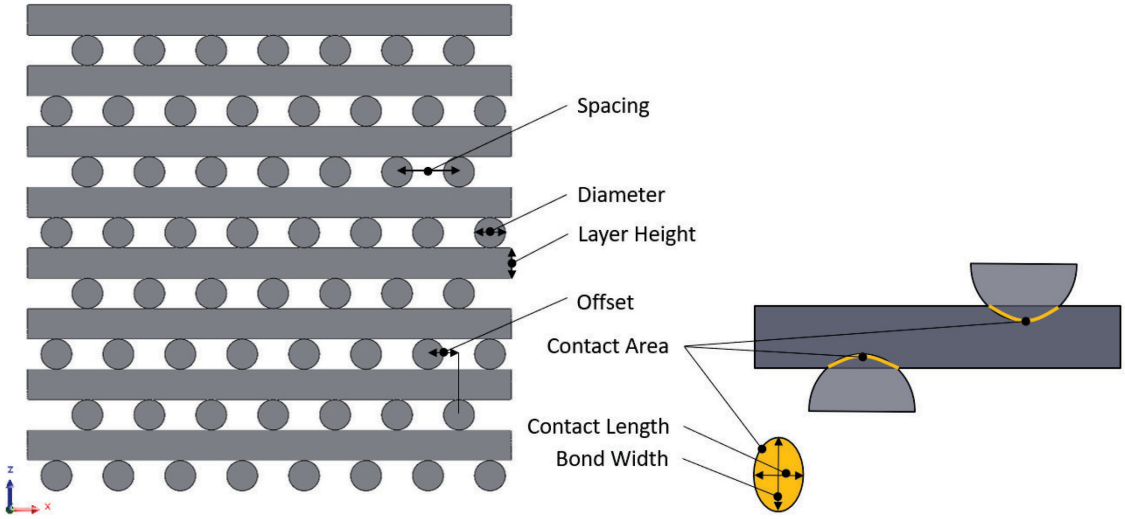

Figure 5 Visual representation of the different terms used to describe the porous structure of FDM scaffolds.

2.3 Gradient Scaffolds

Scaffolds with a graduated porosity of 60% porosity in the middle and 15% in the proximal region were designed to mimic the anatomical porosity of femoral head closely. These scaffolds demonstrated excellent bone ingrowth eight weeks after implantation[49].

As mentioned above, the use of gradient scaffolds is highly desirable. It helps balance mechanical and biological properties allowing to have an overall higher stiffness while maintaining high porosity and a variety of pore sizes across the scaffold. The use of gradient scaffolds is inspired by the observation of trabecular bone where a gradient is present to help maintain high stiffness and porosity. The following paragraphs will explore the use of gradient scaffolds in bone tissue engineering.

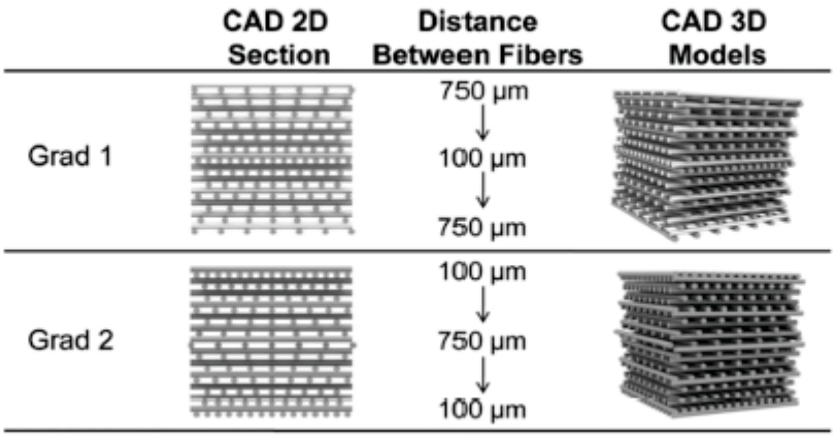

Figure 6 Gradient scaffolds design from Sobral et al[3] Grad 1 has high porosity at the edges and low porosity at the center. Grad 2 has low

One way to balance the mechanical and biological properties of scaffolds is to design a scaffold with a gradient. Sobral *et al.* .[2] investigated the mechanical and biological benefits of two different types of gradient porosity scaffolds compared to uniform aligned scaffolds which are shown in Figure 6.The scaffolds were manufactured through the extrusion of PCL, a thermoplastic, filaments with a circular cross-section deposited in layers with a given spacing separating the filaments and with subsequent layers oriented orthogonally. Human osteosarcoma cells were used to determine cell seeding efficiency and distribution. The scaffolds were as expected, and the lower porosity, 31%, scaffold with aligned filaments had a higher Young's modulus than all other scaffolds. Gradient scaffold with low porosity on the edges and high porosity at the centre had a slightly higher Young's modulus than the one with high porosity at the edges and low at the centre. However, due to the deviation of the data, this difference was not significant. Twelve hours after cell seeding in static conditions, fewer cells were found in the wells, meaning less cells fell through without attaching, in the case of gradient scaffolds compared to uniform scaffolds. The gradient scaffolds had a significantly increased seeding efficiency compared to the uniform aligned scaffold with the gradient with high porosity outwards performing best (seeding efficiency of 70%)[2].

Di Luca *et al.* .[4] also investigated PCL FDM manufactured gradient and uniform aligned scaffolds but focused their study on osteogenic differentiation. Their gradient scaffolds consisted of four regions of different gaps between extruded filaments, which ranged from 500 to 1,100 µm. The uniform aligned scaffolds had gaps of 500 µm and 1,100 µm. The gradient scaffold was found to have greater cell differentiation into osteoblasts, shown by a 12 times increase in the activity of the alkaline phosphatase (ALP)[4].

From the studies mentioned above, it can be concluded that a gradient scaffold significantly improves the biological properties of bone scaffolds and efforts should be placed upon understanding the relationship between their mechanical properties and their biological properties.

2.4 Additive Manufacturing

Scaffolds act as a support material for the regeneration or replacement of tissues and organs, allowing the cells to attach and grow. A controlled and heterogeneous structure can help to optimize cellular growth. 3D printing allows to control characteristics, like internal architecture, porosity, and interconnectivity, to fulfil the different requirements, discussed above, for cell proliferation and to create an architecture like the native tissue. In this section, the different 3D printing techniques will be assessed.

2.4.1 Stereolithography

Stereolithography (SLA) is based on a UV Laser curing liquid resin into a hardened material layer by layer. It requires photoinitiators, and they can have toxic effects on the cells. It benefits from a high resolution 5-300 µm, superior accuracy and the smoothest surface finish[56]. Various techniques are regrouped in this category as two-photon polymerization, holography, and visible light-based SLA. It can print a different kind of materials as chitosan, when blended with photoiniators, its concentration improved the cell viability but reduce the mechanical properties[57]. A scaffold made of three arm star PCL with photoactive end groups exhibited a metabolic activity similar to the control group (tissue culture polystyrene)[56]

2.4.2 Selective Laser Sintering

Selective laser sintering (SLS) uses high powered carbon dioxide laser to heat and fuse small particles of polymer powder. They are mainly used with PCL, calcium phosphate or composites of polymer and bioceramic. The prints are highly detailed and with thin walls, hundreds of microns (700 µm)[58]. One of the main problems is the shrinking or warping of the scaffold due to thermal distortion. Natural polymers cannot be used due to the high temperature as they would degrade[59].

PCL is an excellent material for this technique due to its low melting temperature 59-64°C and a glass-transition temperature of - 60°C, transition from a rigid state to a more flexible state. It is

easily processable[58]. PCL scaffolds demonstrated good bone ingrowth and cartilage ingrowth on the articular surface[60].

2.4.3 Powder Bed Inkjet

Powder bed inkjet works with droplets of dilute solutions of biomaterials. They are dispensed driven either by thermal or piezoelectric processes into a powder bed. The ink acts as a binder solution to a bulk material positioned within the powder bed. The powder can be heated between 100 to 350°C. The main problems are the effect of shear or thermal stresses on natural polymer inks and inconsistent droplet volume[61]. Piezoelectric inkjet offers the ability to print a large variety of materials with the choice of polar or non-polar solvents. However, the material must be in a powder form. PCL either pure of 50:50 βTCP with channels around 1 mm demonstrated *in vitro higher* cell concentrations than the other scaffolds and highest level of collagen formation[62].

2.4.4 Extrusion Printing

Extrusion printing regroups two main techniques: the extrusion of molten material, also called fused deposition modelling (FDM) or Fused Filament Fabrication (FFF) and the extrusion of gelling liquid material. FFF works with thermoplastics as deposited as long filament, as shown in Figure 7. The strength of the structure relies on the bonding between the deposited layers. In the extruder, the filament is melted at a predetermined temperature and is extruded through the nozzle. For this technique, PLA and PCL are biocompatible, biodegradable and medical-grade sources are approved for use in the body by the FDA[11]. The accuracy and shape of the final structure depend on the speed at which the molten extruded filament cools down and solidifies after it has been dispensed.

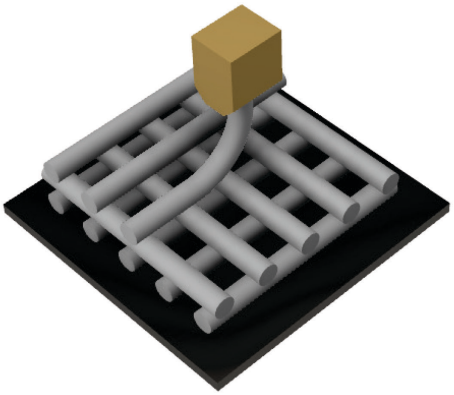

Figure 7 Scheme of extrusion printing: an extruder will deposit filaments of thermoplastic on a heat bed to create structure in three dimensions.

Quick processing and availability give to this technique a strong potential for BTE scaffold research despite its low resolution (around 200µm) and the specific requirement for the materials, using

thermoplastics[63]. However, a large variety of materials can be used, including natural and synthetic polymers. Extrusion printing offers a wide range of achievable compressive strength and porosity. In the scope of patient-tailored grafts, like other AM techniques discussed above, it is possible to use CT data to produce scaffolds that match the exact defect dimensions[51]. And it is also possible to incorporate bioactive molecules, improving the properties of the scaffold. Then, for the research on bone tissue engineered scaffolds, this method seems to be the most suitable, thanks to its versatility and preliminary results suggesting that 3D printed scaffolds have great potential.

2.5 Mechanical properties of lattice materials

The work of Ashby and Gibson relates structure to apparent properties by making use of the lattice geometry combined with the structural mechanics of elastic members constituting the lattice[64,65]. They performed a structural analysis on representative unit cells, of which the walls were modelled as beams. They derived analytical models for the apparent Young's modulus of honeycombs and for foams. The properties of the lattice depend on the intrinsic properties of the parent material, its relative density, structural parameters like the geometry of the lattice elements and the connectivity of the cell walls. Foams were modelled as a cubic array of structural elements, beams, and plates, for open- and closed-cell foams respectively.

Ashby and Gibson covered an extensive range of materials, including elastic polymers, in their study of cellular solids. Proportional relationships were used by Ashby and Gibson to calculate the relationship between Young's modulus (E*) and porosity with constants defined from fitting mechanical test data for different materials. The relationship for open cell foams is[50]:

$$E^* = C_1 \cdot E_s \cdot \left(\frac{\rho^*}{\rho_s}\right)^2 \qquad (1)$$

With the constant C_1 almost equal to 1, E_s the Young's modulus of the bulk material, ρ^* the density of the porous scaffolds, ρ_s the density of the scaffold if solid.

However, at large relative densities ($\rho^*/\rho_s > 0.3$) the beam concept breaks down. The cell walls are now so short that they axially yield before they bend, see Figure 8. Above this density, the material is better thought of as a solid with holes in it, not as a foam[50]. The scaffolds produced by Sobral et al.[2], shown in Figure 6, can be considered as an open-cell foam with mechanical properties modelled using relationships like Equation 1 due to their chosen geometry of the pores and the periodicity of the scaffold.

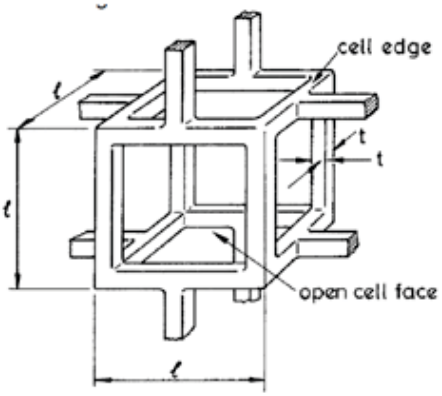

Figure 8 Unit cells. Open cell foam model from Ashby and Gibson. l is the length of the cell edge; t is the thickness of the cell edge. t << l [56].

Another common approach to predict the mechanical properties of porous materials is the use of Finite Element Model (FEM). This technique can model complex geometries, by incorporating boundary conditions. It is simple and widely available through software packages. Hendrikson et al. [66] used Finite Element Analysis to control the pore configuration and tune the mechanical properties to match the native tissue. The combination of FEM with microtomography provides information on the apparent stiffness and the permeability of scaffolds. However, CAD-based FEM could give a better prediction of the properties mentioned above, like the Young's modulus, the Ultimate yield strength [67–69]. FEMs require significant computational power and yet do not capture how mechanical signals results in specific cellular behaviour and differentiation [66] showing their limits. These limits will be studied later.

McKown et al. [70] studied stainless steel 316L SLM-fabricated lattices under compressive and blast loadings. For the struts aligned with the compressive loading direction, the failure mechanism observed was buckling. This is expected as slender structural elements aligned to the compressive loading led to buckling. For the lattice with no struts aligned to the loading direction, the failure was identified to be by progressive collapse. The blast loading tests showed that the lattice with the struts aligned to the loading direction, failed due to a shear band propagation at an angle of 45° caused by the buckling.

Similar lattices to McKown were fabricated by Karamooz et al. [71] with PLA by using fused filament fabrication (FFF). Finite element analysis (FEA) was used to predict the mechanical behaviour of truss lattices using two different models. One model was composed of 2D beam elements to represent the struts. The other model was composed of solid elements. Struts in the truss were built layer-by-layer, producing lattices with clear discontinuities at the surface of the trusses. The beams composing the FEMs had non-constant cross-sections. Both models showed good

agreement with the experimental data for stiffness. Moreover, they demonstrated the possibly to use FFF to produce parts with an inherent lattice structure that consist of alternating stacks of filaments.

Naghieh et al.[19] asserted that the fabrication of scaffolds is time consuming. Therefore, they tried to model the effect of layers penetration (interlayer adhesion) on the mechanical properties. They used FEM and experiments to compare their predictions. Figure 9(A) shows their model in the CAD software. Figure 9(B) shows their model after being meshed for finite element analysis.

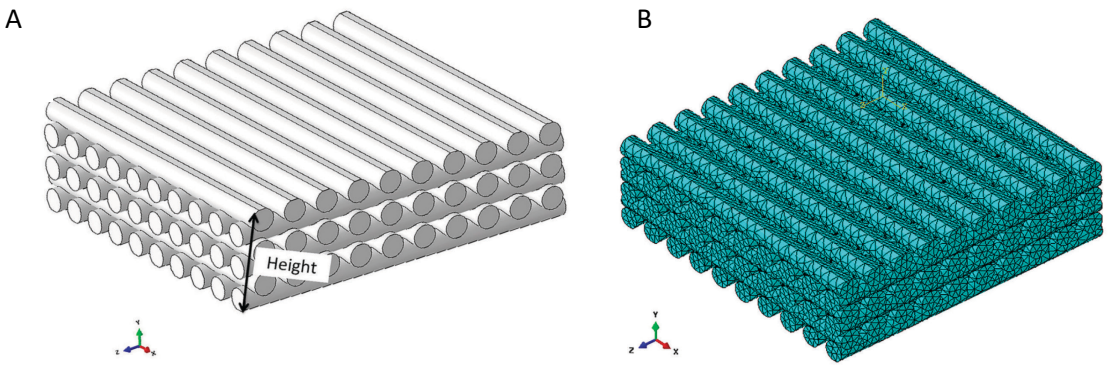

Figure 9 Naghieh et al. scaffold model (A) CAD Design (B) Mesh for Finite Element Analysis

From their work, they obtained a direct correlation between layer penetration and elastic modulus as a linear increase. It is possible to obtain higher Young's moduli with the same porosity by decreasing the size of the struts and therefore increasing the number of filaments. They also showed that the strut diameter impacted the layer penetration and the mechanical properties.

Norato and Wagoner [69] created bone scaffolds and studied the influence of the pore size on their stiffness. They modelled the scaffolds as rods stacked orthogonally in alternating directions see Figure 10. For the calculation of the stiffness, they used Finite Elements models and used numerical homogenisation assuming that what happens to one unit cell can be generalised to the scaffold using the periodicity and symmetry of the design. From their study they derived design charts to help achieve required stiffness by specifying the diameter (d), spacing (l) and overlap (a/d) of the rods making up the scaffolds. Norato and Wagoner managed to capture the functional relationships between the variables in Equation 6. Their design charts allow for their scaffolds to select the geometric and manufacturing parameters that render scaffolds with the desired moduli, porosity,

and pore size without the need of additional simulation or experimentation. Their scaffolds can then target different implant sites[69].

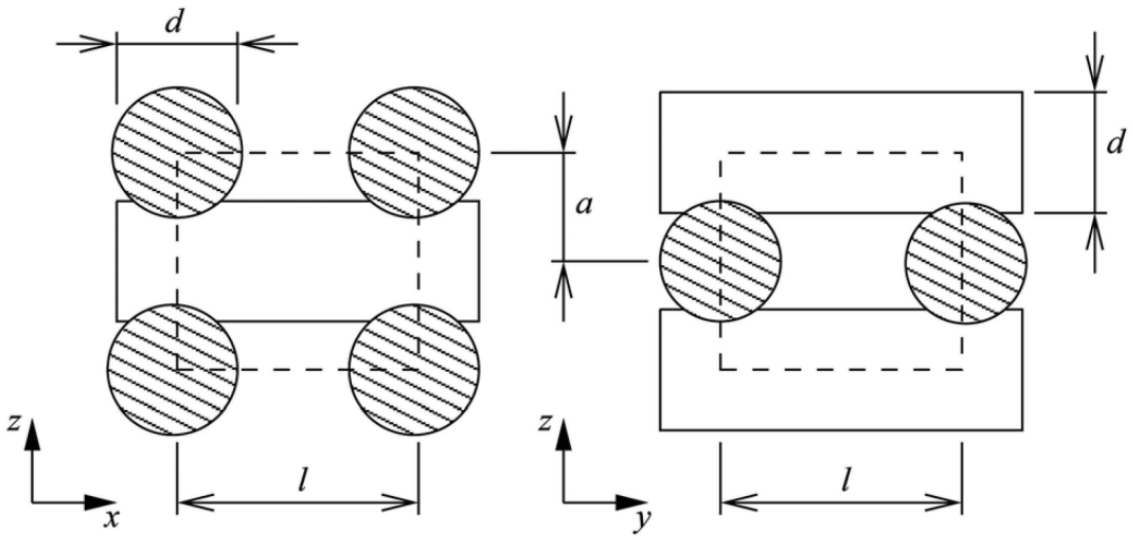

Figure 10 Norato's scaffolds models as rods stacked orthogonally in alternating directions. a corresponds to the layer height, d corresponds to the diameter of the filament, and l corresponds to the spacing.

Cuan Urquizo and Bhaskar[68] studied more complex geometries for BTE scaffolds through their compressive stiffness of staggered woodpile lattices, Figures 11 and 12. They studied them analytically, numerically, and experimentally in the stacking direction. They derived a fifth power law between the apparent Young's modulus and the volume fraction that is valid at high porosity, similarly to Norato's work, when the filaments are sitting in the middle of the overhang. For unidirectionally staggered lattices when the filaments are laying at the midpoint in one layer and aligned in the layer above, see Figure 11

$$\langle E \rangle_1 = CE(\bar{\rho})^5 \qquad (2)$$

With $\langle E \rangle_1$, the apparent Young's modulus, C a constant, E the Young's modulus of the bulk material, $\bar{\rho}$ the relative density similar to the volume fraction, ${}^{\rho^*}/_{\rho_s}$, discussed above.

For dense lattices, with a low porosity, below a relative density, $\bar{\rho}$, of 0.3, this power relationship doesn't hold. This is due to the mechanical conditions of the filaments, which are mainly shear and

diametrical compression at higher density when filament spacing is smaller. They assumed that this deviation was due to the shear of the filament that becomes non negligible at high relative density, above 0.3. Due to the shear, they applied the Timoshenko correction to include the effect of shear in the equation, obtaining the following formula,

$$\langle E\rangle_{1-T} = \frac{CE(\bar{\rho})^5}{1 + 48\pi^{-2}\kappa^{-1}(1+\nu)(\bar{\rho})^2} \quad (3)$$

Where $\langle E\rangle_{1-T}$ is the apparent Young's modulus when the Timoshenko's correction is applied, C is a constant, E is the Young's modulus of material, κ is the shear constant, ν is the Poisson's ratio and $\bar{\rho}$ is the relative density

For models in symmetrical staggered configurations, Figure 12, when the filament lies at the midpoint of the overhang between supports, they obtained the following formula:

$$\langle E\rangle_2 = \frac{1}{2}CE(\bar{\rho})^5 \quad (4)$$

They compared their analytical expressions for apparent lattice stiffness against Finite Element calculations which showed a slight departure from the fifth power law. In the case of unidirectional staggered lattice, they obtained: $\langle E\rangle \sim (\bar{\rho})^{4.8}$. For the bidirectional staggered lattice, they obtained: $\langle E\rangle \sim (\bar{\rho})^{4.7}$. The reason for the different power laws obtained by FE is that at higher relative density the smaller filament spacing causes deviations from beam theory as shear and compressive deformation modes become more important.

The higher the density is, the higher the deviation will be, see Figure 13. Although, the micromechanics of the scaffolds are bending dominated and the differences in power laws with honeycombs or other studied structures are linked to the dimensionality and differences in architecture. The power law scaling of the apparent properties is not always guaranteed but it is of great interest.

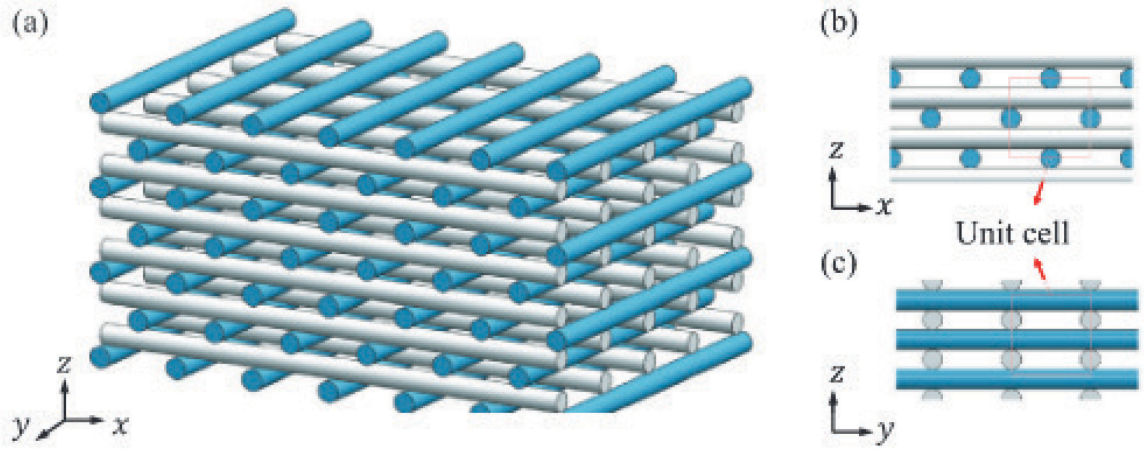

Figure 11 (a) Schematic diagram of the unidirectional staggered woodpile arrangement from Cuan Urquizo et al. (b) Front view of the structure in the xz plane; blue shaded filaments are staggered in alternating layers, (c) side view of the structure in the yz plan

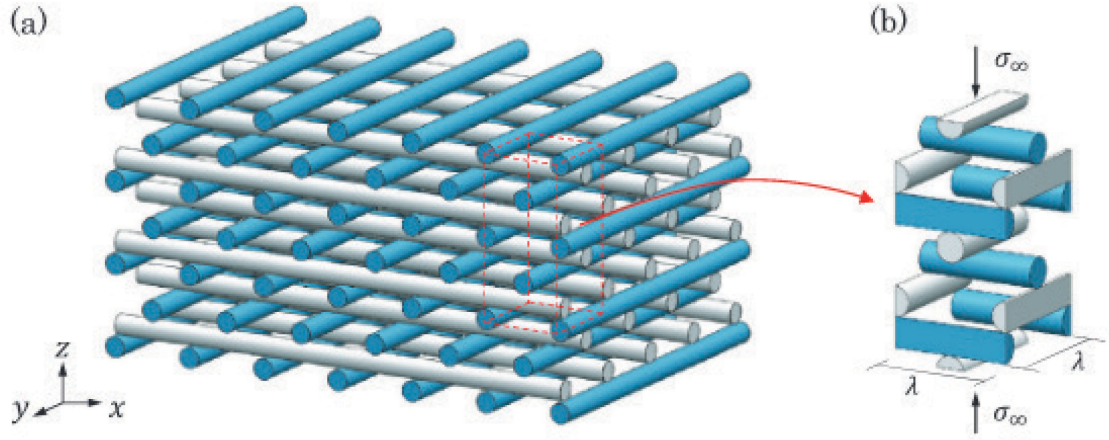

Figure 12 (a) Schematic sketch of the staggered woodpile structure created by Cuan Urqizo et al. (b) the unit cell of the structure. □ corresponds to the spacing, s.

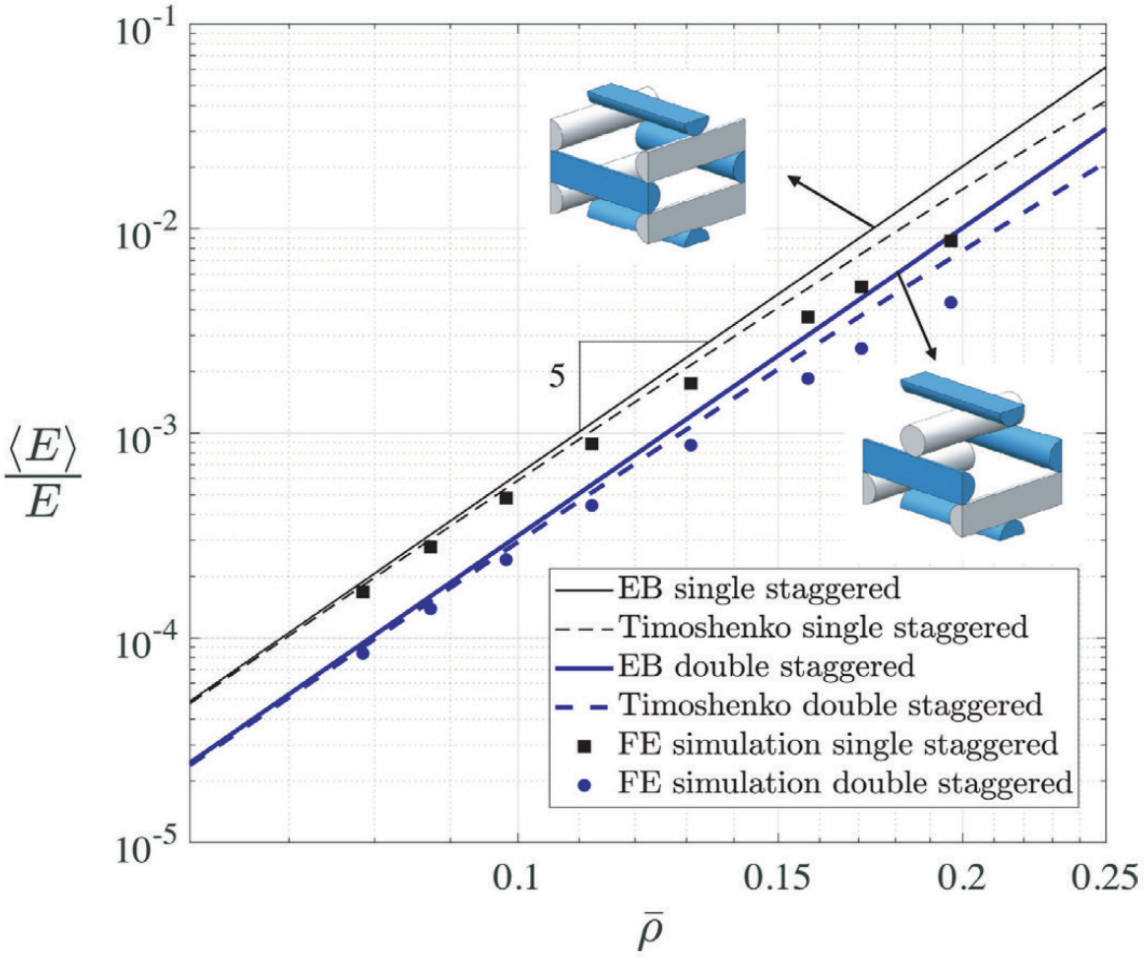

Figure 13 Comparison of modulus versus relative density as predicted using analyses and the finite element simulations. Results obtained using Euler-Bernoulli (Solid lines) and Timoshenko (broken lines) models for the filament flexure. The discrete points correspond to the finite element models results[56]. From Cuan Urqizo et al.

For later discussion, these results and Cuan Urquizo's work will be compared. Their models are the most similar to these scaffolds, and they well describe the evolution of the apparent Young's modulus with the porosity.

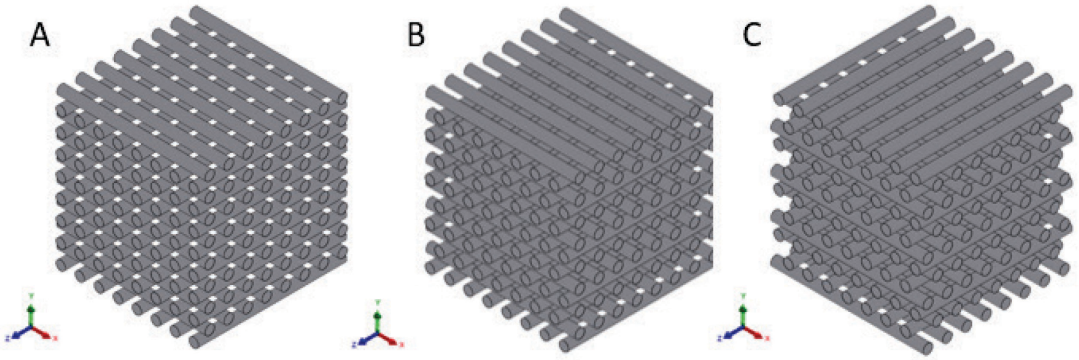

$$\langle E \rangle = \frac{E\pi(1-\alpha)}{2}\left(\frac{d}{l}\right)^2\left[0.37\left(-(1-\nu)(1-\alpha)+2ln\left|\frac{2-\alpha}{\alpha}\right|\right)+8.666\nu^2\left(\frac{d}{l}-1\right)\left(-(1-\alpha)+ln\left|\frac{2-\alpha}{\alpha}\right|\right)\right]^{-1}$$

$$\langle E \rangle_1 = CE(\bar{\rho})^5$$

$$\langle E \rangle_2 = \frac{1}{2}CE(\bar{\rho})^5$$

Figure 14 A. Uniform aligned scaffold and the equation to calculate its apparent Young's modulus from Norato et al. **B.** Semi staggered scaffold, every other layer is offset and the equation to calculate its Young's modulus from Cuan Urquizo et al. **C.** Uniform offset scaffold, every layer is offset and the equation to calculate its apparent Young's modulus from Cuan Urquizo et al.

2.6 Influence of FFF printing parameters on mechanical properties

When setting up a print, it is essential to pay attention to the printer parameters. The extruder nozzle diameter will define the minimum diameter of the printed filament. The upper limit of the diameter depends on the layer height chosen for the print and on the flow rate, the quantity of filament passing through the extruder per unit of time. When the layer height decreases for a given flow rate, the filament is extruded closer to the previous layer, making it flatter and wider. The flow rate corresponds to the amount of material fed to the extruder per unit of time. If it increases at given layer height, the diameter will get higher as more material is pushed through the nozzle, with the diameter of the nozzle as a limit. The flow rate also determines the speed of the print. The contact area between the layers is then defined by the diameter of the extruded filament, the layer height, the flow rate and the extrusion speed impacting the later.

It has been observed that structural parameters such as filament spacing, filament orientation and manufacturing parameters, such as extruder temperature or extruder movement speed have a great influence on the mechanical properties of FFF parts. These findings highlight the importance of understanding the structure-property relation in parts fabricated using fused filament fabrication.

As discussed in the previous section, the spacing between filaments plays a major role in defining the properties of the scaffold. In the following paragraph, the spacing of filaments is discussed as a processing parameter for parts that are intended to be nearly fully dense, with a relative density above 0.3. Rodriguez et al. [72] characterized the stiffness and strength of ABS parts based on the structural parameters. They found that the optimal filament gap was -25.4 µm, with a filament of diameter of 400 µm, when the structure was optimized for compressive strength. The negative distance indicates that there is overlap between neighbouring filaments. To define this optimal gap, they studied three different arrangements of filaments in the fused filament fabricated parts. In the first one, the filaments in each layer were aligned with the filaments of the adjacent layers and were separated by a negative gap. In the second one, the filaments were skewed, and they were separated by negative gaps. In the third one the filaments were skewed with positive gaps. They measured the stiffness and strength of the parent material, on raw monofilaments, to compare them with the printed samples. The aligned parts with negative gaps had the highest stiffness and strength values. Mechanical properties of the FFF parts were found to be inferior to those of the parent material. They observed a reduction of 11% to 37% in the stiffness and 22% to 37% in the strength[72]. The largest difference corresponds to parts fabricated with positive gaps between the filaments. The reduction in mechanical properties is attributed to the voids. The decrease of mechanical properties could be seen as a drawback, but the parts were lighter and produced faster than fully dense parts.

Another way of modifying the spacing of the scaffolds is to change the layer height. Kuznetsov et al. offered a new methodology for researching the influence of material processing parameters on the mechanical properties of fused filament fabricated parts, highlighting that the standards are not applicable to FFF printing technology[73]. Following their methodology, they found that layer height had the greatest influence on intra-layer adhesion. The part strength decreased along with the layer height increase. They also found that the nozzle diameter had a significant influence on interlayer adhesion. They studied nozzles with a diameter of 0.4, 0.6 and 0.8 mm. They concluded

that for a constant layer height, printing with a larger nozzle diameter resulted in increased strength.

The layer height and the nozzle diameter both impact the contact between the layers of filaments and therefore the interlayer adhesion. Abbott et al. investigated the effect of layer height on contact length between filaments[18]. They found higher tensile strength for layers built in the XY orientation due to increased contact length between neighbouring roads, Figure 15. One of their key findings was the relation between the tensile strength and the contact length, see Figure 16. It implies that a structure can be designed to be less than fully dense without sacrificing interlayer strength and therefore contribute to weight savings or increased cell proliferation. There is not only one set of printing parameters that will generate optimal properties. The designer should consider the build orientation and the print parameter selection depending on the intended use of the scaffold.

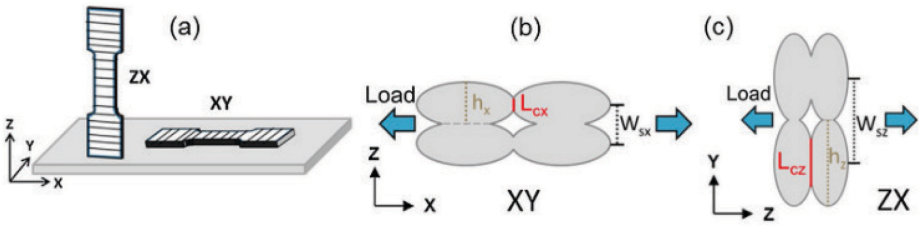

Figure 15 From Abbott et al. (a) Printed orientations: XY (flat) and ZX (vertical). Contact length, road height and road spacing notations is defined for (b) XY and (c) ZX orientations

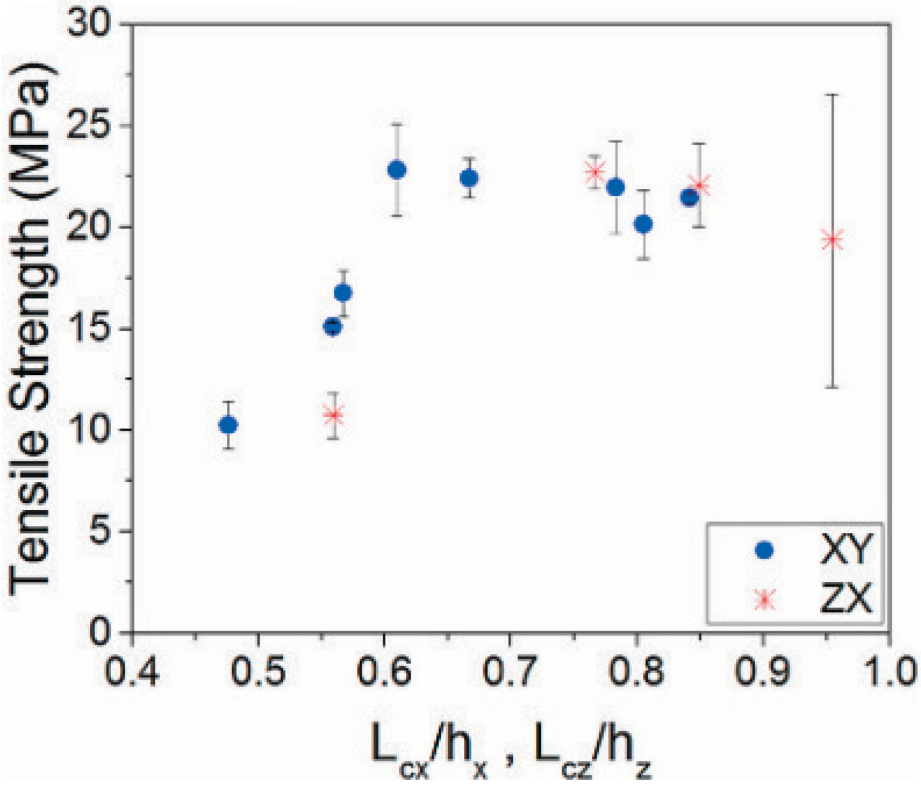

Figure 16 Results from Abbott et al. showing tensile strength with normalized contact length of the contact area between the filaments. XY direction is in blue and ZX is in red.

Bellini et al. [74] presented a comparison between the mechanical properties (tensile strength, maximum strain, and elastic modulus) of ABS single pre-manufactured filaments and single FFF-ABS filaments. Almost no extrusion effect on the strength and stiffness was observed. A reduction of one third on the maximum strain was noted. As the material passed through the extruder the molecular chains aligned resulting in reduced elongation to failure. The samples laying on the printing plane were more sensitive to nozzle-path modifications. The samples that were built perpendicular to the printing plane had their mechanical response predominantly dependent on the bonding between layers. Different deposition trajectories will produce parts with varying mechanical properties, even if the macro shape and dimensions are the same.

Contact area between layers is crucial to finely tune the mechanical properties of scaffolds. In order to get a better understanding of the interlayer adhesion Coogan and Kazmer modelled the interlayer contact and contact pressure during fused filament fabrication[75]. They found out that small layer height contributed most significantly to increasing the exit contact pressure, which is responsible for forcing the new layer into intimate contact with the previous layer. The contact pressure was found to directly correlate with interlayer contact, so contact pressure is expected to be a critical determinant of the final part strength. Their model aims at predicting contact length,

providing a crucial missing piece toward a comprehensive FFF strength model by outperforming bond width predictions based purely on conservation of volume given by the printing geometry. For the range of processing parameters they explored, pressure-driven intimate contact was a critical contributor for interlayer contact.

Another important parameter defining the part strength in combination with the spacing is the deposition orientation. This parameter will define the shape of the pores between filaments. Montero et al. [76] considered the deposition orientation and the gap between filaments to observe their influence on the strength of FFF specimen. A reduction of 67%-72% of the mechanical properties compared to the parent material was observed, attributed to the presence of voids, and filaments orientation. Anh et al. [77] studied the influence of manufacturing parameters on the tensile and compressive properties. They considered parameters such as filament orientation, filaments width, and filament separation. The influence of filament separation and orientation on tensile strength was observed to be most significant. The strength of the parts loaded along the axis perpendicular to the printing plane was tested under compression, resulting in 15% lower compressive strengths than the axially loaded samples. They considered filament orientation aligned to the loading direction (axial), 45° (crisscross) and perpendicular (transverse). The structure was 10-times stronger axially than transversally. This suggested an important anisotropy of parts fabricated with FFF, as parts were directionally sensitive.

As discussed above the spacing and the layer height modify the contact area between the filaments. In Fused Filament Fabrication melted plastic filaments are deposited to create a shape. The extrusion temperature of these filaments is also defining the interlayer adhesion. Rodriguez et al. [72]concluded that the extrusion rate and envelope temperature, the temperature of the surrounding environment, affect the filaments cross-section and the filament-to-filament bonding strength. Finite element heat transfer analysis was used to understand the solidifying temperature process. The centre of the part cooled rapidly, within 0.55s. Variations in the filament thickness were attributed to the non-uniform temperature distribution shown in the temperature profile. Their observations were supported through scanning electron microscopy (SEM) analysis.

The temperature of the layers is also impacted by the printing speed as the filaments remain at elevated temperature for some time after deposition, as shown by Rodriguez et al. Abbott et al. studied the relationship between print parameters, thermal history, mesostructure and tensile

strength for ABS filament[18]. The increase of the print speed negatively affected the tensile strength and the contact length. An increase in extruder temperature resulted in a minor increase in tensile strength and contact length. However, Zhang et al. went further and proposed a three-dimensional transient mathematical model of temperature variation with respect to space and time for fused deposition modelling[78]. The considered sample is a cuboid at fixed raster angled of 0(90°) and filling ratio of 100%. In their study, the printing speed was predicted to be positively correlated to mechanical properties of constructed components through the mechanism of thermal coalescence between neighbouring filaments. Even though they neglected the influence of heat radiation, and they modelled the manufactured component pore-free, they showed that the reheating effect of a previously deposited filament by a newly deposited filament is happened in all cases but mainly in the layer thickness direction. They also demonstrated the importance of temperature settings (temperature of extruder, temperature of heat bed and environment) in the control of the overall cooling rate to reduce internal stresses and promote interlayer bonding. They concluded that the higher the layer height of printing the lower the overall cooling rate. Their conclusions go against Abbott et al. or Kuznetsov conclusions concerning the interlayer bonding. However, in their work Zhang et al. studied fully dense parts and divided them in cubic voxels which explains the difference as they are not considering porosity or contact length.

In 2016, Faes et al. highlighted the importance of the interlayer cooling on the mechanical properties of components produced via FFF[79]. They varied the interlayer cooling time by changing the number of parts built at a time and performed tensile tests. They discovered an inverse correlation between the inter-layer cooling time and the ultimate tensile strength. They attributed this phenomenon to the prolonged cooling of the deposited material which resulted in weaker interlayer bonding. However, they acknowledged the lack of thermal monitoring. Their finding supports that higher printing speed should result in stronger interlayer adhesion due to shorter cooling time.

2.7 Summary

After studying bone properties, BTE scaffolds appear to be a sensible choice to mimic bone structure and be a viable alternative to autografts. Research has shown that using a gradient pore structure would be the most suitable to both provide similar mechanical properties to trabecular bone while favouring cell growth and proliferation. Many materials have been studied to obtain bone like engineered structure. Thermoplastic extrusion has appeared has a prominent technique in the field allowing to use different polymer materials, printing quickly, with a high degree of

control on the structure. From the literature two analytical models have already been developed to study aligned or offset filaments. No model exists for gradient scaffolds. The importance of the contact area and its influence on the mechanical properties of 3D printed scaffolds has been partially studied. The printing parameters and their influence on the contact area and the mechanical properties is worth further studying.

The main objective of this thesis is to understand the mechanical properties of 3D printed scaffold for bone tissue engineering. Even though many researchers studied the mechanical properties of 3D printed scaffolds no one has developed a micromechanical model for gradient scaffolds. Gradient scaffolds are known to favour cell proliferation and vascularisation. The mechanical properties of this kind of scaffolds are hard to understand due to their complex architecture. The existing models only consider aligned filament or offset filaments. The study of gradient scaffolds is useful for the design of 3D printed scaffolds, for the fine tuning of their mechanical properties and overall help develop better scaffolds for bone tissue engineering.

Many researchers worked on the alignment or the spacing of the filaments. In this study these parameters are accounted for and are studied through existing models. A gradient model is developed based on these models. However, the discrepancy between the models and the experimental results is addressed, a new path of research is highlighted at the cross path between manufacturing and thermal management.

The contact area is extensively studied in this thesis. It is characterised with optical microscopy and tested at different printing parameters. Printing parameters have a direct influence on the interlayer adhesion of lattice scaffolds. From this study, the printing parameters can be modified linked to the contact area to finely control the mechanical properties of the 3D printed scaffolds.

2.8 Aims and Objectives

The aim of this study is to explore the influence of printing parameters such as filament spacing, printing speed or layer height on the mechanical properties to allow a fine tuning of the mechanical response of complex 3D printed scaffolds. For this study to the focus was drawn up the exploration of BTE scaffolds and to compare theresults to the literature highlighting some areas worthy of further studies. Experimental results are compared to the models developed by Norato et al. and

Cuan Urqizo et al. A guide to printing with a custom MATLAB code giving a total control on the printing parameters of commonly available FFF 3D printers is also provided.

- Comparison of uniform aligned, uniform offset and gradient scaffold mechanical behaviour tested in compression to the literature for validation and prediction of the Young's modulus based on the models developed by Norato et al. and Cuan Urqizo et al.
- Mechanical characterisation will be performed on uniform aligned, uniform offset and gradient scaffold in compression to study the influence of the material, the filament spacing and the filament arrangement on the apparent mechanical properties.
- The influence of the printing parameters, including the extruder temperature, the printing speed, the alignment of the filament and the layer height, on the scaffold structure will be evaluated.
- The contact area between the layers will be observed following the use of different printing parameters.

Chapter 3 Methodology

3.1 Scaffold design

This report will focus on the design and study of the mechanical properties of gradient scaffolds. Four main categories of scaffolds, uniform aligned, uniform offset, discrete gradient, and gradient, will be analysed to understand gradient scaffold mechanical behaviour better. Table 2 summarizes the designed dimensions of all the scaffolds. All scaffolds were designed as cubes with a height, H, a width, W, and a depth, D, of 25 mm. The designed diameter of an extruded filament, d, was 0.38 mm. The designed layer height, h, was 0.35 mm. The designed spacing, s, and offset distance, od, was varied within a gradient scaffold by the spacing increase, Δs, as shown in Figure 17, but was constant within uniform scaffolds at the values specified in Table 2. In terms of pore shape, a tetragonal pattern was designed with a 0°/90° alignment between subsequent layers as the chosen printing pattern. All the scaffolds were first designed as an assembly of cylinders using Solidworks (Dassault Systèmes, France) and exported as .step files. The scaffolds were built layer-by-layer in the Z direction as seen in figure 17.

The G-code files (printing instructions) were generated through a slicing software, Slic3r (Open-source) after importing the .step files from CAD. Later MATLAB was used to gain more control over the printing instructions. The code was derived from the open-source code of Slic3r. It was difficult to print single lines with Slic3r. Using MATLAB allowed to print single lines of extruded materials at the desired position. The spacing of these lines was accurately defined through the movement of the extruder and the heat bed. All the information regarding the MATLAB code can be found in the MATLAB G-Code in Appendix A. Using MATLAB allowed a precise control of the printing parameters, such as the printing speed, the extruder temperature, the layer thickness, the printing pattern, and the offset between the layers. All the analysed samples were printed with the MATLAB generated custom G-Code. The scaffolds were printed as a series of parallel lines at spacing, s, and within an outside square perimeter W by D. This set of lines was repeated for the next layer by changing the orientation of the lines by an angle of 90° and shifting the position upward by a distance h and sideways by a distance od. The spacing between lines results in the porosity of the scaffolds and means that the filament printed on top of previous layers needs to bridge the gap between lower filaments without support from below.

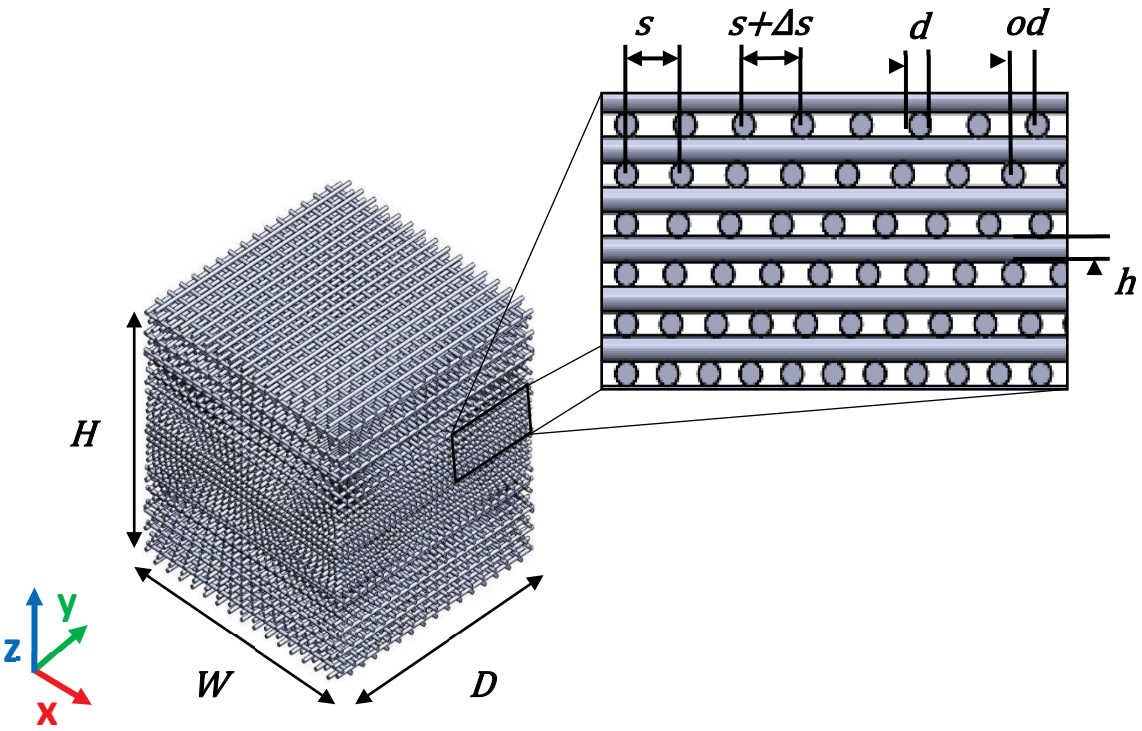

Figure 17 Gradient scaffold schematic showing overall dimensions (W, D, H) and key architectural parameters (s, Δs, d, od and h).

Table 2 Designed dimensions of the scaffold in millimetres (mm).

W**(mm)**	Width of the scaffold	All	25
D**(mm)**	Depth of the scaffold	All	25
H**(mm)**	Height of the scaffold	All	25
***d* (mm)**	Diameter of a filament	All	0.38
***h* (mm)**	Layer height	All	0.35
***s* (mm)**	Spacing	Uniform	0.65, 0.85, 1.2, 1.45, 1.65
		LHL grad	0.85/1.45/0.85
		HLH grad	1.45/0.85/1.45
		Discrete grad	0.85/1.45
od**(mm)**	Offset distance	Uniform	0.32, 0.42, 0.60, 0.72, 0.82
		LHL grad	Varying
		HLH grad	Varying
		Discrete grad	Varying
***Δs* (mm)**	Spacing increase	LHL grad	0.017
		HLH grad	0.017
		Discrete grad	0.60

3.1.1 Uniform Aligned

In the uniform aligned scaffolds the design spacing, *s*, is the same in all the layers, Table 2. The spacing chosen will define the porosity of the scaffold. In uniform aligned scaffolds, the filaments which bear the load are directly on top of each other (Figure 18), the offset distance, od, between the filaments of two successive layers is zero. Therefore, the load path for compressive loading in the build Z direction is straight and can be modelled as axial compression of the unit cell shown in Figure 18. The contact area between orthogonal filaments, assumed to be elliptical, is also shown in Figure 18. This unit cell (Figure 18, isometric view) can be repeated with periodic boundary conditions to make up a larger scaffold with uniform aligned architecture, and hence its relative

density and mechanical response (calculated from Equations 6) can be used to predict those of the corresponding scaffold.

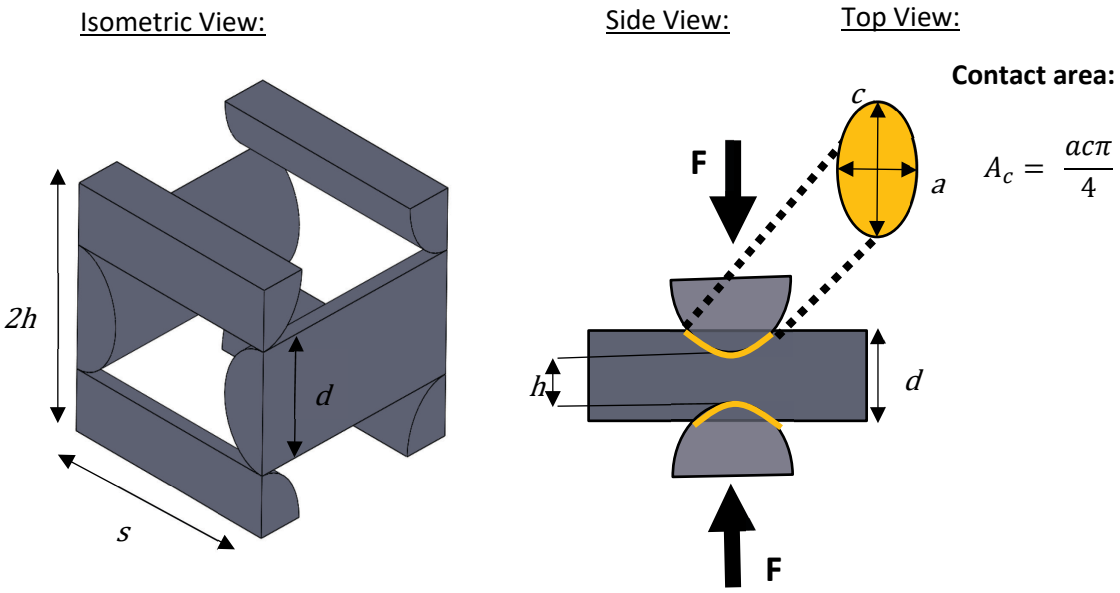

Figure 18 Aligned unit cell mechanical behaviour. Left Aligned unit cell with dimensions. Right Isolated part of the aligned unit cell to study uniaxial compression. A_c is the contact area between the filaments (shown yellow).

3.1.2 Uniform Offset

The uniform offset scaffolds were created to study the effects of the offset appearing in the gradient scaffolds due to the change in spacing between layers. The spacings were exactly the same as the uniform aligned scaffolds. The offset distance between the filaments in the uniform scaffolds was set to half of the spacing, $od = 0.5s$, which is not fully representative of the varying offset distances observed in the gradient scaffolds.

In the uniform offset scaffolds, the spacing, s, is the same in all the layers, Table 2. The chosen spacing will define the porosity of the scaffold. In uniform offset scaffolds, the filaments which bear the load are not directly on top of each other. An offset distance separates them, od, equals to half the spacing, s, Table 2. At points of overlap between layers, each strut is constrained against vertical deflection by layers above and below and against rotation by symmetric boundary conditions. Load transfer and deflection can then be modelled like a fixed beam using the arrangement shown in Figure 19.

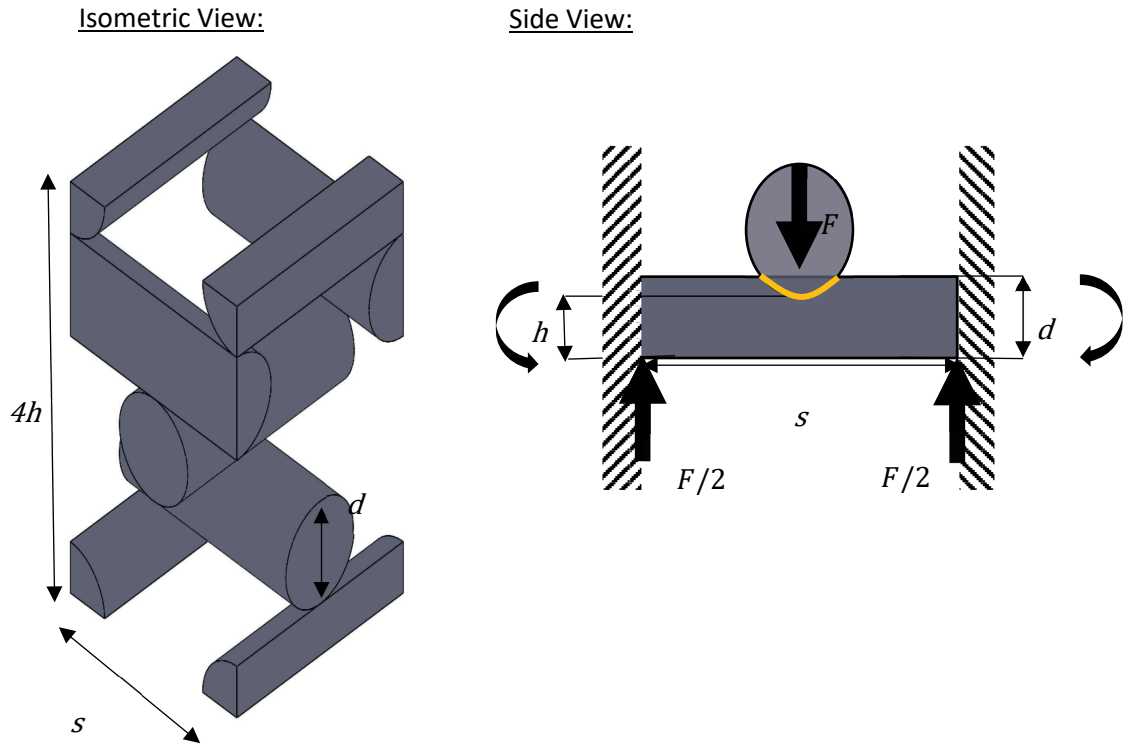

Figure 19 Offset unit cell mechanical behaviour. Left Offset unit cell with dimensions. Right isolated beam of the offset unit cell. Top right Point load, bottom right Partially Distributed Load, with contact between layers shown yellow.

3.1.3 Gradient Scaffolds

The design of the gradient scaffold is based on the research of Di Luca et al.[4] showing improved biological properties using gradient scaffolds. The designed gaps (s–d) in their work ranged from 0.5 mm to 1.1 mm, which translates into a spacing, s, of 0.85 mm to 1.45 mm, measured from the centre of one filament to the next one, creating pores ranging from 0.47 mm to 1.07 mm as the designed diameter of the filament, d, is 0.38 mm. The spacing was changed every layer by Δs. The central filaments of the scaffolds were aligned, creating two main regions due to the variable offset distance, od. In the centre, the filaments were aligned, as in a uniform aligned scaffold, Figure 20. When moving towards the edges of the scaffold, the change of spacing every layer created a variable offset between the filaments, making their centre no longer aligned, similar to an offset scaffold. Also, as the offset distance varies, the load path is no longer applied at the centre.

Two main types of gradients were created, one with high porosity/spacing at the top and bottom edges and low porosity in the centre, called High-Low-High (HLH), figure 6. The other type had low porosity at the top and bottom edges and high porosity in the centre, called Low-High-Low (LHL).

Another scaffold was created with a discrete gradient, where only two spacings were used with an abrupt change in spacing at a single interface in the centre of the scaffold. This type of gradient was used to study the interface between two distinct spacing regions. Here, the spacings used were 0.85 and 1.45 mm.

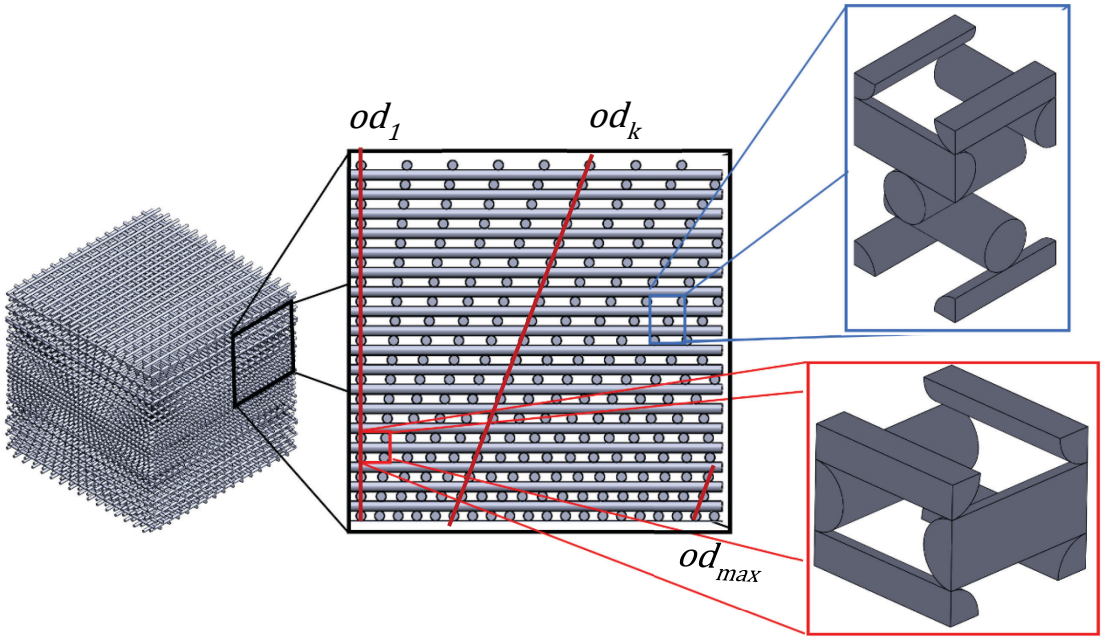

Figure 20 HLH Gradient Scaffold with aligned, offset unit cells and the offset distance at filament 1 and k and maximum offset distance od_{max}. Left Isometric view of an HLH gradient scaffold. Middle Side view of an HLH gradient scaffold showing the different regions in the gradient. Right In blue offset unit cell, in red aligned unit cell.

3.2 Materials

Non-medical grade PLA from 3DFilaPrint (UK) and PCL from 3D4Makers (Netherlands) was used to produce the scaffolds due to its wide availability and similarity to medical-grade material. Table 3 provides a summary of the relevant material properties, which were used

to predict mechanical properties and calculate the relative density and therefore, porosity.

Table 3 Important material properties of PLA and PCL for 3D printing

Property	**PLA**	**PCL**
Density ($g.cm^{-3}$)	1.24	1.1
Tensile modulus (MPa)	2290	350

Printing Temperature (˚C)	180 - 210	130 - 170

3.3 Scaffold fabrication

The scaffolds were manufactured using FFF techniques with a PRUSA i3 MK3 (PRUSA research, Czech Republic) with a standard brass nozzle (0.4 mm diameter). The nozzle temperature was set at 210°C and bed temperature at 60°C for PLA. The nozzle temperature was set at 110°C and bed temperature at 25°C for PCL. For both materials, the print speed was set to 20 mm/s. When the printing parameters were studied, in chapter 6, the nozzle temperature was set at 190°C, 210°C and 240°C, and the print speed was set at 5 mm/s, 20 mm/s and 60 mm/s. As specified in Section 1.1, the layer height was set to 0.35 mm. The diameter of the extruded filament was set to 0.38 mm. The G-code, printing instructions, was generated through a Slic3r (Open-source).

For the PLA used, its recommended printing temperature was ranging from 180 and 210˚C. To reach that temperature we set up the nozzle at 210˚C to be sure that enough heat is transferred to the material and reach the melting point of PLA, 170˚C[94]. In the experiment the nozzle temperature was set at 190˚C to study the contact area in our lattices. At that lower temperature the filament will go below the melting point of PLA quicker. The temperature of the nozzle was also set at 240˚C to allow the filament to spend more time melted and then the contact area can be studied. The nozzle temperature of 210˚C was used as a reference as that the temperature usually chosen for PLA prints.

3.4 Characterisation

3.4.1 Visual and morphological characterization

3.4.1.1 Porosity measurement

All the scaffolds were measured with a digital calliper. The width, W, the depth, D, and the height, H, were measured at three different points and averaged to obtain the volume of the scaffolds. The mass of the samples was measured with a laboratory scale. These measurements allowed us to calculate the porosity of the scaffold. Using the density of the material used the mass of the fully dense scaffold was calculated

$$porosity = 1 - \frac{mass\ scaffold}{mass\ fully\ dense\ scaffold} \quad (5)$$

3.4.1.2 Optical microscopy for mesostructured analysis

The mesostructure of the scaffolds was examined using optical microscopy. The microscope (Olympus BH Metallurgical Optical Microscope) was used with a 4x objective for large field of view. Contact area between filaments (as shown in Figure 22) and designed scaffold dimensions (as summarised in Table 2) were also measured. For quantitative measurements, images were captured at five different locations, see Figure 21(A), on five different layers separated layers, see Figure 21(B). Two measurements were made for each contact area and three for filament diameter as described in Figure 22. The layer height and the spacing were also measured. All the measurements were made using the image processing package Fiji[80]. The results are reported as averages of the measures for each specimen. A total of 72 measurements for the diameter and 25 for the contact area were taken for each specimen. Different samples were produced for mechanical testing using the same FFF processing conditions, because the measurements were destructive, and the samples could not be reused

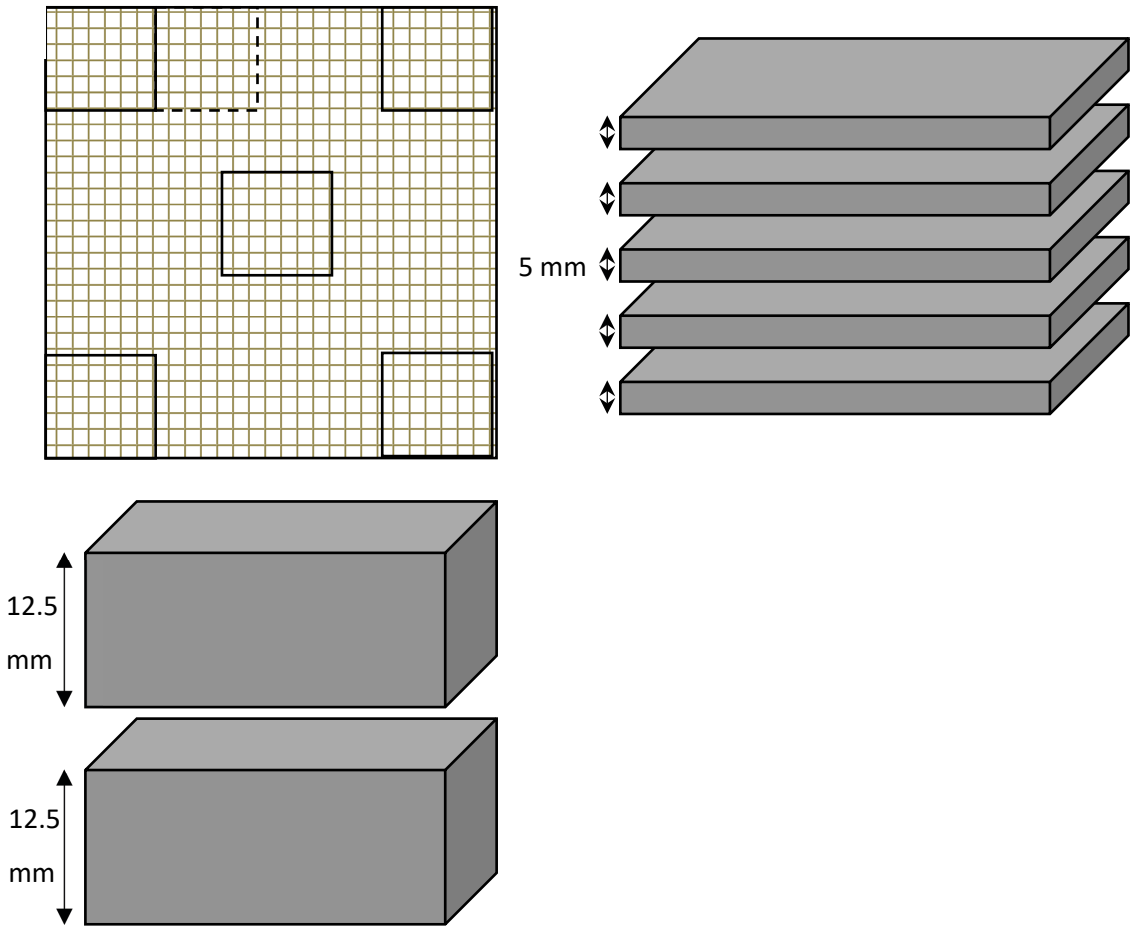

Figure 21 (A) Map of the different locations where the data were collected **(B)** Exploded side view of the scaffold after preparation for analysis, Compression Testing. **(C)** Exploded side view of the scaffold after preparation for analysis, Printing Parameters.

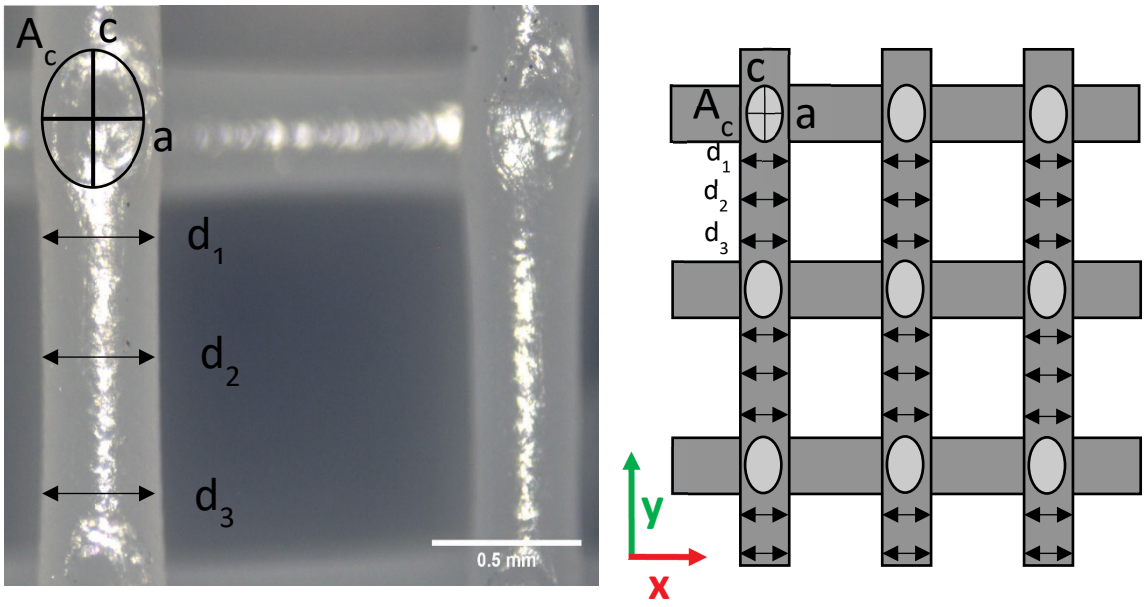

Figure 22 Diameter and contact area measurements a scaffold layer. Left Optical microscope image of a pore (Top view). Right) Scheme of the different measurements in a layer (Top view). Zoom x10.

3.4.1.3 Optical microscopy for mesostructured analysis using different printing parameters

For each set of printing parameters, described in Chapter 6, three samples were printed together on the heat bed. For the microscopic analysis each sample was split approximately 12.5 mm from the bottom, see Figure 21(C). Each half was analysed at five different locations, see figure 21(A). At each location, at least four contact areas were measured.

3.4.2 Mechanical characterisation

Compression tests were performed on all the samples using an Instron 5569 testing system with a 50 kN load cell and loaded at a rate of 1mm/min. This load rate was chosen to match the previous testing procedure for similar samples[52,53]. The samples were loaded in the build direction Z direction, corresponding to the layers stacking direction. Samples were loaded for 10 minutes to result in a final displacement of 10 mm, which exceeded the yield point for all specimens.

At least one sample was tested for each scaffold geometry in Table 2. Three samples were tested to assess repeatability for uniform aligned and offset scaffolds with a spacing of 0.85 and 1.45 mm for PLA and PCL. Three samples were tested for each set of printing parameters. Force-displacement data were extracted from the testing machine and analysed to produce apparent stress-strain graphs, on a total apparent area of 25 by 25 mm, examples of which are shown in the

results section. The linear regions of these graphs were identified after plotting the data. Then a linear regression was applied with a MATLAB code, Appendix B. A point in the middle of the linear elastic region was chosen. Then, the values were compared to the linear fit with a R^2 limit value of 0.995, as shown in Figure 23. The slope of the curve was used to determine the apparent elastic modulus of the scaffolds.

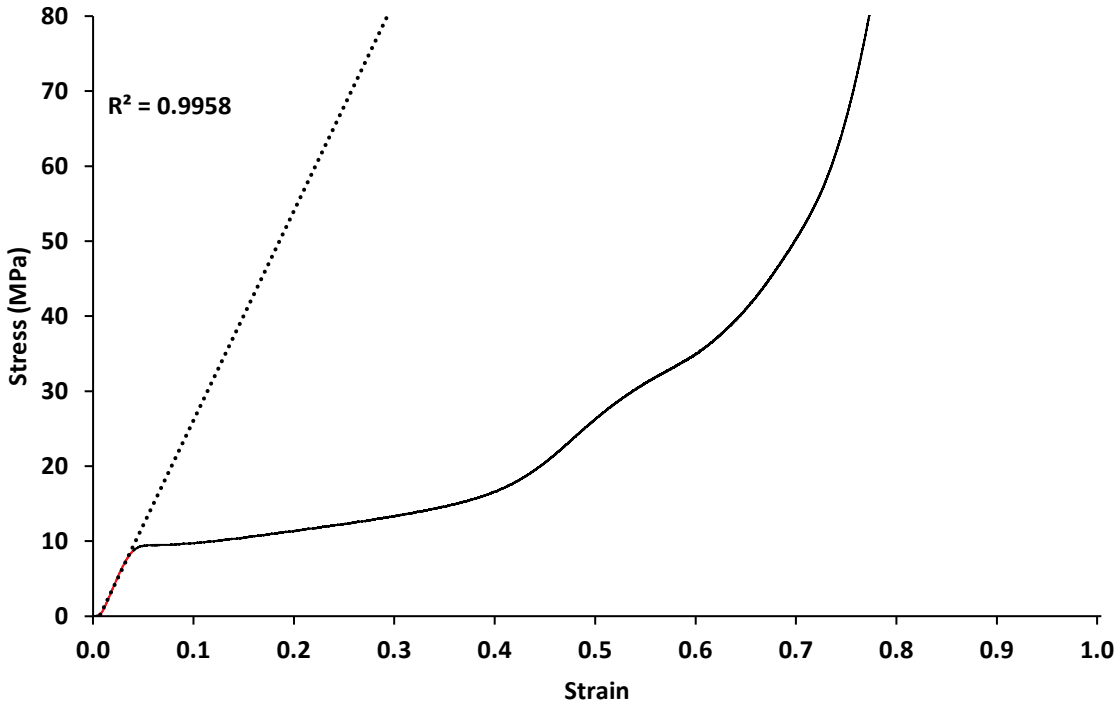

Figure 23 Representative apparent stress-strain curve for uniform aligned scaffold with spacing s = 0.85 mm, including linear regression fit to the elastic region for calculating Young's modulus.

Chapter 4 Uniform Scaffolds

4.1 Introduction

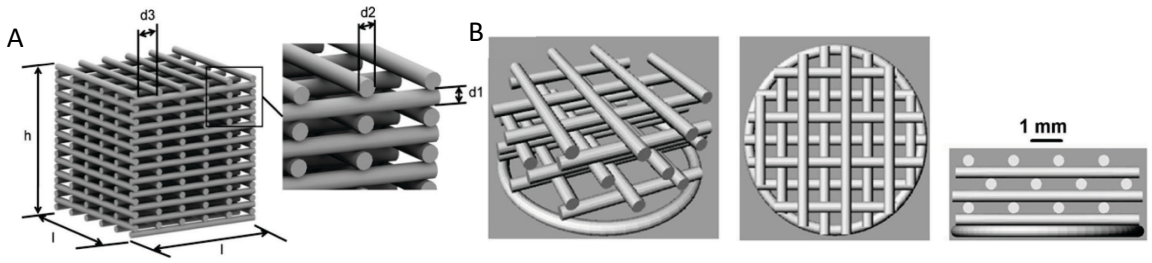

Figure 24 (A) Gregor's scaffold design[1] **(B)** Sobral's scaffold design[2]

As discussed previously in the literature review, the design used in the experiments are based on Sobral's work on homogeneous scaffolds and Gregor's work on PLA scaffolds. Figure 24 (A) shows Gregor's scaffold design. As seen in previous chapter, the design of the uniform aligned scaffold is identical. All dimensions can be matched with Figure 24 (A) the layer height, h, as d1, the diameter of the filament, d, as d2, the spacing between the filaments, s, as d3, the height of the scaffold, H, as h. The scaffolds are cubic and often the depth, L, and the width, W, are equal and are found as l in Gregor's design[46]. Figure 24 (B) shows Sobral's scaffold design and it was the inspiration for the uniform offset scaffold[2].

These two designs have been studied by other researchers either through mathematical modelling, FE or experiments. In this chapter I present the results from the uniform aligned and offset scaffolds tested in compression. The results will be compared to the previous literature in the discussion.

4.2 Mechanical properties characterisation

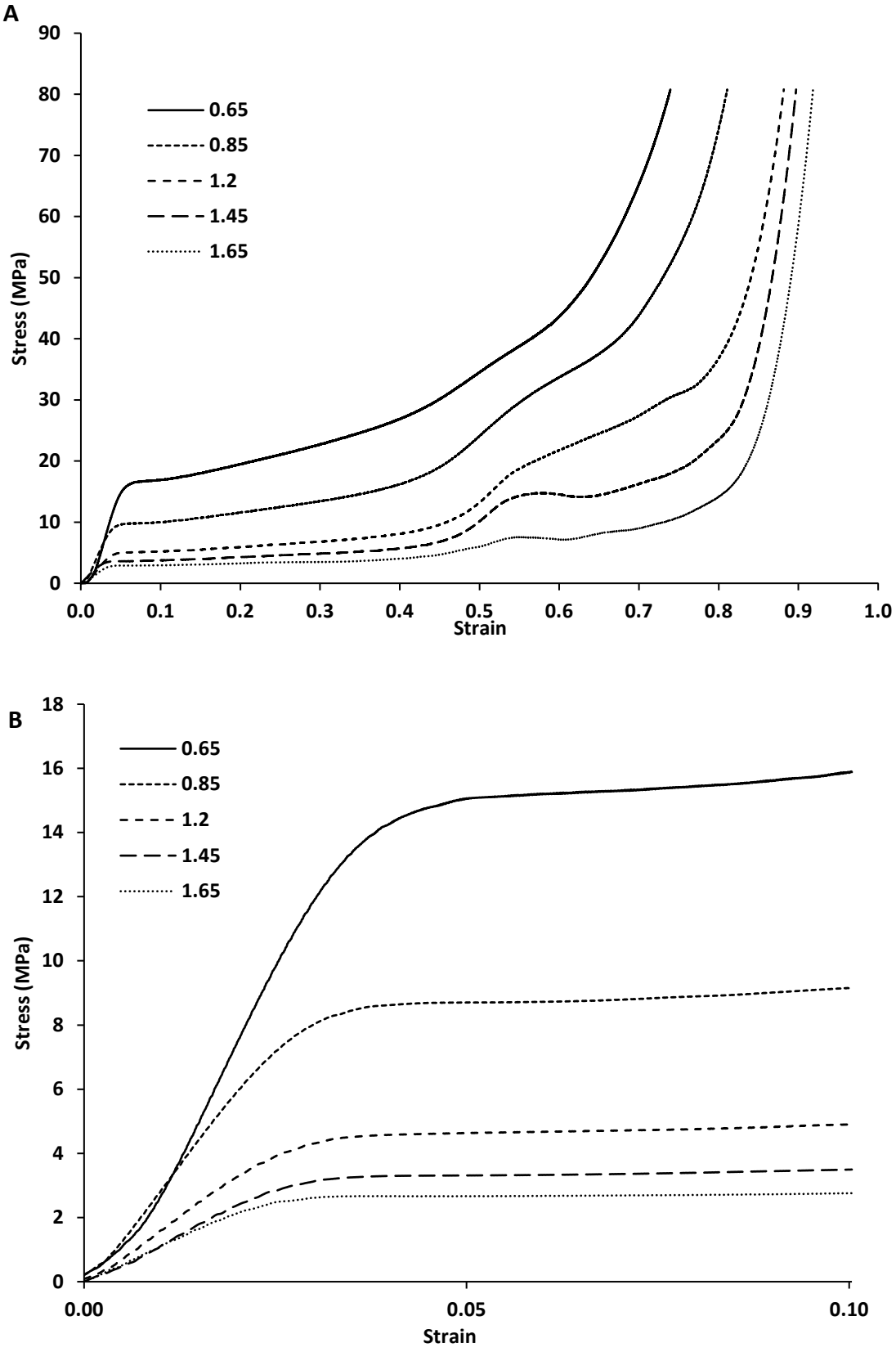

Figure 25 (A) Representative stress-strain curves for PLA uniform aligned scaffolds with spacings, s, 0.65 mm. 0.85 mm, 1.2 mm, 1.45 mm and 1.65 mm. **(B)** Focus on small strain to observe the linear elastic

region of PLA uniform aligned scaffolds with spacing, s, 0.65 mm. 0.85 mm, 1.2 mm, 1.45 mm and 1.65 mm.

Figure 25 shows representative stress-strain behaviour of PLA uniform aligned scaffolds with different spacing loaded in compression in the Z direction. All the curves exhibit an initial linear region, followed by yield and a flat plateau region, and then an increasing densification region. Stiffness and stress at a given strain both increased as the spacing decreased. The transition between the plateau region and the densification region became smaller as the spacing decreased. From Table 4, an increase in the spacing by 0.2 mm, 30%, results in a decrease by 40% of the Young's modulus, from 466.19 MPa to 281.08 MPa. The higher the porosity the less variation is observed in the Young's modulus.

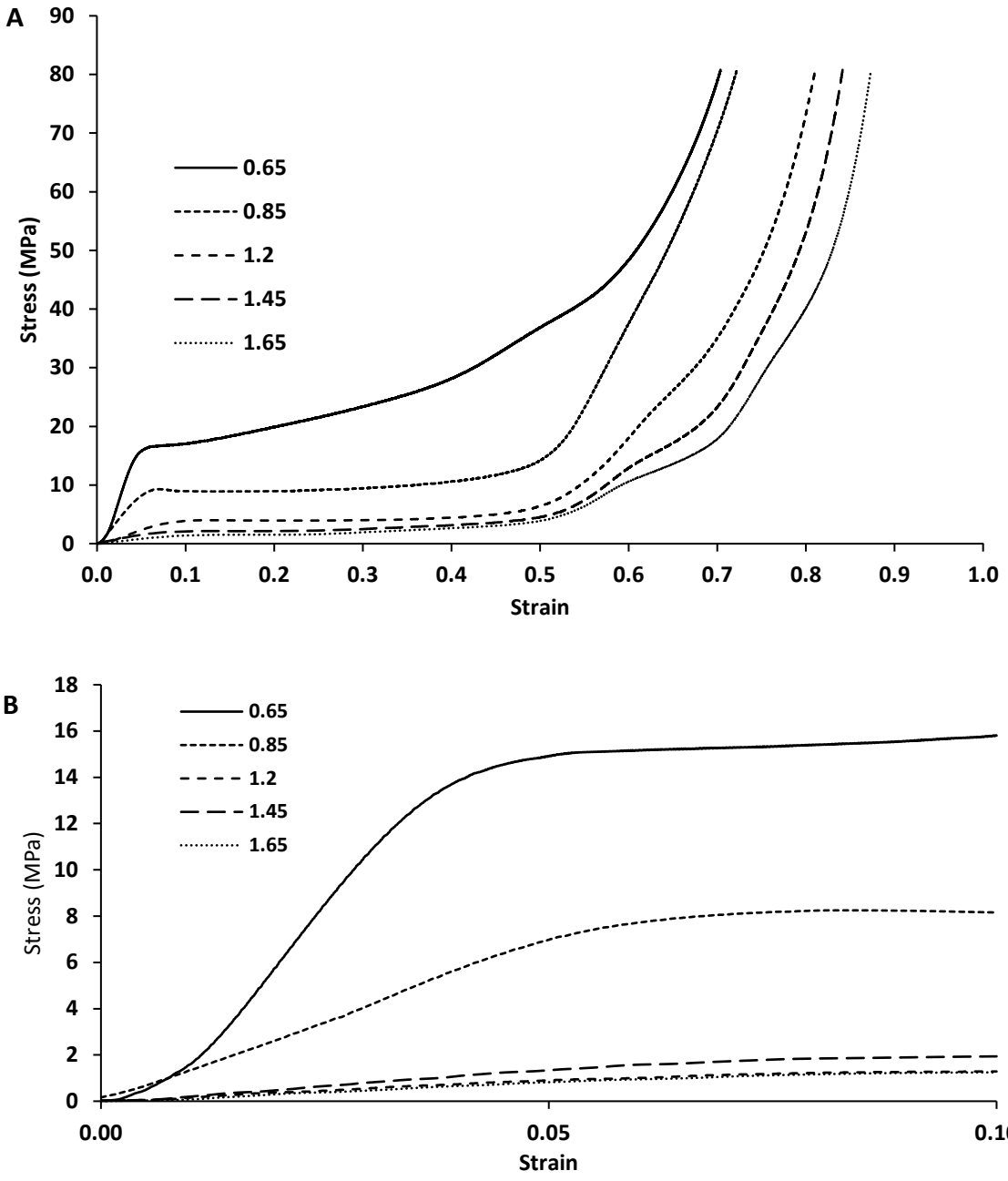

Figure 26 (A) Representative stress-strain curves for PLA uniform offset scaffolds with spacings, s, 0.65 mm. 0.85 mm, 1.2 mm, 1.45 mm and 1.65 mm. **(B)** Focus on small strain to observe the linear elastic region of PLA uniform offset scaffolds with spacing, s, 0.65 mm. 0.85 mm, 1.2 mm, 1.45 mm and 1.65 mm.

Figure 26 shows representative stress-strain behaviour of PLA uniform offset scaffolds with different spacing loaded in compression in the Z direction. All the curves exhibit an initial linear region, followed by yield and a flat plateau region, and then an increasing densification region. However, the stiffness of the uniform offset scaffold with a spacing, s = 0.65 mm, is significantly higher than the other uniform offset scaffolds. All the values of the Young's moduli are in Table 5. When the spacing tends to get closer to the diameter of the extruded filament ($s \approx d$), the mechanical behaviour of the uniform offset and aligned scaffold will become similar. As the offset distance depends on the spacing, if the spacing gets too close to the diameter of the extruded filament, it will be difficult to avoid the alignment of the filaments in a structure similar to the uniform aligned scaffold.

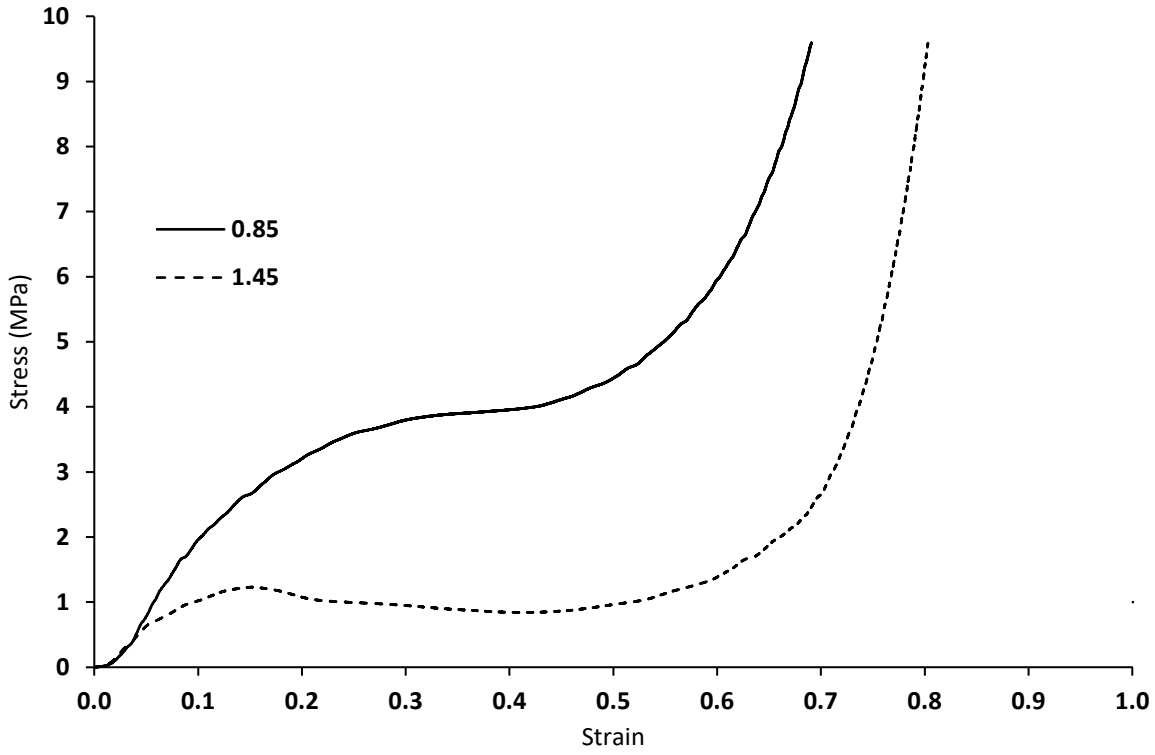

Figure 27 Representative stress-strain curves for PCL uniform aligned scaffolds with spacings, s, 0.85 mm, and 1.45 mm.

Figure 27 shows representative stress-strain behaviour of PCL uniform aligned scaffolds with different spacing loaded in compression in the Z-direction. All the curves exhibit an initial linear region, followed by yield and a short plateau region, compared to PLA, and then an increasing densification region. Stiffness and stress at a given strain both increased as the spacing decreased. The transition between the plateau region and the densification region became smaller as the spacing decreased. PCL is softer than PLA, with a Young's modulus of 350 MPa compared to 2290 MPa. When comparing the Young's moduli between PLA and PCL

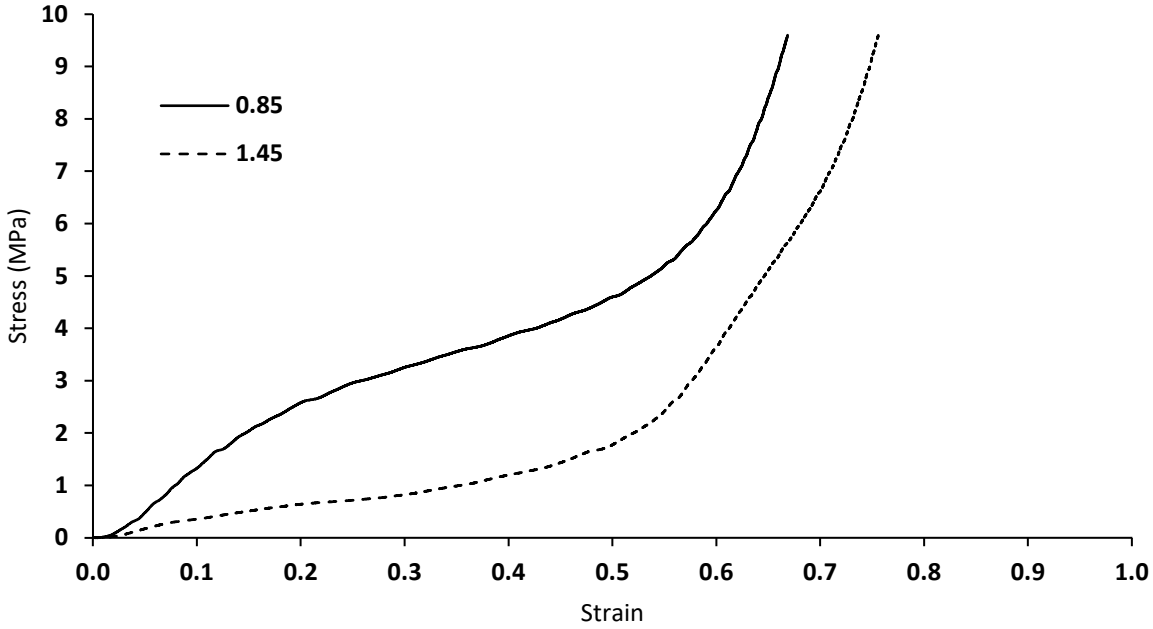

Figure 28 Representative stress-strain curves for PCL uniform offset scaffolds with spacings, s, 0.85 mm, and 1.45 mm.

there is a higher decrease with PLA, 58%, from 281.08 MPa to 118.04 MPa, Table 4 compared to PCL with a 35% decrease, from 24.52 MPa to 15.92 MPa, Table 6.

Figure 28 shows representative stress-strain behaviour of PCL uniform offset scaffolds with different spacing loaded in compression in the Z direction. All the curves exhibit an initial linear region, followed by yield and a short plateau region, compared to the PLA scaffolds, and then an increasing densification region. The plateau region here is not flat, which is similar to the softest PLA scaffolds. When comparing the Young's moduli between PLA and PCL there is a higher decrease with PLA, 84%, from164.84 MPa to 26.84 MPa, Table 5 compared to PCL with a 70% decrease, from 11.13 MPa to 3.27 MPa, Table 7.

Table 4 Experimental results for the Young's modulus of PLA uniform Aligned Scaffolds

Spacing (mm)	Sample 1 (MPa)	Sample 2 (MPa)	Sample 3 (MPa)
0.65	466.19		
0.85	283.71	281.33	278.21
1.2	148.54		
1.45	118.24	119.07	115.61
1.65	94.61		

Table 5 Experimental results for the Young's modulus of PLA uniform Offset Scaffolds

Spacing (mm)	Sample 1 (MPa)	Sample 2 (MPa)	Sample 3 (MPa)
0.65	347.81		
0.85	160.82	164.84	177.53
1.2	47.65	44.46	48.16
1.45	26.12	26.84	23.35
1.65	15.17	15.28	14.51

Table 6 Experimental results for the Young's modulus of PCL uniform Aligned Scaffolds

Spacing (mm)	Sample 1 (MPa)	Sample 2 (MPa)	Sample 3 (MPa)
0.85	24.93	23.59	24.52
1.45	16.69	15.21	15.92

Table 7 Experimental results for the Young's modulus of PCL uniform Offset Scaffolds

Spacing (mm)	Sample 1 (MPa)	Sample 2 (MPa)	Sample 3 (MPa)
0.85	9.39	12.88	11.13

1.45	3.79	3.27	3.13

4.3 Discussion

The repetition of the unit cell to create a scaffold is common design approach for FFF parts. Two different approaches can be taken. The first one is to create channels, that will act as pores, and use a gyroid unit cell composed of multiple layers[81]. The second one is to create the pore as a unit cell without trying to reproduce a spherical shape. The second approach allows to achieve smaller dimensions for the pores as the limit is the filament diameter and therefore the resolution of the printer.

Table 8 Predicted apparent Young's modulus for PLA scaffolds from the Aligned model made by Norato and from the Offset model made by Cuan Urqizo. PLA Young's modulus 2290 MPa.

Spacing (mm)	**Aligned Model (MPa)**	**Offset Model (MPa)**
0.65	472.77	699.41
0.85	302.32	247.95
1.2	166.43	58.92
1.45	118.83	25.57
1.65	94.09	14.23

Table 9 Predicted apparent Young's moduli for PCL scaffolds from the Aligned model made by Norato and from the Offset model made by Cuan Urqizo. PCL Young's modulus 350 MPa.

Spacing (mm)	**Aligned Model (MPa)**	**Offset Model (MPa)**
0.85	46.21	37.89
1.45	18.16	3.91

All the representative stress-strain curves described previously are similar to the compressive stress-strain curve for elastic-plastic foams described by Ashby and Gibson[82] and Cuan Urquizo et al.[68]

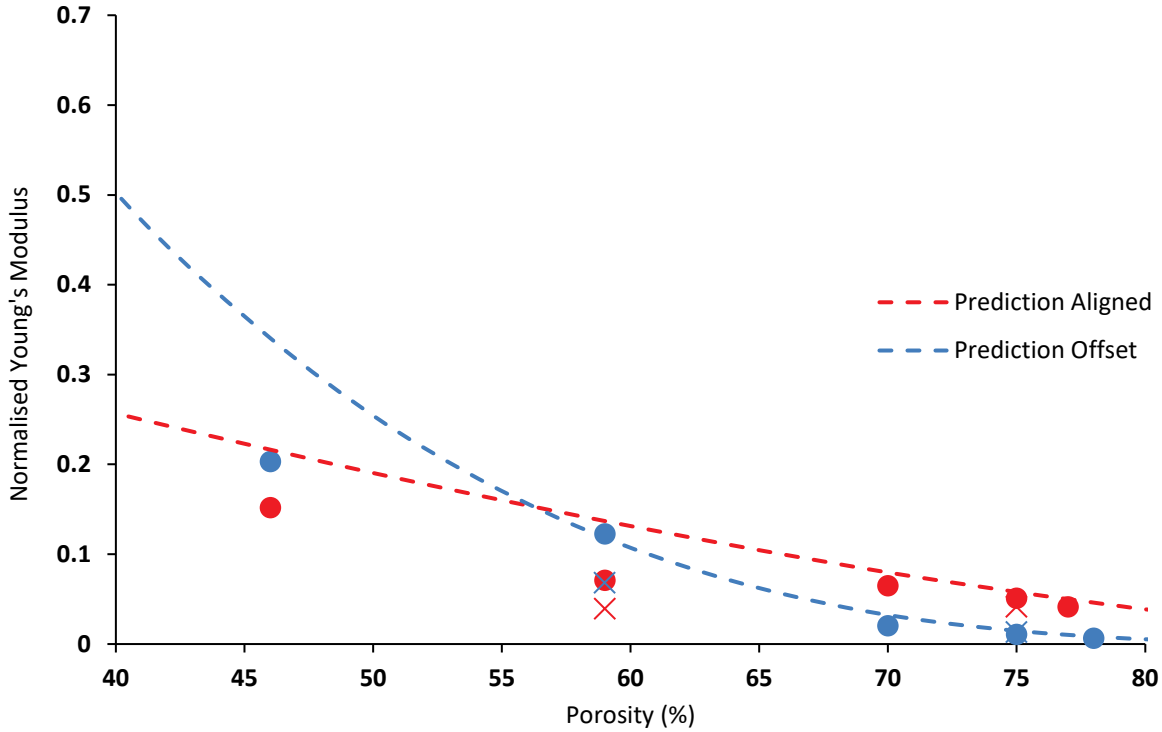

Figure 29 Normalised Young's Modulus the bulk material Young's modulus of the PLA and PCL uniform aligned and offset scaffold plotted against the porosity. The data for the uniform aligned scaffolds are in red. The data for the uniform offset scaffolds are plotted in blue. The experimental data for PLA are represented by dots. The experimental data for PCL are represented by crosses. The prediction for the aligned scaffolds is obtained with Norato's model. The prediction for offset scaffolds is obtained with Cuan Urqizo's model. PLA Young's modulus 2290 MPa PCL Young's modulus 350 MPa.

A decrease in porosity will result in an increase of the stiffness, figure 29, and stress at a given strain as there is more material to resist the deformation. The aligned scaffolds are stiffer and have higher stress than the corresponding offset scaffolds at the same strain. More filaments are directly in the load path to resist deformation. The filaments, in uniform aligned scaffolds, resist the deformation as columns whose cross-section is equal to the contact area between the filaments.

Naghieh et al. manufactured uniform aligned scaffolds. The parameters of their scaffolds were different from the ones manufactured. The diameter of the filament was 0.7 mm, and the spacing between the filament was 0.35 mm which makes their scaffold close to the uniform aligned scaffold with a spacing of 0.65 mm. They found that their scaffolds had a Young's modulus around 183.62

MPa. When normalising their result to the Young's modulus of the PLA, 0.121 wasobtained, which is close to the modulus of the uniform aligned scaffold with a spacing of 0.85 mm, 0.122. Therefore,a scaffold with a higher porosity and a similar stiffness was obtained. When they used a finite element model they found a Young's modulus 16% higher, 213.21 MPa, than during their experiments. When using the model developed by Norato et al., Equation 6, the prediction was 6% higher than the experimental result.

Norato and Wagoner [69] used their knowledge of cellular solids to create bone scaffolds and understand the influence of the pore size on their stiffness. They modelled the scaffolds as rods stacked orthogonally in alternating directions (Figure 30). Their parameter, l, corresponds to the spacing, s. The layer height, h, corresponds to their parameter, a. For the calculation of the stiffness, they used Finite Elements models and used numerical homogenisation assuming that what happens to one unit cell can be generalised to the scaffold. They considered the diameter, the spacing and the overlap. Norato and Wagoner[69] modelled the uniform aligned scaffolds as discs in diametrical compression. They considered the contact area between the filaments. They tested their model with different overlaps, α, ranging from 0.05 to 0.45. As seen in the equation below:

$$\langle E \rangle = \frac{E\pi(1-\alpha)}{2}\left(\frac{d}{l}\right)^2 \left[0.37\left(-(1-\nu)(1-\alpha) + 2ln\left|\frac{2-\alpha}{\alpha}\right|\right) + 8.666\nu^2\left(\frac{d}{l}-1\right)\left(-(1-\alpha) + ln\left|\frac{2-\alpha}{\alpha}\right|\right)\right]^{-1} \quad (6)$$

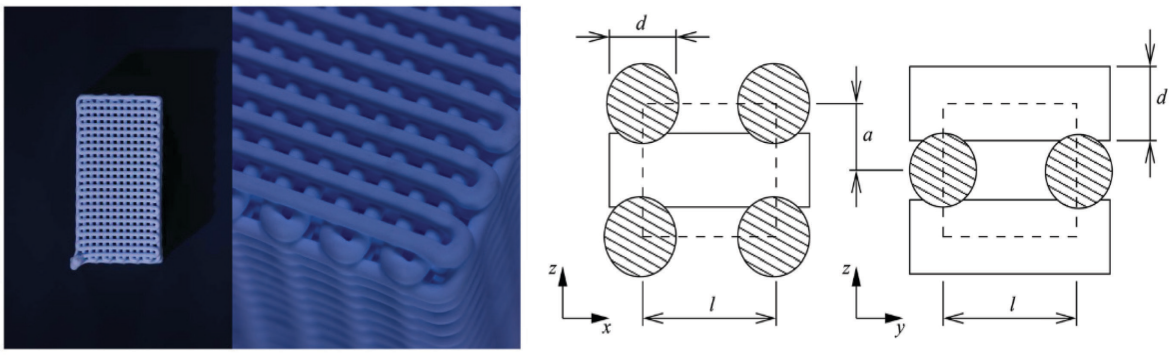

Figure 30 Norato and Wagoner's 3D printed scaffold. Unit cell considered in Norato and Wagoner's uniform aligned model.

An increase in the overlap, α in the equation, will lead to an increase in the apparent stiffness of the scaffold. Although, this model is only applicable for their specific geometry and only for the uniform aligned scaffolds. Another model is required to predict the properties of the uniform offset scaffolds. An increase in the overlap, α in the equation, will lead to an increase in the apparent stiffness of the scaffold. This parameter is not considered in the Cuan Urquizo's model for the uniform offset scaffolds.

Cuan Urquizo et al. developed analytical models for symmetrical unidirectional stacking, symmetrical bidirectional stacking, and asymmetric unidirectional stacking[68]. The uniform offset scaffolds correspond to Cuan Urqizo's symmetrical bidirectional stacking models. The model also includes a correction factor, to account for the shear when the spacing is low. The correction factor was developed by Timoshenko to take into account shear deformation and rotational bending effects to describe thick beams. The added mechanisms lower the stiffness of the beam. See equation below.

$$\langle E \rangle = \frac{CE(\bar{\rho})^5}{1 + 48\pi^{-2}\kappa^{-1}(1+\nu)(\bar{\rho})^2} \quad (7)$$

With κ the shear coefficient for circular cross-sections equals to 0.9[68], and the Poisson's ratio ν equals to 0.36 for PLA[83]. The constant C approximately equals to 31.5, this is a non-dimensional constant[68]. The bonding between the filaments was not taken into account for the offset model.

This equation is derived from the analysis of a periodically loaded elastic filament. Although, for dense lattices, with a low porosity, the relation above does not stay true as seen in the Tables 4,5 and 8 or Figure 29. This is mainly due to the filament shear and diametrical compression. The developed model is restricted to uniform offset scaffolds, when the filament lies at the midpoint between the supporting filaments, $s/2$.

Cuan Urquizo also performed experiments to define the modulus-porosity relationship. They observed 4 stages of deformation. First, there is a bending supported by neighbouring filaments. Then, a yielding of the bending filament, which is the non-linear part of the curve. Then, a plastic deformation of the bending filament. Finally, the layer n and n-2 enter in contact and the scaffold densifies and loses its porosity while increasing its stiffness.

For a low relative density, high porosity, Euler-Bernoulli micromechanics are suitable to predict the apparent Young's modulus. For both uniform aligned and offset, the models predictions are not far from the moduli obtained from compression testing, as seen in Figure 29 and in Tables 4 to 9.

The apparent Young's modulus was calculated considering the linear response at the initial phase of deformation, in the elastic region. For small values of apparent density, the results were close to power law five fit for relative elastic modulus function of the porosity. For higher values of the apparent density, above 0.25, a deviation from the theoretical asymptotic fifth power law could be observed. The higher the apparent density, the closer it is to 1, the higher the deviation, Figure 29 and Figure 31 in log-log scale[68].

The difference with the theory shows a lower Young's modulus, a lower stiffness resulting in an increased softening, in the experimental samples, they tend to be less stiff than the predicted apparent Young's modulus. Although, there was a good match between Cuan Urquizo's FE calculations and the experiments, as seen in Figure 31. Cuan Urquizo et al. supposed that the differences were mainly due to fabrication errors and measurement errors. They also showed a systematic softening, lower experimental modulus, when comparing the theory, the uniform offset model, to the FE analysis and their experimental samples. This deviation increased at higher relative density, lower porosity. The fifth power law is not exact and the relationship between the apparent stiffness and the apparent density is following this relation $\langle E \rangle \sim (\bar{\rho})^{4.7}$ for their uniform offset scaffolds. The difference in power law compared to honeycombs ($\langle E \rangle \sim (\bar{\rho})^{3}$) or foams ($\langle E \rangle \sim (\bar{\rho})^{2}$)is linked to the dimensionality and the differences in architecture. As the relative density increases, the ratio of the radius of the filament over the spacing between the filaments increases resulting in short and thick filaments where the beam theory can't be applied.

The reasons are probably that they ignored in their model the shear in the filaments, the diametrical compression was assumed negligible. The 3D effects in dense lattices, with a relative density above 0.25, were not considered and the small degree of ellipticity was not taken into account. The models assumed a circular cross section. The parameter α, the overlap, is not considered in Cuan Urquizo's model for the uniform offset scaffolds.

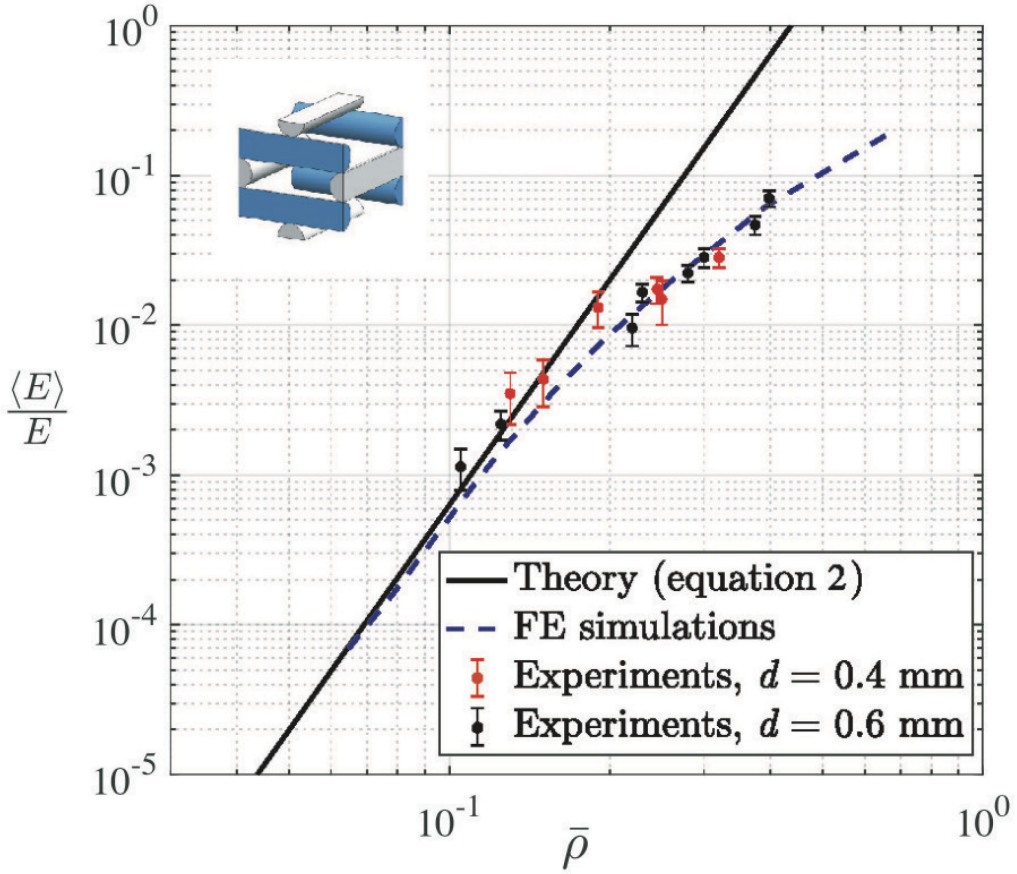

Figure 31 Comparison of the modulus-porosity relationships: as predicted by the uniform offset model (solid line), with FE calculations (dotted line) and experimental results obtained from compression test of 3D-printed samples, fabricated using different filament diameter and lattice spacing. Figure from Cuan Urqizo et al.

When comparing compression results to the models, similar results were observed for both models. For a relative porosity above 0.25 the models do not hold. The lower porosities are not covered by these models. The use of the Timoshenko's correction factor, in Equation X could not solve the problem. The apparent Young's modulus showed a non-linearity due to the contact mechanics involved.

As observed in the literature the models tend to predict well the mechanical properties of lattice scaffolds (apparent properties) till high apparent density.

4.4 Conclusion

The stiffness of bone tissue engineered scaffolds along the stacking direction of two arrangements of the scaffold was studied. The difference in stiffness of the structure for these two arrangements was studied using analytical models based on a periodic beam theory to describe the filament mechanics. The model for uniform aligned scaffolds was developed by Norato et al. The model for uniform offset scaffolds was developed by Cuan Urqizo et al. The analytical predictions were compared against experimental results. When a structure with staggered filaments is loaded remotely, the filaments predominantly experience bending. On the other hand, when a structure with an aligned configuration is loaded, the response is dominated by local elastic deformations close to the region of the filament adhesion. The fundamental micromechanics of Euler-Bernoulli were appropriate to develop analytical expressions for the apparent structure-property relationship.

The dependence of the apparent Young's modulus with respect to changes in the position of the filaments in the scaffold was brought out. Structures in the aligned configuration show a strong dependence on the overlap between filaments. The apparent Young's modulus showed a non-linearity due to the contact mechanics involved. The apparent Young's modulus of aligned configuration with filament overlapping was studied analytically and experimentally. The model developed was based on the diametrical compression of a flatten disc. An increment of the apparent stiffness was observed as the fraction of overlap increases.

For the same volume fraction structures, the aligned configuration is stiffer, than the offset configuration. The latter case is softer as it is bending-dominated. Both models struggled with high relative density, when the porosity is decreasing, and the filaments are getting closer to one another. The use of the Timoshenko's correction did not solve this problem for the uniform offset model. The power law scaling of the apparent properties is not always guaranteed but it is of great interest. In this respect the two developed models are helpful for the design of high porosity bone tissue scaffolds. They both capture the impact of the filament diameter, the filament spacing and material properties on the stiffness. Although, they are both limited to a specific geometry. An alternative solution will be explored in the next chapter to study variable offset and gradient structures.

Chapter 5 Gradient Scaffolds

As shown in the literature gradient scaffolds could potentially be used as bone grafts. In this chapter, their apparent mechanical properties using analytical models and experimental validations are discussed.

5.1 Introduction

The design of the gradient scaffold is based on the research of Di Luca et al. showing improved biological properties using gradient scaffolds[4]. They designed the gaps with a spacing limit ranging from 0.5 mm to 1.1 mm, measured from the surface of the filaments. This limit translates for the scaffolds in a spacing, s, of 0.85 mm to 1.45 mm, measured from the centre of one filament to the next one. Filament gaps ranging from 0.47 mm to 1.07 mm were obtained, as the designed diameter of the filament, d, is 0.38 mm. The spacing was changed every layer by Δs. The central filaments of the scaffolds were aligned, creating two main regions due to the variable offset distance, od. In the centre, the filaments were aligned, as in a uniform aligned scaffold, Figure 32. When moving towards the edges of the scaffold, the change of spacing every layer created a variable offset between the filaments making their centre no longer aligned as in an offset scaffold. However, as the offset distance varies, the load is not always applied at the centre of the over-hang.

Two main types of gradients were created, one with high porosity at the edges and low porosity at the centre, called High Low High (HLH), Figure 32. The other one had low porosity at the edges and high porosity at the centre, called Low High Low (LHL).

Another gradient was created, discrete gradient, where only two spacings were used. This type of gradient was used to study the interface between two distinct spacing regions. It is composed of two uniform aligned scaffolds with different spacing merged in one scaffold. Here, the spacings used were 0.85 and 1.45 mm. Therefore, the spacing was not incremented every layer.

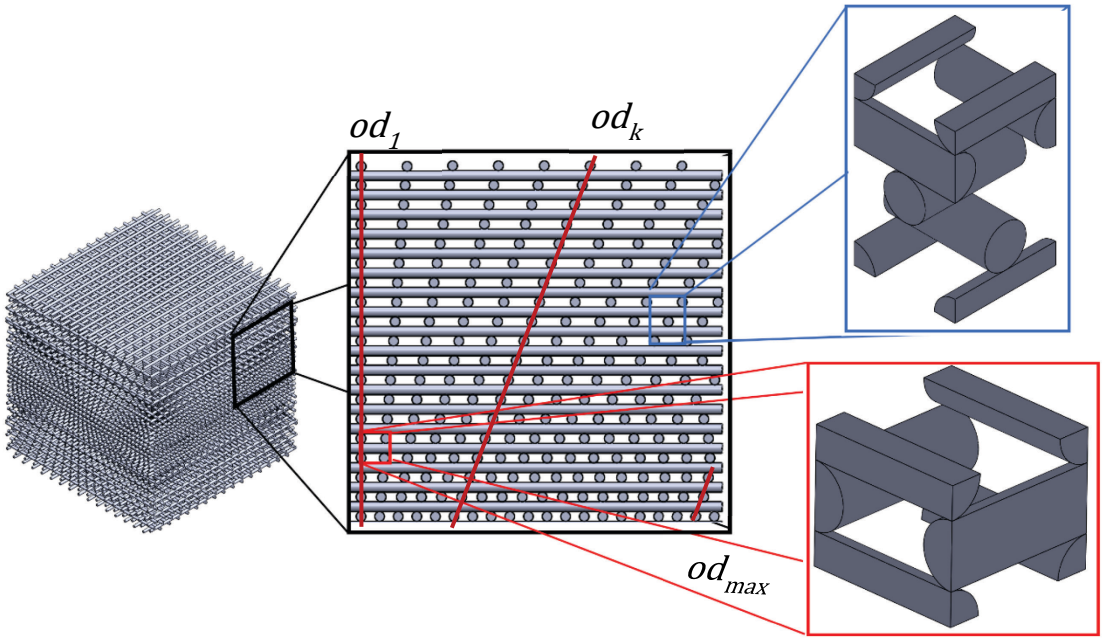

Figure 32 HLH Gradient Scaffold with aligned, offset unit cells and the offset distance at filament 1 and k and maximum offset distance od_{max}. Left Isometric view of an HLH gradient scaffold. Middle Side view of an HLH gradient scaffold showing the different regions in the gradient. Right In blue offset unit cell, in red aligned unit cell.

For the gradient scaffold, the first approach was to consider the deformation mode in a unit cell as a three-point bending of a simply supported beam with an asymmetric point load. From this assumption, the nominal elastic modulus is expressed as:

$$E^* = \sigma\left(\frac{1}{\varepsilon}\right) = \frac{F}{A}\left(\frac{4h}{3\delta_{max}}\right) = \frac{9\sqrt{3}hs\pi\, d^4 E_s}{32s^2(s^2 - od^2)^{3/2}} \quad (8)$$

The offset distance, od, is expressed as:

$$od_k = (k-1)\Delta s \quad (9)$$

Where k is the number of a filament and Δs is the spacing increase.

The offset distance of the filaments k is the same in all the scaffold when two successive layers are considered, Figure 32. When k equals 1, the filament is in the centre of the layer.

The variable offset model shows when the predicted Young's modulus gets lower than the uniform aligned scaffold experimental values. All the values higher than the uniform aligned experimental data will be treated with the aligned model, and all the values lower will be treated with the offset model. The variable offset model allows us to know how many filaments are considered aligned or offset in one layer according to the spacing. The higher the spacing is, the fewer filaments are in the layer, the less offset distance is observed in a layer, as it depends on the number of filaments (Equation 10, 11).

The predicted Young's modulus based on the aligned and offset model are combined within a layer through an iso-strain rule of mixture, as the layer is assumed to deform homogeneously. The Young's modulus of the layer is expressed as follows:

$$E_{Layer} = f_{Strain}E_{Aligned} + (1 - f_{Strain})E_{Offset} \quad (10)$$

With E_{Layer} the apparent Young's modulus of a layer, $E_{Aligned}$ the apparent Young's modulus predicted by the aligned model for the layer and E_{Offset} the apparent Young's modulus predicted by the offset model for the layer.

$$f_{Srtain} = \frac{V_{Aligned}}{V_{Layer}} \quad (11)$$

With f_{Strain} the volume fraction for the iso-strain rule of mixture, $V_{Aligned}$ the volume of aligned filament in the layer and V_{layer} the volume of the layer.

The volume of aligned filament in one layer, $V_{Aligned}$, depends on the variable offset model to determine how many filaments are considered aligned in a layer.

The prediction of the nominal elastic modulus of the gradient scaffold is obtained by homogenizing the modulus obtained for every layer of the scaffold with an iso-stress rule of mixture, as the load applied to the gradient scaffold is assumed homogenous.

$$E^* = \left(\frac{f_1}{E_{layer1}} + \frac{f_2}{E_{layer2}} + \cdots + \frac{f_n}{E_{layer\,n}} \right)^{-1} \quad (12)$$

With f the volume fraction of a layer in the scaffold.

5.2 Results

5.2.1 Mechanical characterisation

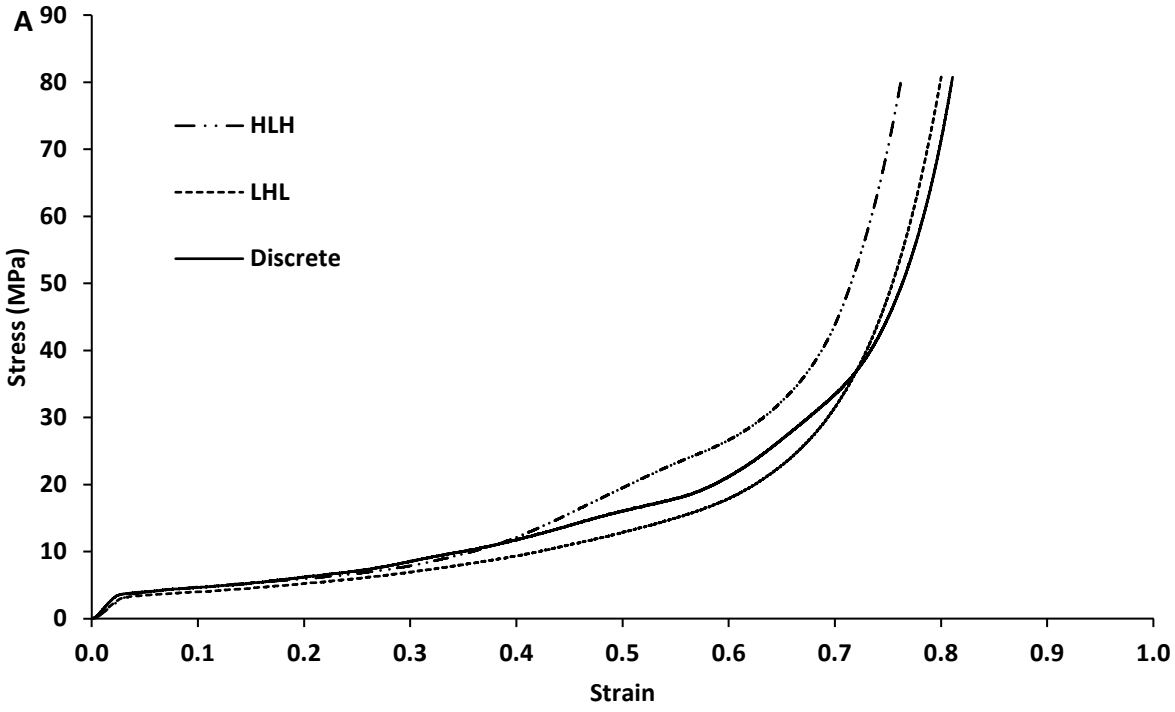

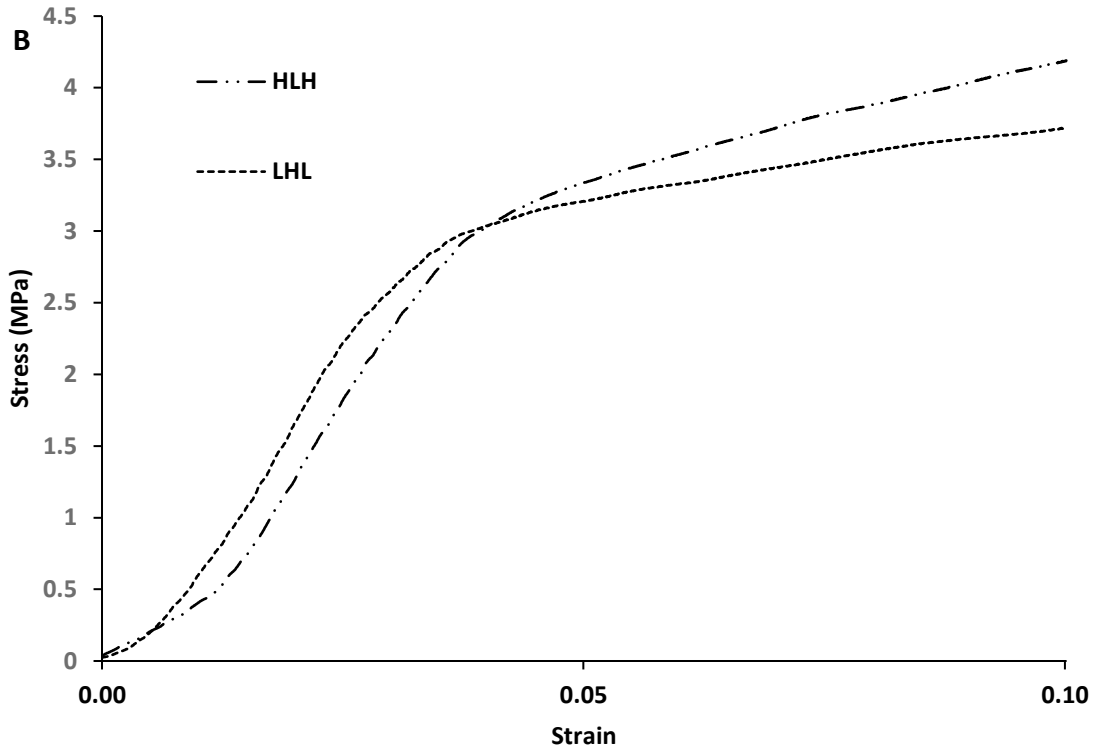

Figure 33. (A) Representative stress-strain curves for gradient scaffolds. HLH: High porosity, Low porosity, High porosity. LHL: Low porosity, High porosity, Low porosity. Discrete: Uniform aligned region with a spacing, s = 0.85 mm, combined with a uniform aligned region with a spacing, s = 1.45 mm. **(B)** Focus on small strain to observe the linear elastic region of gradient scaffolds.

All the gradient scaffolds behave similarly. All the curves exhibit an initial linear region, followed by yield and a flat plateau region, and then a densification region, where the stiffness increases exponentially, Figure 33. However, their linear elastic region differs depending on the architecture. Discrete gradient scaffolds have a steeper linear elastic region, then a higher Young's modulus, 154 MPa (Table 10), than other gradient scaffolds, LHL 110 MPa and HLH 100 MPa.

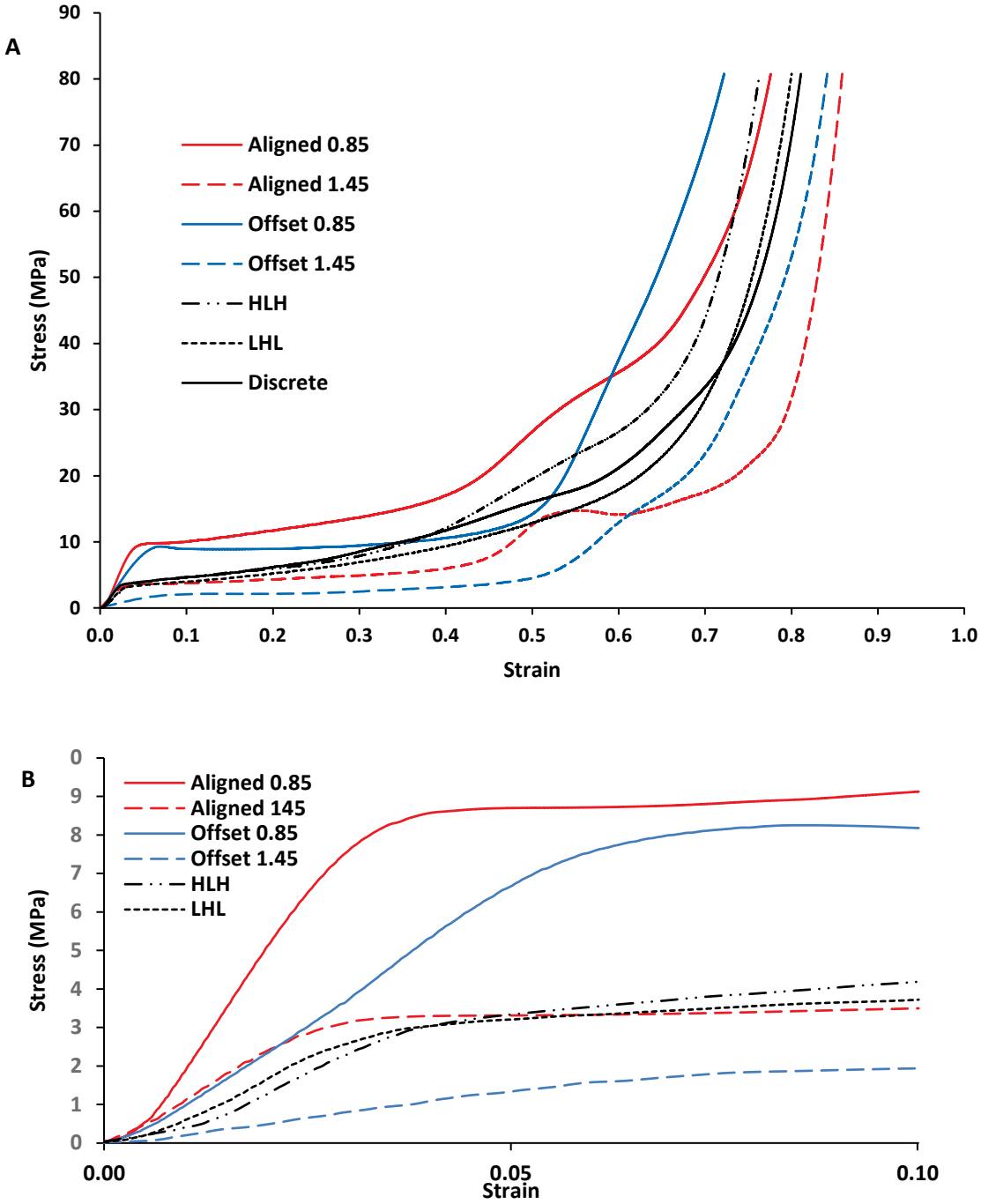

Figure 34 (A) Representative stress-strain curves for gradient scaffolds compared with uniform aligned scaffolds with a spacing, s = 0.85 mm and 1,45 mm and uniform offset scaffolds with a spacing, s = 0.85 mm and 1.45 mm. HLH: High porosity, Low porosity, High porosity. LHL: Low porosity, High porosity, Low porosity. Discrete: Uniform aligned region with a spacing, s = 0.85 mm, combined with a uniform aligned region with a spacing, s = 1.45 mm. **(B)** Focus on small strain to observe the linear elastic region of gradient scaffolds in comparison with uniform aligned (in red) and uniform offset (in blue)

Figure 34 illustrates the difference between the architectures of the different scaffolds. As the spacing limits of the gradient scaffold are 0.85 mm for the lower limit and 1.45 mm for the upper

limit, only uniform scaffolds with a spacing of 0.85 mm and 1.45 mm were plotted. The stress-strain curves of all the gradient scaffolds were plotted. All the curves exhibit an initial linear region, followed by yield and a flat plateau region, and then an increasing densification region. Aligned scaffolds (in red) are stiffer than offset scaffolds (in blue) at the same spacing. In the linear elastic region, gradient scaffolds behave similarly to the uniform aligned scaffolds with the highest spacing, s = 1.45 mm. The gradient stress-strain curves then diverge in the plateau region according to their architecture. The High porosity Low porosity High porosity (HLH) gradient stress-strain curve looks similar to the uniform aligned scaffold with the lowest spacing, s = 0.85 mm, in the densification region.

5.2.2 Gradient model

5.2.2.1 Variable offset model

When the offset distance was too small between the studied filament and the filament two layers below, the Young's modulus obtained from the variable offset model was too high compared to Young's modulus measured for a uniform aligned scaffold at similar spacing. When the offset distance increased and the studied unit cell became closer to the uniform offset model the predictions were still too high compared to the experimental data, see Figures 35, 36, 37 and Table 9. This variable offset model was primarily used to determine when the filaments in a defined layer were more similar to an aligned or to an offset structure. The offset distance at which a filament could be considered as following the offset model got smaller when the spacing increased, as the supporting beam got longer.

At a spacing of 0.85 mm, the transition happened at an offset distance of 0.17 mm, see Figure 35 and Table 10. At a spacing of 1.2 mm, the transition happened at an offset of 0.136 mm, see Figure 36 and Table 9. At a spacing of 1.45 mm, the transition happened at an offset distance of 0.102 mm, see Figure 37 and Table 9.

Table 10 Variable offset model prediction (left), compared to the experimental results (right). The values in red are associated with the aligned model. The values in blue are associated with the offset model.

Variable Offset Model

		Spacing (mm)		
k	**od (mm)**	**0.85**	**1.2**	**1.45**
1	0			
2	0.034	3063.86	1263.65	802.96
3	0.068	1117.27	456.52	289.04
4	0.102	627.68	254.00	160.22
5	0.136	421.05	168.68	106.00
6	0.17	311.38	123.45	77.27
7	0.204	245.00	96.09	59.90
8	0.238	201.24	78.05	48.45
9	0.272	170.63	65.41	
10	0.306	148.26	56.15	
11	0.34	131.36		
12	0.374	118.27		
13	0.408	107.92		
14	0.442	99.62		

Experimental

	Spacing (mm)		
	0.85	**1.2**	**1.45**
Aligned	281.08	148.54	117.64
Offset	163.05	46.5	25.44

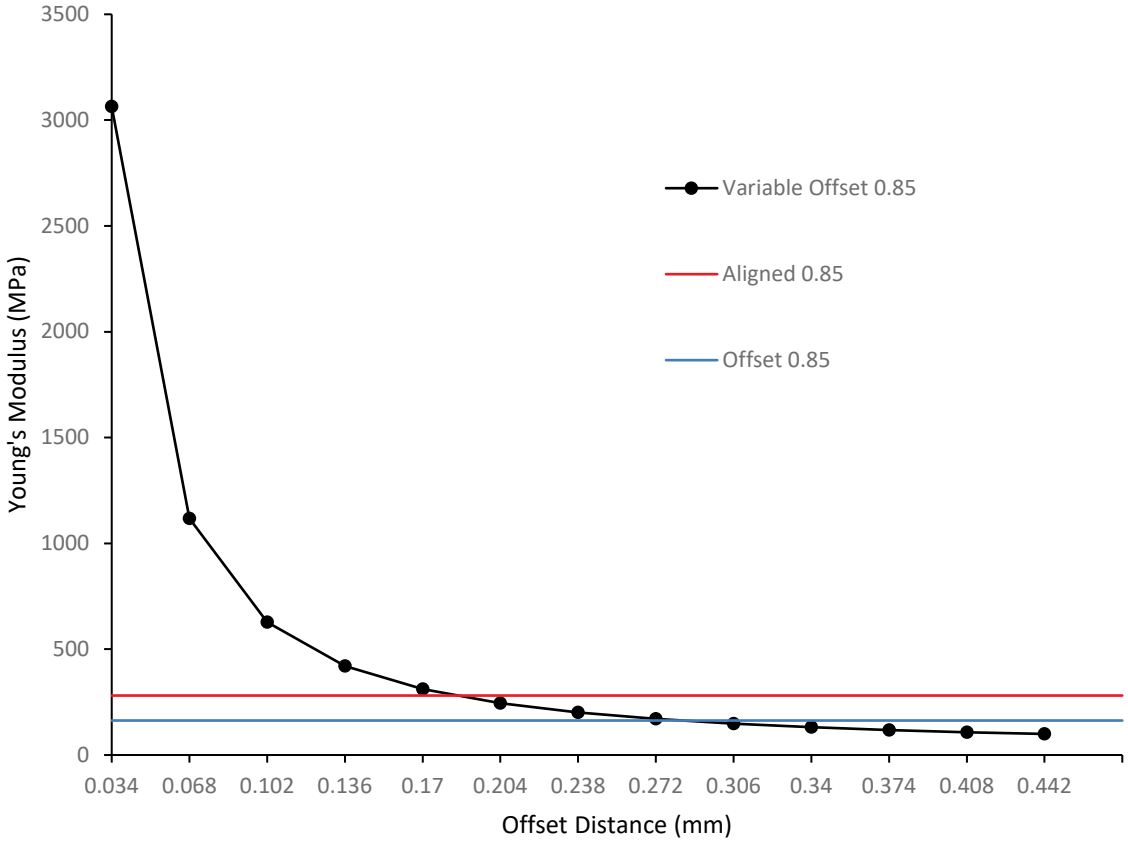

Figure 35 Comparison of the variable offset model prediction of the Young's modulus function of the offset to the aligned (in red) and offset (in blue) models at a spacing of 0.85 mm.

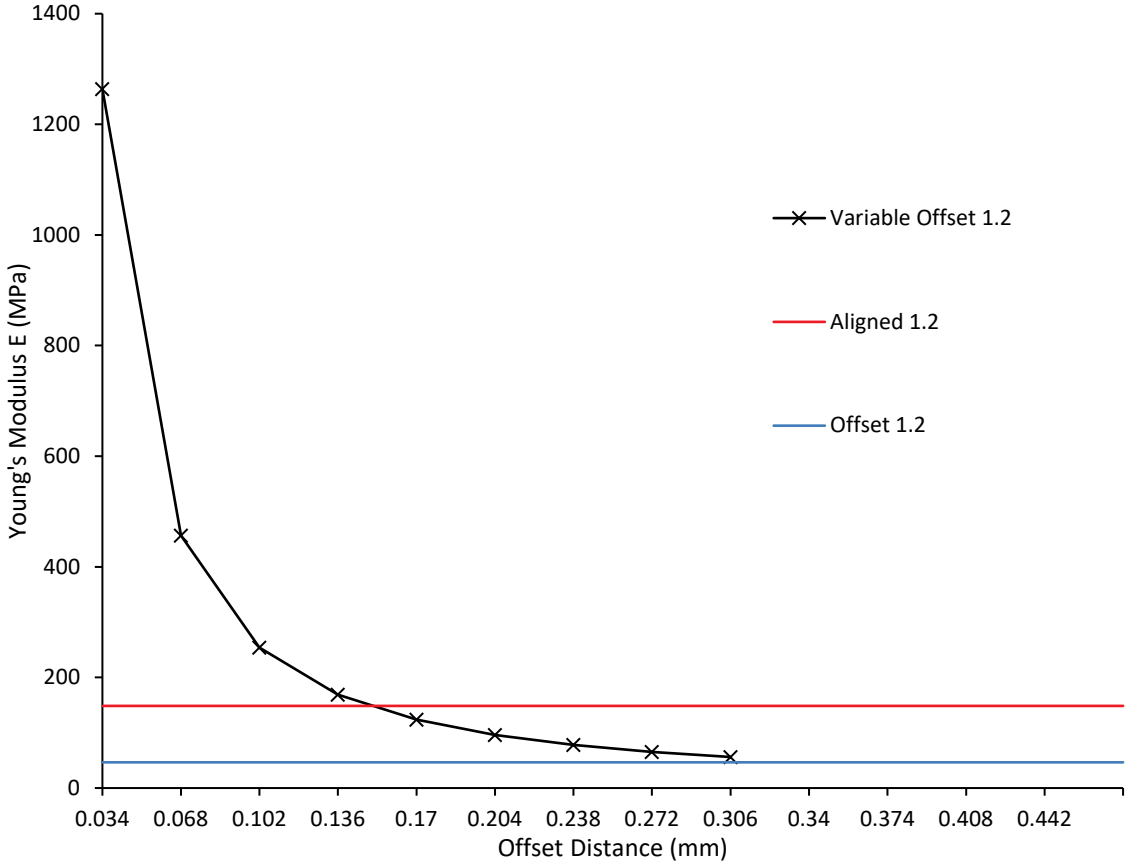

Figure 36 Comparison of the variable offset model prediction of the Young's modulus function of the variable offset to the aligned (in red) and offset (in blue) models at a spacing of 1.2 mm.

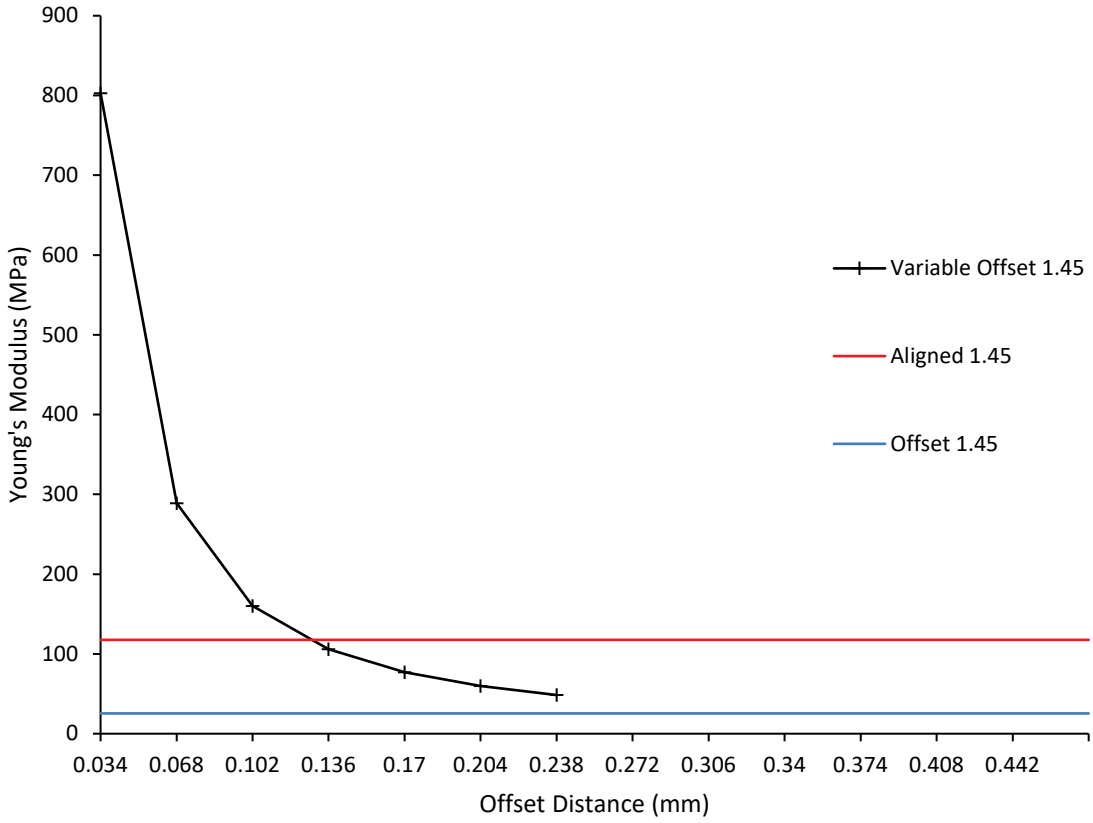

Figure 37 Comparison of the variable offset model prediction of the Young's modulus function of the offset distance to the aligned (in red) and offset (in blue) models at a spacing of 1.45 mm.

5.2.2.2 Rules of mixture

The predictions, obtained with the rule of mixture, for the gradient scaffolds have a maximum deviation of 12.5 % for Low High Low porosity gradient and a minimum of – 1.9% for the discrete gradients, Table 11. The predictions are assuming that one layer will deform as a whole and show the same train at different locations.

Table 11 Experimental results for PLA gradient scaffolds and their prediction.

PLA	Sample 1 (MPa)	Sample 2 (MPa)	Sample 3 (MPa)	Prediction (MPa)	Deviation (%)
HLH 1.45-0.85 1.45	105.03	92.63	108.92	116.73	+ 12.5
LHL 0.85-1.45-0.85	111.67	114.08	115.39	116.73	+ 2.6
Discrete 0.85-1.45	154.76	153.58	155.91	151.73	- 1.9

5.3 Discussion

The gradient scaffolds, HLH and LHL, have Young's moduli around 110 MPa. Even though being a combination of aligned and offset regions, they behave, in their linear elastic region, like the uniform aligned scaffolds with a porosity corresponding to the upper limit of the gradient, here the uniform aligned scaffolds with a spacing of 1.45 mm and a Young's modulus 118 MPa. For the variable offset model, the offset region is more represented at lower spacing due to a higher number of offset filaments within a layer, Table 10. The Young's modulus of uniform offset scaffolds at a spacing of 0.85 mm, around 160 MPa, is higher than the Young's modulus of uniform aligned scaffold at a spacing of 1.45 mm, around 110 MPa. When the values are averaged for the whole scaffold, the result is close to 120 MPa, the Young's modulus of the uniform aligned scaffold at a spacing of 1.45 mm. The uniform aligned scaffold with a spacing corresponding to the upper limit of the gradient defines the stiffness of the gradient. Although, Figure 38 shows that the uniform offset model gives a prediction close to the experimental value at the average porosity of the gradient scaffolds.

The offset filaments will deform by bending as described by Cuan Urquizo et al. following the work of Ashby and Gibson on open cell foam. They will deform more easily than the aligned filaments that are directly supported by the previous layers. This alignment creates pillars inside the scaffold that deform under compression. As the result the aligned filaments will not bend, and they will deform at higher strains compared to the offset filaments. The deformation of the offset structure is only possible if the supporting filament can be considered as a slender beam, a long and thin beam. This is solved using the Timoshenko correction. However, in gradient scaffolds the other challenge comes from the variable offset distance. If the studied filament is too close to the filament two layers below, their centres should be separated by a distance at least equal to the diameter of one filament, then it will not be able to bend and it will deform like the aligned filaments, under compression. This issue can be addressed by using a variable offset model, like the one used by Cuan Urquizo et al., that will allow to cover the full range of offset distances found in a gradient scaffold.

The Young's modulus obtained with the prediction is the same for LHL and HLH. The experimental results are different. HLH gradient, with a Young's modulus of 104 MPa, is less stiff than LHL gradient, with a Young's modulus of 114 MPa. This difference might be due to the test protocol and

to the fact that having edges with a higher porosity make them more fragile and they will be compressed faster at low strain.

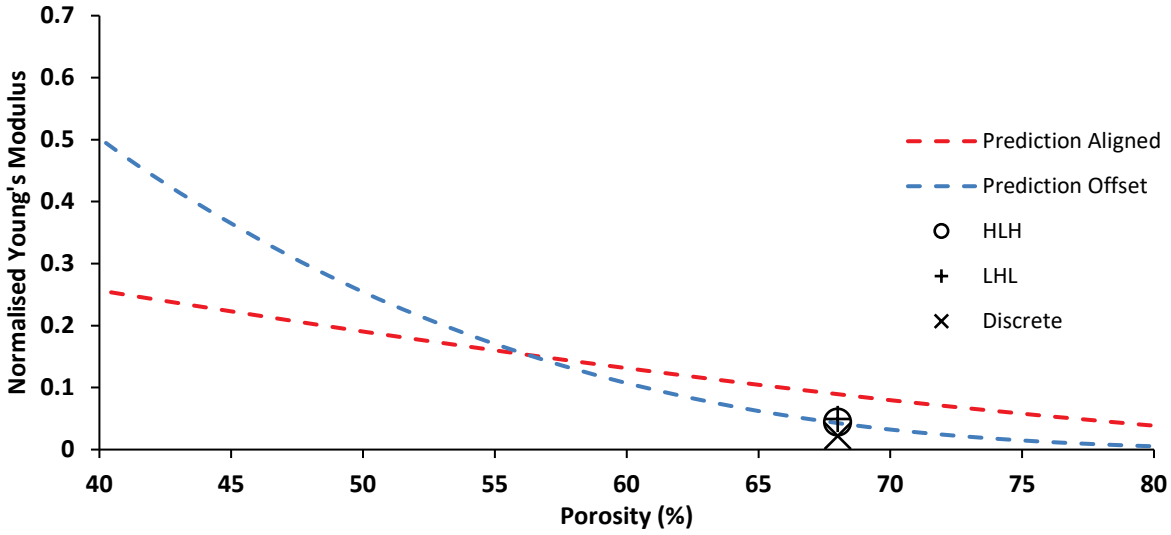

Figure 38 Normalised Young's modulus of the different gradient scaffolds: HLH, LHL and discrete function of their porosity. The prediction for the aligned scaffolds is obtained with Norato's model and is plotted in red. The prediction for the offset scaffolds is obtained with Cuan Uquizo's model and is plotted in blue.

The use of the rule of mixtures gives acceptable results. However, the model could be further improved to consider the variable offset as the one developed above tends to overestimate the apparent Young's modulus for a given offset. The model used by Cuan Urquizo to predict the properties of asymmetric scaffolds with a variable offset seems to be an interesting path to explore and to further improve the model. They submitted the woodpiles shown in Figure 39 to compressive loading[68]. Their structures were composed of filaments with diameters of 1 mm, and the spacing between filaments was 10 mm. Their arrangements were such that filaments did not lie at the mid-point of the overhang. This location was controlled using the parameter, a, corresponding to the offset distance, od, which is defined as the length from the left filament to the location of the offset filament. The lattice shown in Figure 39 corresponds to a ratio of the offset distance to the spacing of 0.7. They compared their periodic beam model to other models and finite element analysis (FEA) data. The solid line corresponds to the model based on the periodic beam. The agreement between the periodic beam model and the FEA data validates the boundary conditions they used to develop their model. The dotted lines in Figure 40 are the upper and the lower bounds for the apparent Young's modulus. The correct response lies between these two, and thus is close the response predicted with the periodic beam model.

The use of the rule of mixtures takes into account the extreme case where the filament is aligned by replacing the equation of variable offset by the one used to predict the apparent properties of uniform aligned scaffolds. Although is still limited to the cases where the beam is long enough to allow the filament to bend. Therefore, when the ratio of the offset distance, od, by the spacing, s, is close to 0 or 1 the prediction becomes more complex.

The combination of the rule of mixtures with an improved variable offset model should yield better results and should be considered for future works. This perspective will be discussed in the chapter 7.

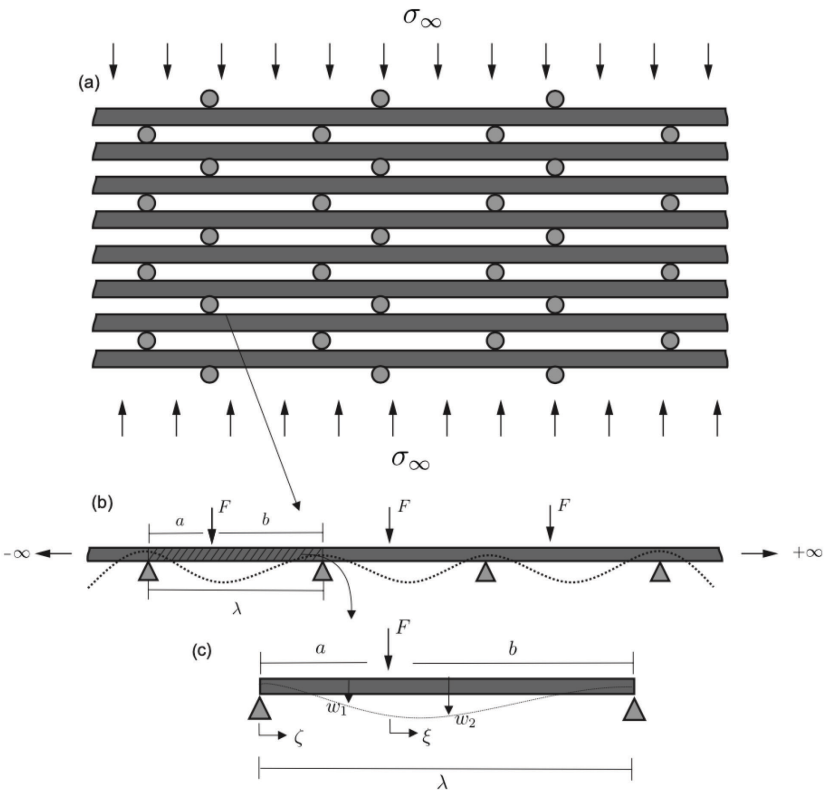

Figure 39 (a) Schematic of the asymmetric staggered arrangement developed by Cuan Urqizo. (b) and (c) show the periodic beam and the free body diagram for the analysis derived from Cuan Urqizo's work[84].

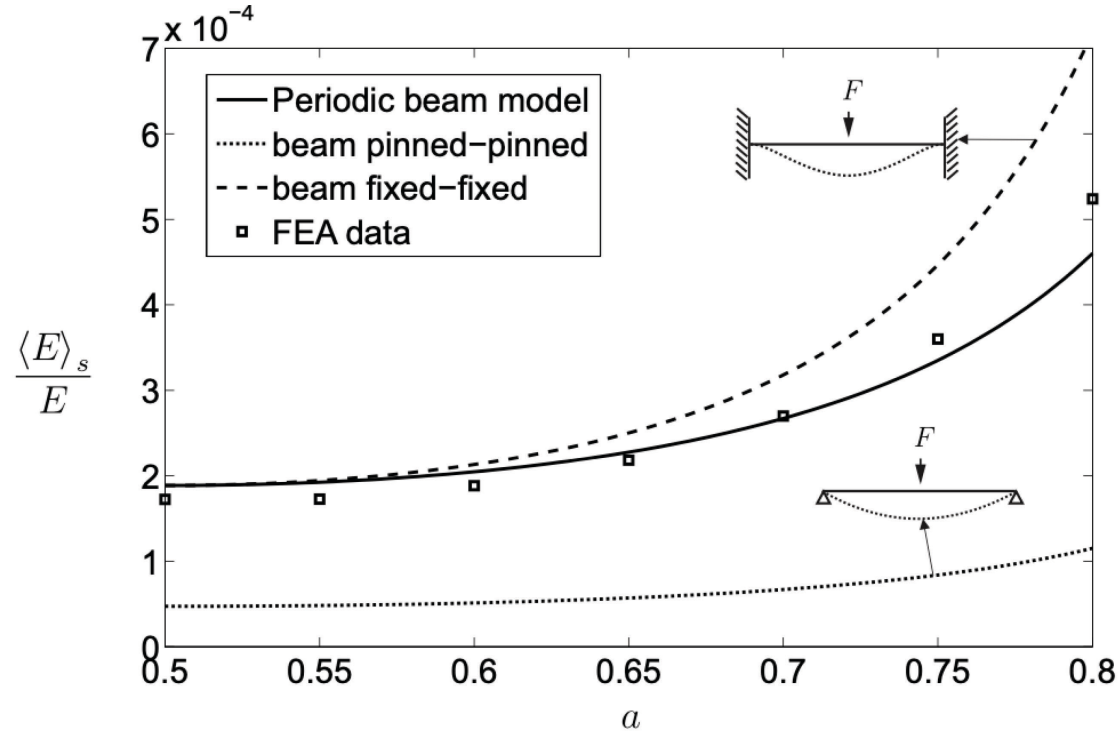

Figure 40 Comparison of Cuan Urquizo models for a beam pinned-pinned condition, fixed-fixed condition, a periodic beam and the FEA data.

The understanding of the phenomena at staked when the ratio of the offset distance by the spacing is close to zero is crucial to develop an accurate model. In the previous chapter, the contact between the filaments was highlighted as one of the parameters playing an important role in the prediction of the apparent mechanical properties of lattice scaffolds. Therefore, the next chapter is dedicated to the study of printing parameters that could impact this parameter in the hope to better understand the evolution of the contact area between the layers according to the temperature, the printing speed, the layer height and the offset distance.

5.4 Conclusion

The stiffness of bone tissue engineered scaffolds with a porosity gradient was studied. Two different approaches were combined to develop an analytical model to predict the apparent Young's modulus of the scaffolds. The model was based on the beam theory to describe the filament mechanics. The analytical predictions were compared against experimental results. An iso-strain rule of mixture was used to combine the models developed by Norato[69] and Cuan Urqizo[68] and studied in the previous chapter. A variable offset model was used to determine how many filaments in one layer were following the uniform aligned model or the uniform offset model.

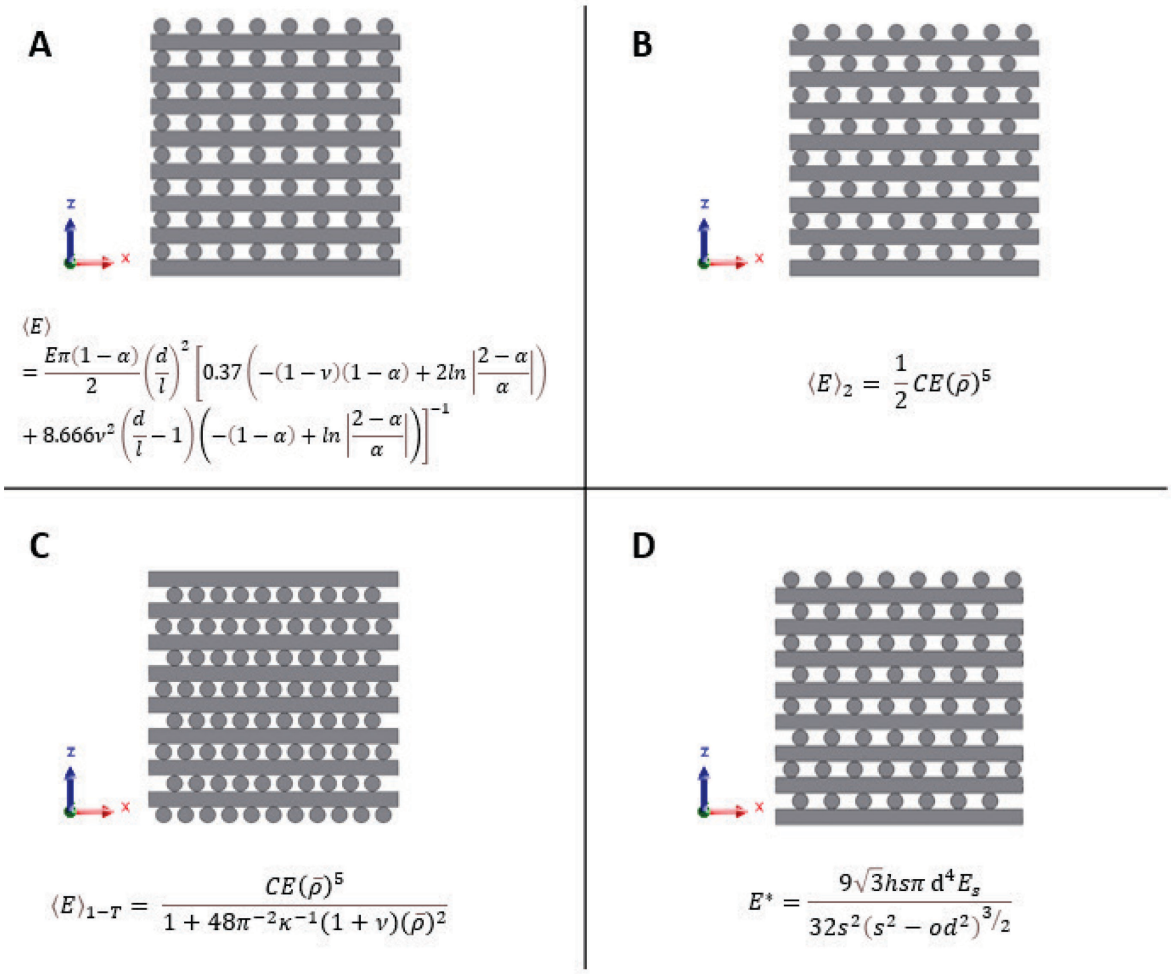

Figure 41 A Uniform aligned scaffold and the equation from Norato et al. to calculate its apparent Young's modulus. **B**. Uniform Offset Scaffold with a low relative density, spacing 1.45mm, and the equation from Cuan Urquizo et al. to calculate its apparent Young's modulus. **C**. Uniform offset scaffold with a high relative density, spacing 0.65 mm, and the equation including the Timoshenko correction from Cuan Urquizo et al. to calculate its apparent Young's modulus. **D.** Variable Offset Scaffold and the equation used to calculate its apparent Young's modulus.

The combined approach with a rule of mixture gave a prediction 12.5 % higher in the case of the HLH scaffold and was the worst-case scenario. The main problem of this approach is that it does not capture the difference between a highly porous and a denser scaffold centre if the gradient spacing limits are the same. Although, it was possible to predict the apparent Young's modulus of different configuration as shown with the discrete scaffolds.

From the mechanical characterisation, a tendency of the gradient scaffolds to behave like the uniform aligned scaffolds with a spacing corresponding to the upper limit of the gradient was

observed. Even though, the apparent Young's modulus of the gradient scaffolds was closer to the uniform offset model prediction, see Figure 41. The offset filaments will bend, and the aligned filaments will support the structure at a low strain corresponding to the linear elastic region of the gradient scaffolds. Then, at a higher strain the offset filament will enter in contact with the previous layer and their behaviour will be similar to the aligned filaments. The aligned filaments will increase the stiffness of the scaffold as they deform under compression. As the gradient scaffolds are mainly composed of offset filaments it gave more weight to the offset model. Unfortunately, it was not possible to compare the experimental data with the literature as there is no mention of mechanical results for similar scaffolds made with thermoplastics.

These initial findings show that a rule of mixture could be suitable to predict the properties of graded scaffolds. The model could be refined by using a different variable offset model capturing more parameters. The use of Cuan Urqizo's periodic beam model seems like the next logical step to improve the predictions. More experimental data with different graded scaffolds configuration varying the spacing limits, the spacing increase, or the disposition of the filament in the layer are required to confirm these results.

Chapter 6 Printing Parameters

6.1 Introduction

Kuznetsov et al. offered a new methodology for researching the influence of material process parameters on the mechanical properties of parts printed with FDM, highlighting that the standards are not applicable to FDM printing technology[73]. Following their methodology, they found that layer height had the greatest influence on intra-layer adhesion. The part strength decreased along with layer height increase for nozzles with a diameter of 0.4, 0.6 and 0.8 mm. They also found that the nozzle diameter had a significant influence on interlayer cohesion. For a constant layer height, printing with a larger nozzle resulted in increased strength.

Abbott et al. studied the relationship between print parameters, thermal history, mesostrucutre and tensile strength with design of experiment methodology for ABS filament. The increase of the print speed negatively affected the tensile strength and the contact length. An increase in extruder temperature resulted in a minor increase in tensile strength and contact length. The effect of layer height on contact length was found to yield higher tensile strength for XY orientation due to increased contact length between neighbouring roads. One of their key findings was the relation between the strength plateau and the contact length. The implication of this result is that a structure can be designed to be less than fully dense without sacrificing interlayer strength and therefore contribute to weight savings or increased cell proliferation. There is not a set of universal print parameters that will generate optimal properties. The designer should consider the build orientation and the print parameter selection.

Zhang et al. proposed a three-dimensional transient mathematical model of temperature variation with respect to space and time for fused deposition modelling. The considered sample is a cuboid at fixed raster angled of 0(90°) and filling ratio of 100%. In their study, the printing speed is predicted to be positively correlated to mechanical properties of constructed components through the mechanism of thermal coalescence. Even though they neglect the influence of heat radiation, and they consider the manufactured component pore-free, they showed that the reheating effect of a deposited raster by a newly deposited one is universal and happened mainly in the layer thickness direction. They also demonstrated the importance of temperature settings (temperature of extruder, temperature of heat bed and environment) in the control of the overall cooling rate to

reduce internal stresses and promote interlayer bonding. They concluded that the higher the layer thickness of printing the lower the overall cooling rate. Their conclusions go against Abbott et al. or Kuznetsov conclusions concerning the interlayer bonding.

Coogan and Kazmer modelled the interlayer contact and contact pressure during fused filament fabrication[75]. They found out that small layer height contributed most significantly to increasing the exit contact pressure, which is responsible for forcing the new layer into intimate contact with the previous layer. The contact pressure was found to directly correlate with interlayer contact, so contact pressure is expected to be a critical determinant of the final part strength. Their model aims at predicting contact length, providing a crucial missing piece toward a comprehensive FFF strength model by outperforming bond width predictions based purely on conservation of volume given by the printing geometry. For the range of processing parameters they explored, pressure-driven intimate contact was a critical contributor for interlayer contact while wetting growth had a nearly negligible influence.

Already in 2016, Faes et al. highlighted the importance of the interlayer cooling on the mechanical properties of components produced via Fused Deposition Modeling[79]. They varied the interlayer cooling time by changing the number of parts built at a time and performed tensile tests. They discovered an inverse correlation between the inter-layer cooling time and the ultimate tensile strength. They attributed this phenomenon to the prolonged cooling of the deposited material which resulted in weaker interlayer bonding. However, they acknowledged the lack of thermal monitoring. Their finding supports that higher printing speed should result in stronger interlayer adhesion due to shorter cooling time.

Gao et al. considered the crystallisation of the polymer in their review of the interlayer bond[85]. They concluded that for amorphous and semi-crystalline polymers the interlayer bond quality is a function of the bond time provided by the FFF process and depends on the polymer. They suggested that both process control and polymer modification could improve the bond interface by facilitating molecular diffusion and entanglement between adjacent strands. They concluded that to get an effective entanglement the material properties should be carefully designed.

6.2 Results

6.2.1 Printing parameters

6.2.1.1 Extruder temperature

The contact area between the layers of the scaffolds was measured through optical microscopy. When the temperature of the extruder was set to 190°C the average observed contact area was 0.0481 mm^2 for the previous layer, cold as it was deposited earlier, and 0.0512 mm^2 for the new layer, warm at the moment of the bond formation. The observed contact area was larger when looking at the newly deposited layer, see figure 42. For an extruder temperature of 210°C, the observed contact area was 0.0477 mm^2 for the previous layer and 0.0503 mm^2 for the new layer. The observed contact area was 0.0456 mm^2 for the previous layer and 0.0475 mm^2 for the new layer when the extruder temperature was set to 240°C. However, no significant difference in the contact area can be related to the change in extruder temperature.

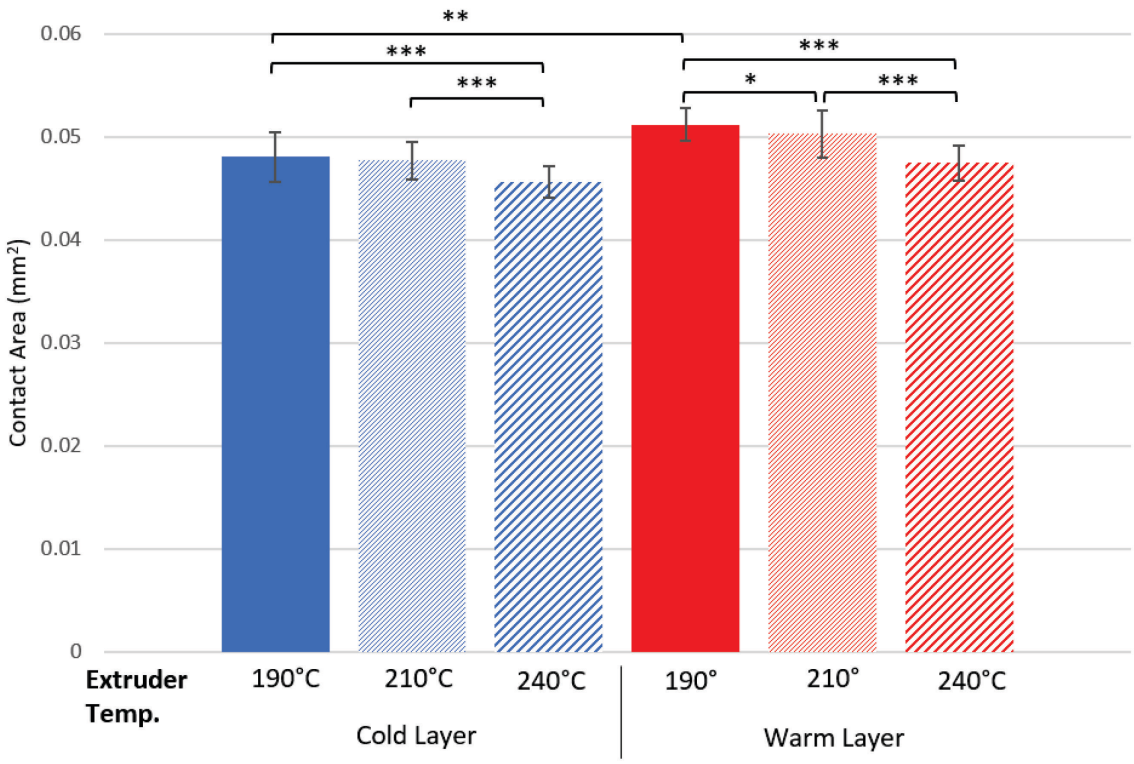

Figure 42 Contact area function of the extruder temperature in degree Celsius. The left part, in blue, corresponds to a deposition on a cold layer. The right part, in red, corresponds to the deposition on a warm layer. * = $p < 0.05$, ** = $p < 0.01$, *** = $p < 0.001$.

6.2.1.2 Layer height

For a layer height of 0.35 mm the observed contact area is 0.0477 mm^2 for the cold layer during the print and 0.0503 mm^2 for the newly deposited warm layer, see figure 43. The measured contact areas range from 0.0284 mm^2 to 0.0981 mm^2. For a layer height of 0.2 mm the observed contact area is 0.151 mm^2 for the previous layer and 0.156 mm^2 for the new layer. The measured values range from 0.124 to 0.199 mm^2. The reduction of the layer height has a direct impact on the increase of the contact area. When reducing the layer height by 43%, an increase of 300% of the contact area can be observed.

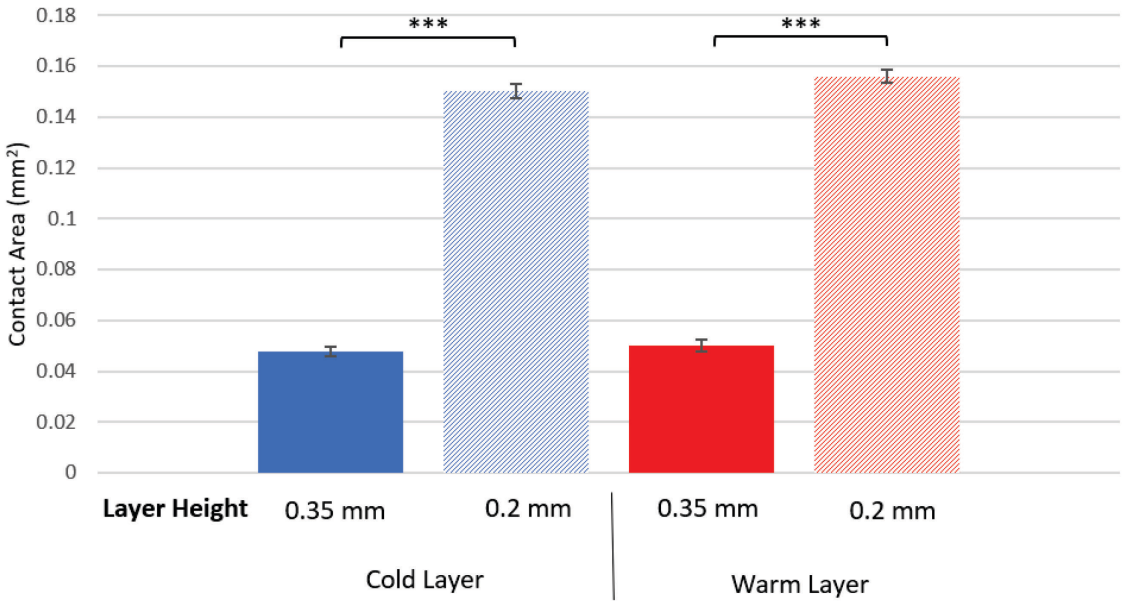

Figure 43 Contact area function of the layer height. The left part, in blue, corresponds to the deposition on a cold layer. The right part, in red, corresponds to the deposition on a warm layer. * = $p < 0.05$, ** = $p < 0.01$, *** = $p < 0.001$.

6.2.1.3 Printing speed

The control printing speed was 20 mm/s and the observed contact area was 0.477 mm^2 for the previous layer, that had time to cool down, and 0.0503 mm^2 for the new layer, warm when deposited. The contact areas were similar in the whole layer, no significant difference could be observed, see figure 44. When the printing speed was divided by 4, the average observed contact area was 0.0317 mm^2 for the previous layer and 0.0348 mm^2 for the new layer. The contact areas were similar over the whole layer. When the printing speed was multiplied by 3, the average observed contact area was 0.0746 mm^2 for the previous layer and 0.0805 mm^2 for the new layer. The contact areas were varying between 0.0054 mm^2 and 0.116 mm^2 at the edges of the layer and between successive filaments.

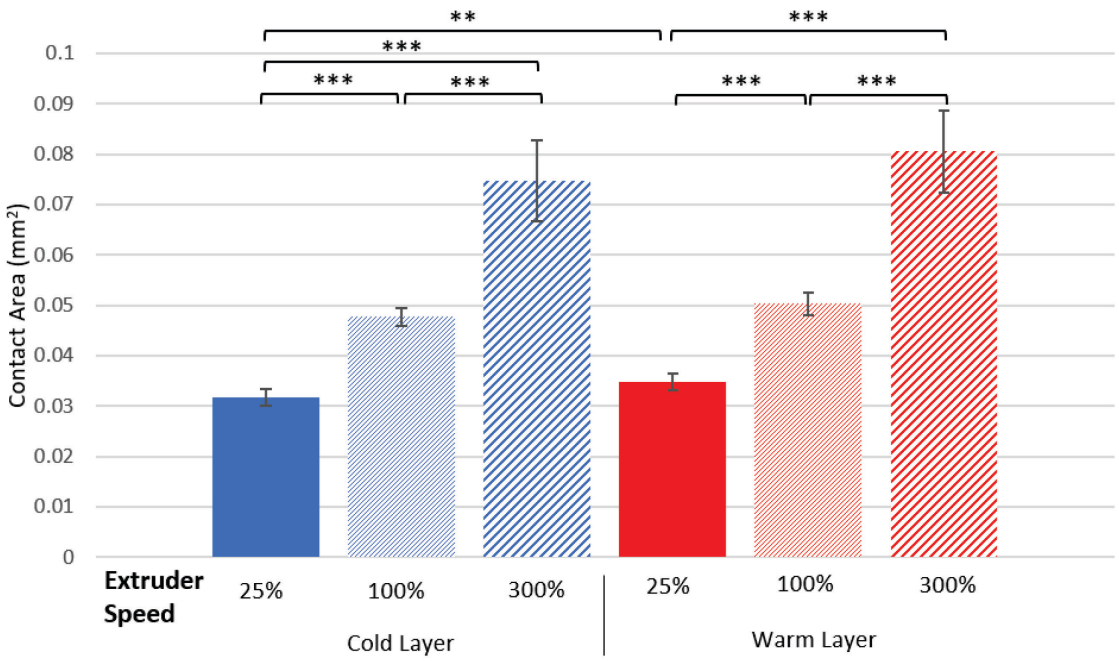

Figure 44 Contact area function of the extruder speed. The left part, in blue, corresponds to the deposition on a cold layer. The right part, in red, corresponds to the deposition on a warm layer. * = $p < 0.05$, ** = $p < 0.01$, *** = $p < 0.001$.

6.2.1.4 Offset

When an offset is introduced between the layers, the average observed contact area is 0.0385mm^2 for the previous layer, that had time to cool down, and 0.0384 mm^2 for the new layer, that is warm when deposited, see figure 45. The variability of the contact area across the layer is, 0.00083 mm^2, and can be considered small. The introduction of an offset between the layer results in a significant decrease of the contact area.

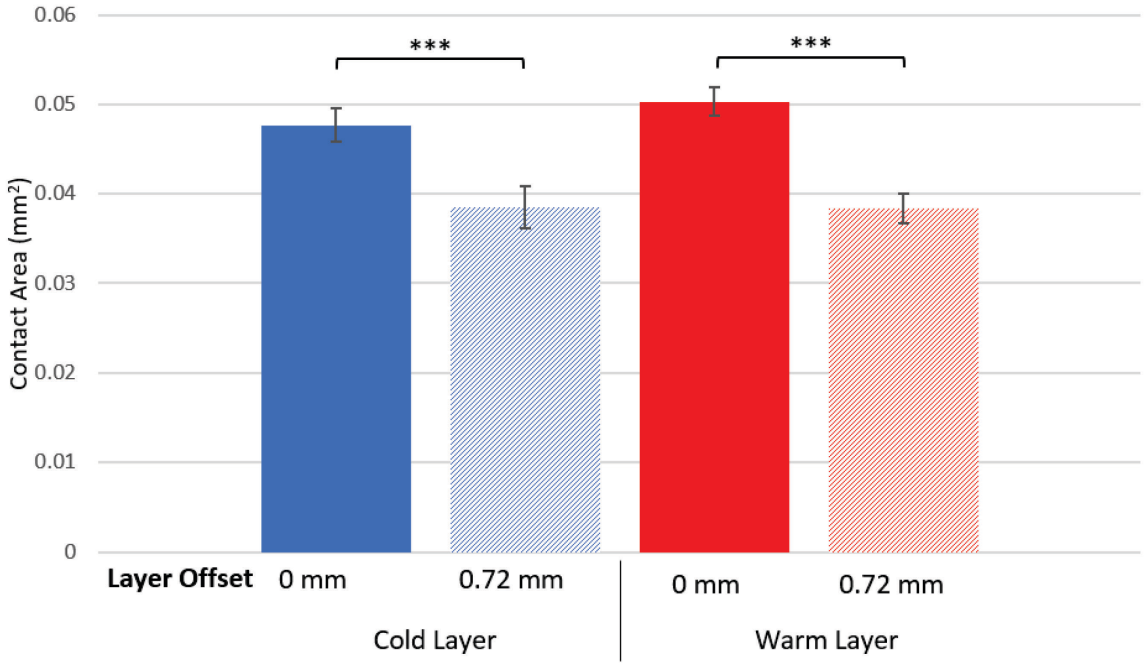

Figure 45 Contact area function of the presence or absence of an offset between the filaments. The left part, in blue, corresponds to the deposition on a cold layer. The right part, in red, corresponds to the deposition on a warm layer. * = $p < 0.05$, ** = $p < 0.01$, *** = $p < 0.001$.

Table 12 Observed Contact Area with standard error for all the printing parameters.

Contact Area (mm2)	**Previous Layer**	**New Layer**
Extruder Temperature (°C)		
190	0.0481 ± 0.0024	0.0512 ± 0.0016
210	0.0477 ± 0.0019	0.0503 ± 0.0023
240	0.0456 ± 0.0016	0.0475 ± 0.0018
Layer Offset (mm)		
0	0.0477 ± 0.0019	0.0503 ± 0.0023
0.72	0.0385 ± 0.0016	0.0384 ± 0.0017
Extruder Speed (20 mm/s)		
25% (5 mm/s)	0.0317 ± 0.0017	0.0348 ± 0.0016
100% (20 mm/s)	0.0477 ± 0.0019	0.0503 ± 0.0023

300% (60 mm/s)	0.0746 ± 0.0081	0.0805 ± 0.0082
Layer Height (mm)		
0.35	0.0477 ± 0.0019	0.0503 ± 0.0023
0.2	0.151 ± 0.0029	0.156 ± 0.0027

6.2.2 Mechanical characterisation

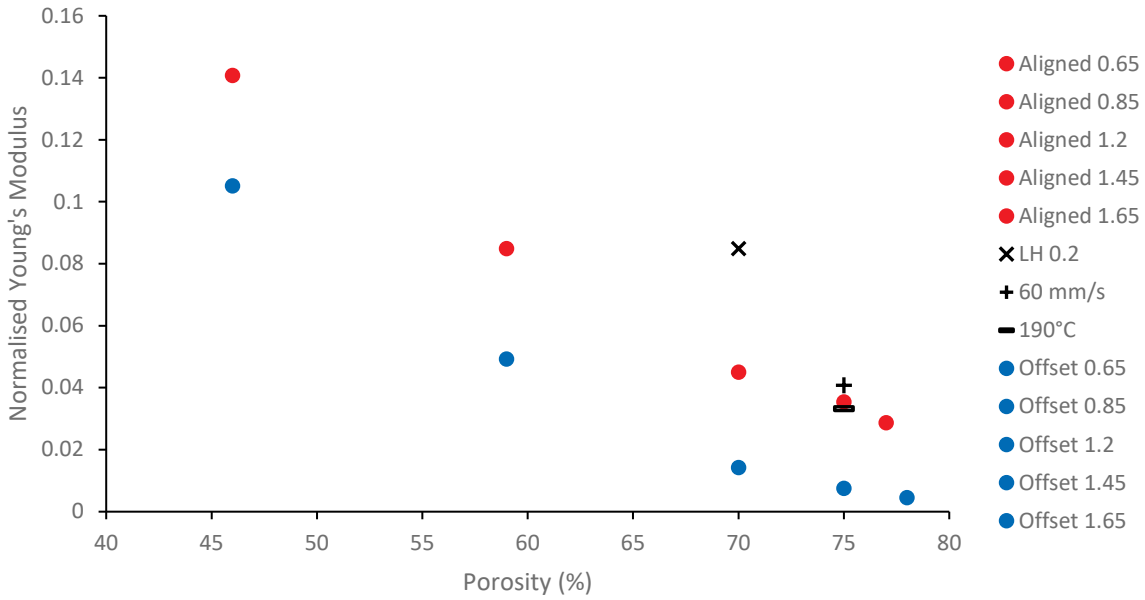

Figure 46 Normalised Young's modulus function of the porosity. The uniform aligned scaffolds at different spacings are in blue. The uniform offset scaffolds with different spacings are in blue. The uniform aligned scaffolds with different printing parameters are in black.

Figure 46 shows the normalised Young's modulus of uniform aligned scaffolds with a spacing of 1.45 mm printed with the different printing parameters discussed above compared to uniform aligned scaffolds and uniform offset scaffolds.

As shown above, a lower printing temperature does not impact the contact area and therefore the stiffness. The scaffolds printed at 190°C have a similar Young's modulus to the ones printed at 210°C.

A higher printing speed results in a larger contact area. This increase in the contact area has a small impact on the Young's modulus of the scaffold. The introduction of an offset distance has a bigger impact on the Young's modulus has it also impacts the mechanics of the scaffold.

The layer height has the highest impact on Young's modulus of the scaffolds. The decrease of the layer height results in a lower porosity, similar to uniform aligned scaffolds with a spacing of 1.2 mm. Although, the Young's modulus of the scaffolds with a lower layer height of 0.2 mm is equivalent to the modulus of uniform aligned scaffolds with a spacing of 0.85 mm.

6.3 Discussion

6.3.1 Extruder temperature

According to the literature, increasing the extruder temperature allows the filament to spend more time above its glass transition temperature. Above the glass transition temperature, the polymer is liquid a bond is formed with the previous layer through thermal coalescence. According to Aid et al.[86], the coalescence of polymer particles is highly dependent on the time. At constant temperature, in 300s two polymer particles can go from distinct to fully merged. However, the enclosure of the printer is open, and the environment temperature is not controlled. The print is created in an environment at room temperature (around 25°C) and the polymer cools down quickly as shown by Zhang et al.[78]. The effect of the extruder temperature on the contact area cannot be observed with this experimental set up. A controlled enclosure allowing a higher environment temperature is required to see the effect of the extruder temperature on the contact area.

6.3.2 Layer height

The layer height defines the thickness of a layer and therefore the contact pressure between the extruder and the previous layer. Coogan and Kazmer showed that small layer heights contribute mots significantly to increasing the exit contact pressure, which is responsible for forcing the new layer into intimate contact with the previous layer[75]. Contact pressure was found to directly correlate with interlayer contact, so contact pressure is expected to be a critical determinant of the final part strength. Pressure-driven intimate contact was a critical contributor for interlayer contact while wetting growth had a nearly negligible influence. The experimental results corroborate Coogan and Kazmer's observations with a three-fold increase in the observed contact area

compared to the control. Although, the reduction of the layer height decreased the accuracy of the print due to the diameter of the extruder (0.4 mm) and to the constant bridging in the scaffolds. The interconnectivity of the scaffold, essential for cell proliferation might be impacted. These problems could be solved by an adjustment of the extruder flow. The amount of material used to create the scaffold is more important as the layer height is smaller, reducing the porosity.

Naghieh et al. obtained a direct correlation between layer penetration and elastic modulus as a linear increase. It is possible to obtain higher Young's moduli with the same porosity by decreasing the size of the struts. They also showed that the strut diameter impacted the layer penetration and the mechanical properties[87]. The strut diameter also impacts the layer height, and it would be interesting to change the diameter of the filaments by using nozzles with different diameters to see the impact on the interlayer adhesion. Unfortunately, only scaffolds with a 0.4 mm nozzle diameter were printed.

To conclude, the decrease of the layer height will increase the stiffness of the scaffold at the cost of the porosity and pores interconnectivity.

6.3.3 Printing speed

By decreasing the speed of the extruder, its temperature should increase the environment temperature and positively affect the thermal coalescence by radiation. However, the experimental observation of interlayer contact area showed a decrease in the bond dimensions. Zhang et al. in their numerical investigation of the influence of process conditions on temperature variation in fused deposition modelling concluded that the higher the printing speed, the lower the overall cooling rate[78]. By increasing the printing speed, the mean temperature of the component upon finishing is higher. Higher mean temperature of the component is beneficial for inter-layer coalescence and correlates to higher mechanical performance[88]. The inter-layer cooling time is reported to be negatively correlated with mechanical properties of FDM constructed components[79]. The influence of printing speed is rarely studied, this study would predict printing speed to be positively correlated to mechanical properties of FDM constructed components, assuming no rheological problems. The experimental results show an increase of the contact area when the printing speed is increased as predicted by Zhang et al[78]. However, the inhomogeneity of the layer due to an insufficient flow rate across the whole layer prevent us from drawing any meaningful conclusion from this experience. The investigation of the impact of the cooling time on

the contact area is required to get a better understanding of the printing speed influence on the thermal coalescence of the layers.

Also, an excessive printing speed (above 100 mm/s) could result in poor adhesion of the newly deposited layer due to an extensive stretching of the filament.

6.3.4 Offset

The introduction of an offset between the filaments of the layer n and the layer n+2, partially removes the support by allowing more bending of the filament in the layer n+1. This bending results in a decreased contact area compared to the control where all the filaments are aligned. This phenomenon is rarely studied in term of interlayer adhesion. The study of micromechanical model shows that this phenomenon can be neglected in bending, the contact area can be neglected for the prediction of the Young's modulus[84]. Although, the decrease of the contact area resulting from the offset becomes more important when considering gradient scaffolds model. To fully understand the mechanical behaviour of gradient scaffolds, the analysis of a variable offset impact on the inter-layer adhesion of a gradient scaffold should be conducted.

From Zhang et al.[78] A numerical investigation of the influence of process conditions on the temperature variation with respect to space and time in FFF can provide immediate guidance over current application of FFF. Significant physical phenomena such as bond formation and mechanical deformation could also be studied from the perspective of energy balance on the basis of this numerical model, especially when direct temperature measurement is challenging. More profoundly, understand temperature variation is beneficial and fundamental to the full understanding of the mechanics of FFF.

6.4 Conclusion

The effects of the extrusion temperature, the printing speed, the layer height and the offset distance on the contact area have been studied. In chapter 4, the importance of the contact area was established. A higher contact area between the filaments will results in a higher stiffness. Tuning this parameter to obtain the desired mechanical properties is crucial.

The comparison between the contact area of the previous layer and the newly deposited layer did not show a significant difference in the control condition, 0.0477 mm^2 and 0.0503 mm^2 less than 5%. Therefore, knowing which filament was deposited first was considered negligible. The filaments within a layer were considered equivalent. A variation in the extruder temperature while remaining above the fusion temperature of PLA did not have a significant impact on the contact area when below the control temperature, as seen before. Increasing the temperature above the control condition only resulted in a significantly smaller contact area. A difference in the appearance of the filament was noticed at 190°C, with a rougher surface and an overall more brittle structure. To conclude, it is not necessary to change the extruder temperature to improve the contact between the filaments and enhance the mechanical properties of the scaffold.

An increase by 300% of the contact area for a decrease of 43% of the layer height was observed. This translated into scaffolds with a higher Young's modulus, close to the uniform aligned scaffolds with a spacing of 0.85 mm, and in a slight decrease in porosity, similar to the uniform aligned scaffolds with a spacing of 1.2 mm. Decreasing the layer height is therefore a promising way to increase the stiffness of a scaffold with a small sacrifice over the porosity.

Using a higher printing speed resulted in an increase of the contact area. As described in the literature, the cooling time is reduced. Therefore, the new filament is deposited on a warmer layer improving the coalescence between the filaments, from 0.0477 mm^2 to 0.0746 mm^2.

When the filaments are not printed on top of each other, when an offset is introduced, like in the uniform offset scaffolds or the gradient scaffolds, the newly deposited filament will have less support from the previous layer resulting in smaller contact areas, from 0.0477 mm^2 to 0.0384 mm^2.

This work demonstrates the importance of the contact area and the relative importance of the printing parameters. A fine tuning of the mechanical properties of bone tissue engineered scaffolds is possible and more complex than simply choosing a filament diameter and a spacing. Further work is required to get a more complete understanding of the mechanics of lattice bone tissue engineered scaffolds.

Chapter 7 Conclusions and Future Work

7.1 Conclusion

The main goal of this study is to investigate the mechanical behaviour of Fused Filament Fabricated scaffolds for bone tissue engineering.

- The apparent elastic properties of 3D printed uniform aligned, uniform offset and gradient scaffolds were studied.
- A methodology to print bespoke lattice structures using FFF was implemented.
- The methodology was used to produce FFF parts with controlled structural parameters. The mechanical properties can be modified according to the diameter of the filament, the spacing of the filaments, the layer height, the implementation of an offset and the printing speed.
- Several samples, with the architectures mentioned above, were printed for mechanical compression using this methodology.
- The structure-property relationship of woodpile lattices was studied with analytical models and experimental characterization.
- A variable offset model in combination with an iso-stress rule of mixture was used to predict the Young's modulus of the gradient scaffolds.
- For a low porosity the analytical models were not in good agreement with the experimental results. The differences with the experimental data are attributed to the overlooked impact of the contact area on the contact area between the filaments. This omission resulted in lower Young's moduli for low porosity scaffolds. Even though the models are not yet able to capture the complexity of this architecture, two significant parameters were isolated.
- The first one is the porosity of the scaffold; it depends on the diameter, the layer height and the spacing.
- The second one is the contact area between the filaments; it is related to the diameter, the layer height, the presence of an offset between the filaments and the printing parameters. The rules of mixture applied to the micromechanical model gave information on the local mechanical behaviour of the scaffolds. Gradient scaffolds can be used to generate a strain gradient on cells and influence their differentiation.

The printing parameters were studied in regard of their influence on the contact area. The layer height and the printing speed have a significant impact on the mechanical response of the scaffolds. They both increased the contact area between the filaments. The contact area should

be included in analytical models when studying lattices as it has a significant impact on the mechanical response.

7.2 Future work

7.2.1 Modelling

The Rule Of Mixture used with the model developed by Norato et al. for uniform aligned scaffolds and the model used by Cuan Urqizo et al. for uniform offset scaffolds has limits that were discussed previously. It is important to use a model that captures a wider range of offsets as gradient scaffolds are mainly composed of offset filaments. The variable offset model described by Cuan Urquizo et al should be able to capture this specifity of the gradient scaffolds. It will therefore be possible to use a rule of mixture and obtain more accurate predictions for the gradient scaffolds.

It will also be interesting to explore the local behaviour of the gradient scaffolds with the help of the model and with mechanical testing. The local mechanical behaviour of gradient scaffolds should be explored with point tracking or Digital Image Correlation. These measurements will help test the validity of the iso-stress rule of mixture, the strain should vary locally. The local strain should be higher within a layer with more offset.

The printing parameters and their influence on the mechanical properties of FFF scaffolds was once again highlighted. The layer height induced an important change in the stiffness of the scaffolds. Therefore, it will be interesting to study the impact of the filament diameter, as it was shown in the literature to play an important role in the mechanical properties of the scaffolds. Another parameter that is worth considering is the overall temperature of the scaffold. Increasing the printing speed increased the contact area, as it reduced the cooling time, showing that the temperature of the layer on which the filament is deposited is important. Three parameters will be explored, the temperature of the heat-bed, the temperature of the environment during the print and the height of the print.

During this study, the contact area was directly linked to the mechanical properties of FFF scaffolds. It will be interesting to explore the structure of the lattices with micro-computed

tomography to study the morphology of the interlayer adhesion and the overall porosity. It will be possible to measure the cross-sections of contact areas without damaging them.

7.2.2 Biological evaluation

As it was shown in the previous study, gradient scaffolds present local mechanical behaviour. Experiments with cells should be conducted to observe the impact of the gradient scaffold on their behaviour. The first step will be to observe how efficient is the cell seeding in scaffolds like Di Luca's ones[4]. The viability, proliferation and differentiation of the cells should be studied without any external stimulation. Depending on the observations different gradients could be printed.

A bioreactor should be designed to apply a cyclic mechanical stimulus to a seeded gradient scaffold and observe the impact of the stimulation on the cell differentiation. According to Palomares et al.[37], a small cyclic bending motion, on a period of 4 weeks, favours chondrogenesis. The investigation of the cellular fate, according to the scaffold regions, is an exciting path to follow.

Appendix A 3D printing with MATLAB

MATLAB GCODE GUIDE

3D printing with MATLAB

The following code allows to:

- Control the path of the extruder with precise coordinates
    - Control the printing pattern
    - Control the angle of deposition (raster angle)
    - Control the shape, up to a single line
    - Control the spacing between the filaments
    - Control the layer height
- Control the fan
- Control the extrusion, amount of material and speed
- Control the printing speed
- Control the temperature of the nozzle and heat-bed
- Create scaffolds with different porosity regions
- Predict the properties of the material (work in progress)
    - Mass, volume and density
    - Mechanical

Author: Maria Stagno-Navarra

A.1 Introduction

This is the code to create a 3D shape i.e. multiple specified layers

The version of MATLAB required to run the code is R2018a and the mapping

toolbox add on is required as well as the standard ones from the intial MATLAB download.

Requirements:

MATLAB R2018a min.

Mapping Toolbox add on.

A.2 Main Code

```
fid = fopen('filename’,'w');
```

GCode file that gets created with the specified name.

Insert name of file instead of filename. Make sure to keep the inverted commas and the extension as .gcode.

The next section initialises the file and ends it once the process is done.

This section of code intialises the file and ends it once done

```
Mkey = ["M104", "M107", "M109", "M115 U3.2.1", "M140", "M190", "M201 X1000
Y1000 Z1000 E5000", "M203 X200 Y200 Z12 E120", "M204", "M205 S0 T0", "M205
X8 Y8 Z0.4 E1.5", "M221 S95", "M83", "M900 K30"];
```

This is an Array of all the M code to be used. Note that the version of the firmware would have to be updated as new versions are released. To do so, change **"M115 U3.2.1"** to reflect the most up to date software. You can add M codes if necessary to control other printer parameters. You can find a summary of all the M-codes and G-codes at: https://reprap.org/wiki/G-code

```
Mdef = [" ; Sets extruder temp in degrees Celsius", " ; Turns fan off",
" ;  Waiting for extruder to heat up", "; Get latest firmware version",
" ; Sets bed temp in degrees Celsius", " ;  Waiting for bed to heat up",
" ; Sets max accelerations in mm/sec^2", " ; Sets max feed rates in mm/sec",
" ; Sets max acceleration and retraction acceleration", " ; Sets min
extruding and travel feed rate", " ; Sets jerk limits in mm/sec", " ; Sets
```

```
extruder override percentage", " ; Sets extruder to relative mode", " ;
Sets linear advance factor. Filament GCode"];
```

This array defines the M codes specified above, in the previous array.

```
Gkey = ["G1", "G1 X100 E12.5 F1000", "G1 X113 Y105", "G1 X60 E9 F1000",
"G1 Y-3 F1000", "G21", "G28 W", "G80", "G90", "G91", "G92", "G92 E0"];
```

This is the array of all the G codes to be used.

```
Gdef = [" ; Linear Movement", " ; Initial thicker line to clear extruder",
" ; Move extruder to middle of the bed", " ; Initial thinner line to clear
extruder", " ; Extruder goes outside the print area", " ; Sets units to
mm", " ; Homes all axis (W=without mesh bed level)", " ; Mesh bed
levelling", " ; Sets coordinates such that they are defined from the origin
of the bed", " ; Sets coordinates such that they are defined relative to
each other", " ; Resets axis position to 0", ";Resets extruder position to
0"];
```

This is the array of the definitions of the corresponding G code in the previous array.

```
Initial_Sequence = [Mkey(2);' '; Mdef(2); Mkey(4);' '; Mdef(4);
```

This is the initial sequence for Prusa i3 Mk3 printer. Without this sequence the printer will display an error message saying that the file is corrupted otherwise.

```
    Mkey(7);' '; Mdef(7); Mkey(8);' '; Mdef(8);
    Mkey(9);' P1250 R1250 T1250' ; Mdef(9); Mkey(11);' '; Mdef(11);
    Mkey(10);' '; Mdef(10); Mkey(13);' '; Mdef(13);
    Mkey(1); ' S210'; Mdef(1); Mkey(5); ' S75'; Mdef(5);
```

```
    Mkey(6); ' S75'; Mdef(6); Mkey(3); ' S210'; Mdef(3);

    Gkey(7);' '; Gdef(7); Gkey(8);' '; Gdef(8);

    Gkey(5);' '; Gdef(5); Gkey(12);' '; Gdef(12);

    Gkey(4);' '; Gdef(4); Gkey(2);' '; Gdef(2);

    Gkey(12);' '; Gdef(12); Mkey(12);' '; Mdef(12);

    Mkey(14);' '; Mdef(14); Gkey(6);' '; Gdef(6);

    Gkey(9);' '; Gdef(9); ';Before layer change';' ';' ';

    Gkey(12);' '; Gdef(12); Gkey(1); ' E-0.8 F2100'; Gdef(1);

    Gkey(1); ' Z0.6 F10800'; Gdef(1); ';After layer change';' ';' ';

    Gkey(3);' '; Gdef(3); Gkey(1); ' Z0.2'; Gdef(1);

    Gkey(1); ' E0.8 F2100'; Gdef(1); Mkey(9); ' S800'; Mdef(9);

    Gkey(1); ' F1500'; Gdef(1);Gkey(9);' '; Gdef(9);

    ];


fprintf(fid,'%1s %6s %12s \r\n',Initial_Sequence);
```

This sequence prints the initial sequence of the GCode to the file needed for the printer to run.

Below you will find the variables that need to be defined/changed. These are constants throughout the print. Should you wish to change them during the print, comment out the variable in this section and specify it in each function in a section below which has a while loop for running the code.

```
bed_x = 210;
```

Width of the bed/heating plate

```
bed_y = 210;
```

Depth of the bed/heating plate

```
w = 25;
```

Width of the shape

```
d = 25;
```

Depth of the shape

```
h = 25;
```

Height of the shape

The file 'cube pic.JPG' gives a visual representation of what the dimensions represent.

```
layerheight = 0.35 ;
```

Layer height, note that 0.15 is the optimum layer height

```
%gap = 2.5;
```

```
Gap between the pathlines
```

```
nozzle_d = 0.4;
```

Nozzle diameter

```
n_regions = 1;
```

```
This is the number of seperate regions on top of each other (lateral
seperation)in case you need to print different regions with different
spacings for example.
```

```
material = "PLA";
```

The material which the print is going to be made from. This input is needed for the material and mechanical properties.

```
samplename = '210C';
```

The name you wish to give to your sample. It is printed at the top of the properties file.

Below you will find the variables that should be changed as wished for each layer. The variable should be specified for each function in a section below which has a while loop for running the code.

The variables should preferably not be defined at the beginning like those

above unless they are not changed. The variables are commented out and if

they don't change throughout the print, then the '%' can be removed to

define the variable for the whole print.

```
offset_x = 0; %Offset of the layer in the x direction
```

```
offset_y = 0; %Offset of the layer in the y direction
```

```
em = 0.57759;
```

The extruder multiplier which is used in the formula below to calculate the extruder factor. It can be changed to alter the roadwidth. Its currently set to 0.36mm.

```
e                =                ((nozzle_d*layerheight*em)+(((3.14159265-
4)*(layerheight*layerheight))/4));
```

The extruder factor which can be changed to change the roadwidth.

```
%e = 0.0544913; % for a layer height of 0.35
```

```
angle = 45;
```

This is the angle at which you want the pathlines to be. They are taken from the horizontal as shown in the picture with the filename 'angle_pic.jpg'.

Note: that for the obtuse function the angle cannot be equal to 0 or 180

degrees.

For the acute function, the angle must be between 1 and 90 degrees.

The zero function only works for zero degrees so required no angle input .

```
%%
```

These are the global variables. They should not be changed for any reason.

```
global totale;
```

%This Variable cumulatively calculates the total extruder movement

```
totale = 0;
```

```
global lh;
```

This variable cumulatively calculates the total layer height at each point

```
lh = layerheight;
```

```
global move;
```

This variable cumulatively calculates the movement of the extruder head

```
move = 0;
```

%%

These Variables help the print run properly and shouldn't be changed.

```
i = 1;
```

This is a counting variable needed for calculating the road width

```
e_vals = zeros(1);
```

This is an empty array for getting the average e factor value

```
layer = 0;
```

```
on off variable which turns on the fan and lowers the temperature of the nozzle by 5 degrees, when on.
```

```
s = 1;
```

This variable is used in creating discrete regions of scaffold.

```
%%
```

The functions in the next section are to be run for different angles.

The function you run depends on the angles as described in a previous

section. Just copy and paste the line which contains the function you wish to run and remove the '%' from the beginning of the line.

```
%onelayer_acute(bed_x,bed_y,w,d,gap,angle,offset_x,offset_y,fid,e,layerheight);
```

For 1 to 90 degrees.

```
%onelayer_obtuse(bed_x,bed_y,w,d,gap,angle,offset_x,offset_y,fid,e,layerheight);
```

%For 91 to 179 degrees

```
%onelayer_zero(bed_x,bed_y,w,d,gap,offset_x,offset_y,fid,e,layerheight);
```

%For 0 degree

%%

Producing GCode for the first region of the shape.

If regions > 1, then copy and paste the while loop underneath. This while

Loop will repeat for the number regions specified. This will allow regions

of varying properties to be produced. Note that the pasted while loop must

be before the line which calculates the average e value (e = ...)

%%%First region

```
while lh < ((h/n_regions)*s)
```

%This ensures that the loop continues till the required height is reached

%Here should be the first layer which you want to run. The layer functions

are in the section above. The as yet unchanged variables should be

changed/defined now.

```
      onelayer_zero_speed(bed_x,bed_y,w,d,1.45,0,0,fid,e,layerheight);
```

%for 0 degrees

```
      onelayer_zero_speed(bed_x,bed_y,w,d,1.45,67,0,fid,e,layerheight);
%for 0 degrees


      onelayer_zero_speed(bed_x,bed_y,w,d,1.45,0,-
67,fid,e,layerheight); %for 0 degrees


%     onelayer_zero(bed_x,bed_y,w,d,0.55,67,-30,fid,e); %for 0 degrees
%     onelayer_zero(bed_x,bed_y,w,d,0.85,17,0,fid,e); %for 0 degrees
%     onelayer_zero(bed_x,bed_y,w,d,0.85,67,0,fid,e); %for 0 degrees
%     onelayer_zero(bed_x,bed_y,w,d,1.2,17,0,fid,e); %for 0 degrees
%     onelayer_zero(bed_x,bed_y,w,d,1.2,67,0,fid,e); %for 0 degrees
%     onelayer_zero(bed_x,bed_y,w,d,3.5,17,70,fid,e); %for 0 degrees
%     onelayer_zero(bed_x,bed_y,w,d,3.5,67,70,fid,e); %for 0 degrees


    nextlayer(fid,layerheight);
```

The next layer function moves the printing level up be a specified amount.

```
e_vals(i) = e;
```

Adding the e value to the array

```
i = i + 1;
```

Adding to the counting variable

```
%%% This is to turn on the fan and drop the temperature by 5 degrees,
```

%%% this helps with PLA prints.

```
    layer = layer + 1;
```

%Turning the fan on

```
    if layer == 1
```

Once the first layer has been completed, the fan will turn on and the temperature will drop by 5 degrees. This temperature drop needs to be changed manually.

```
        Change = [Mkey(1);'S210';Mdef(1); 'M106';' 255';'; Fan on full
power ';];
```

Only the first layer is printed without the fan on

```
        fprintf(fid,'%1s %6s %12s \r\n',Change);
    end
```

```
onelayer_acute_speed(bed_x,bed_y,w,d,1.45,90,0,0,fid,e,layerheight);
```

for 1 to 90 degrees

```
onelayer_acute_speed(bed_x,bed_y,w,d,1.45,90,67,0,fid,e,layerheight); %fo
r
```

```
1 to 90 degrees


onelayer_acute_speed(bed_x,bed_y,w,d,1.45,90,0,-
67,fid,e,layerheight); %for


1 to 90 degrees




%      onelayer_acute(bed_x,bed_y,w,d,0.55,90,67,-30,fid,e); %for 1 to 90
degrees

%       onelayer_acute(bed_x,bed_y,w,d,0.85,90,17,0,fid,e); %for 1 to 90
degrees

%       onelayer_acute(bed_x,bed_y,w,d,0.85,90,67,0,fid,e); %for 1 to 90
degrees

%       onelayer_acute(bed_x,bed_y,w,d,1.2,90,17,0,fid,e); %for 1 to 90
degrees

%       onelayer_acute(bed_x,bed_y,w,d,1.2,90,67,0,fid,e); %for 1 to 90
degrees

%       onelayer_acute(bed_x,bed_y,w,d,3.5,90,17,70,fid,e); %for 1 to 90
degrees

%       onelayer_acute(bed_x,bed_y,w,d,3.5,90,67,70,fid,e); %for 1 to 90
degrees



    nextlayer(fid,layerheight);
```

The next layer function moves the printing level up be a specified amount.

```
    e_vals(i) = e;
```

```
Adding the e value to the array


    i = i + 1;
```

Adding to the counting variable

After the i = i + 1 line/next layer function, another layer can be added. Then another

'nextlayer' function along with the e_vals and i increase lines should be run,

repeat this step till you have the sequence of layers that you want.

The last functions should be the 'nextlayer' function followed by the

e_vals and i increase lines and finally the layer increase line.

```
end


s = s + 1;
```

This is an important line especially if you're making discrete regions. Make sure to always include after the end statement

```
e = mean(e_vals);
```

This is the mean of e factor values matrix, used in calculting road width.

Preview of the print in a web browser.

Note: To run the code faster, comment out the next line.

```
%web('http://nraynaud.github.io/webgcode/','-new','-notoolbar');   %Opens
the webpage in the MATLAB webpage

%browser. This is to visualise the GCode you have just produced.

%Copy and paste the GCode produced by opening the file you created and
copying all the text.

%Select all the GCode in the open webpage and delete it.

%Past your GCode there instead and click simulate. This will show the
toolpath of the 3D printer.

%To visualise your scaffold better in 3D, open the GCodeSimulatorV134.jar

%file, and load your GCode file.
```

The final sequence of code allows the Prusa i3 Mk3 to run without errors

```
Final_Sequence =   [Mkey(2);' ';Mdef(2);Mkey(1);' S0';Mdef(1);
```

Finishing sequence for Prusa i3 Mk3. Without it will say file is corrupted.

```
    Mkey(5);' S0';Mdef(5);

    ' ';' ';' I have finished printing, please take object';

    Gkey(10);' '; Gdef(10); Gkey(12);' '; Gdef(12);

    Gkey(1);' E-0.8'; Gdef(1); Gkey(1);' Z50'; Gdef(1);

    Gkey(1);' X-113 Y105' ; Gdef(1); Mkey(2);' '; Mdef(2);

    'M84';' ';' ;Stops idle hold';

    ];


fprintf(fid,'%1s %6s %12s \r\n',Final_Sequence);

fclose(fid);
```

The code is also creating a second file which contains all the predicted information. This information is only a prediction and should be verified depending on your material properties.

```
fig = fopen('DiLuca-aligned-spacing-1.45.txt','w'); %Opening of new file
with information needed for material property and time prediction.

%Insert name of file instead of filename. Make sure to keep the inverted
commas and the extension as .txt.
```

Introductory information

```
Intro = ["PROPERTIES FILE FOR";samplename;

        "";"";

        "BASIC INFORMATION USED IN LATER CALCULATION";"";];

fprintf(fig, '%1s %6s \r\n',Intro);
```

Prediction of the material used for the print

```
te1 = 6285.6520900122;

te2 = 1338.22819000007;

te3 = 1554.62879999994;

f_in_m = (((6.67/te1)+(1.46/te2)+(1.77/te3))/3) * totale * 0.89; % Length
of filament used. Used in material properties calculations.
```

```
f_in_mm3 = (((15732.83/te1)+(3520.42/te2)+(4253.08/te3))/3) * totale * 0.89; % Volume of filament used. Used in material properties calculations.

Prediction_information = [ % prints the values needed to input in the material properties function.

                          "Total Extruder Movement = ";totale; " - The movement of the extruder not the extruder head";

                          "Filament used in metres";f_in_m; " - An empirical calculation based on values extracted from Slic3r";

                          "Filament used in mm^3";f_in_mm3; " - An empirical calculation based on values extracted from Slic3r";];

fprintf(fig, '%1s %6s %6s \r\n',Prediction_information);
```

Time estimation of the print

```
ts = (1.184963138 * (move*0.03135))+240; %Calculation of time estimate in seconds.

tm = ts/60; %Calculation of time estimate in minutes.

th = tm/60; %Calculation of time estimate in hours.

Time = [' ';' ';

        "TIME ESTIMATIONS";"";

        "Time to complete part is:";" "; ts; "seconds"; tm;"minutes";th;"hours";];

fprintf(fig, '%1s %6s \r\n',Time);


================================================================================
================================================================================
====

%%

%Material property prediction.
```

```
%m1 = mass calculated using metres of filament, m2 = mass calculated using

%volume of filament used, d1 = density calculated using m1, d2 = density

%calculated using m2, p1 = porosity calculated using metres of filament

%p2 = porosity calculated using volume of filament,

% m3, m4, d3, d4 are values but not in SI units.

%material = type of material used, length = length of filament used in m

%volume = volume of filament used in mm^3


f_in_m = f_in_m * 0.86; %Value multiplied by factor to get more accurate
prediction

f_in_mm3 = f_in_mm3 * 0.86; %Value multiplied by factor to get more accurate
prediction


density = [1.24,1.1,1.19,1.3,1.15,1.2]; %in g/cm^3. Densities of the
various materials to be used.

r = 0.875; %radius of filament in mm. Would need to be changed if using
different machine

ov = (w*d*h)/(1000^3); %object volume in m^3. Volume of 25 x 25 x 25 cube,
the cubes produced for testing.

mvol = (f_in_mm3/1e9); %volume of filament used in SI units.

if material == "PLA" %#ok<*BDSCA> %Material specified in the function has
corresponding density stored in the workspace for later calculations.

    rho = density(1)*1000; %Density in SI units.

elseif material == "PCL" %Material specified in the function has
corresponding density stored in the workspace for later calculations.

    rho = density(2) * 1000; %Density in SI units.

elseif material == "PVA" %Material specified in the function has
corresponding density stored in the workspace for later calculations.

    rho = density(3) * 1000; %Density in SI units.
```

```
elseif material == "Conductive_TPU" %Material specified in the function has corresponding density stored in the workspace for later calculations.

    rho = density(4) * 1000; %Density in SI units.

elseif material == "Conductive_PLA" %Material specified in the function has corresponding density stored in the workspace for later calculations.

    rho = density(5) * 1000; %Density in SI units.

elseif material == "NinjaFlex" %Material specified in the function has corresponding density stored in the workspace for later calculations.

    rho = density(6) * 1000; %Density in SI units.

end

vol = pi * (r/1000)^2 * f_in_m; %volume of material used given length in m^3

m1 = vol * rho; %Calculation of mass as described above in kg.

m2 = (mvol) * rho; %Calculation of mass as described above.

m3= m1 * 1000; %mass m1 but in grams.

m4 = m2 *1000; %mass m2 but in grams.

d1 = m1/ov; %Calculation of density as described above.

d2 = m2/ov; %Calculation of density as described above.

d3 = d1 / 1000; %density d1 but g/cm^3.

d4 = d2 / 1000; %density d2 but g/cm^3.

p1 = (1-(vol/ov))*100; %Calculation of porosity as described above.

p2 = (1-(mvol/ov))*100; %Calculation of porosity as described above.

p4 = (1 - (d1/rho))*100; %Porosity calculated using 1 - relative density

p5 = (1 - (d2/rho))*100; %Porosity calculated using 1 - relative density

p6 = ((ceil(p4))+(ceil(p5)))/2; %Porosity as average of 1 - relative density. Closest value to actual porosity

m5 = ((1-(p6/100))*1.24*(2.5^3))*1.1722103; %Mass of the scaffold based on porosity

if p6 < 80
```

```
    multiplier = 0.927795016;

else

    multiplier = 0.969101103;

end

p7 = floor(p6*multiplier);



info = ['';'';'';"GENERIC PROPERTIES OF THE SCAFFOLD";"";"";

        samplename;"has dimensions 25 x 25 x 25";" mm"; %Prints the basic
information of the samples. This is based upon a 25 x 25 x 25 cube with
the road with to be the nozzle diameter plus layer height.

        "Spacing is ";'variable'; "mm";

        "Average road width is "; (e*7.172639148)+0.0920261415; " mm";

        "Listed below are its predicted properties";" ";" ";

        " ";" ";" ";];

data = ["CALCULATED MASS, DENSITY AND POROSITY FOR SCAFFOLD USING DIFFERENT
METHODS";"";"";"";

        "Mass calculated using metres of filament";m1;"kg";""; %Prints the
values calculated above to make it easier to get and read the information
for the samples given length of filament used and volume of filament used.

        "Mass calculated using volume of filament";m2;"kg";"";

        "Mass calculated using metres of filament";m3;"g";"";

        "Mass calculated using volume of filament";m4;"g";"";

        "Density calculated using first mass";d1;"kg/m^3";"";

        "Density calculated using second mass";d2;"kg/m^3";"";

        "Density calculated using first mass";d3;"g/cm^3";"";

        "Density calculated using second mass";d4;"g/cm^3";"";

        "Porosity calculated using metres of filament";p1;"%";"";

        "Porosity calculated using volume of filament";p2;"%";"";

        "Porosity calculated using 1 - relative density 1 is ";p4;"%";"";
```

```
        "Porosity calculated using 1 - relative density 2 is ";p5;"%";"";

        "";"";"";"";

        "THE POROSITY OF THE SCAFFOLD IS";p7;"%";" - calculated using
empirical correction found from experimental data";

        "THE MASS OF THE SCAFFOLD BASED ON POROSITY ABOVE IS";m5;"g";" -
calculated using empirical correction found from experimental data";

        "";"";"";"";

        "From experimentation it was found that the actual values of
porosity were higher than predicted";"";"";"";

        "";"";"";"";];


fprintf(fig, '%1s %6s %2s \r\n',info);

fprintf(fig, '%1s %6s %1s %2s \r\n',data);


%%

%Mechanical property prediction


Youngs_Modulus = [3120,470,3860,12,"N/A",12]; %Youngs modulus of the
materials in MPa

densities = [1.24,1.1,1.19,1.3,1.15,1.2]; %in g/cm^3. Densities of the
various materials to be used.

yield_stress = [70,25.2,"N/A",15,"N/A",4]; %Tensile yield stress in MPa

fracture_stress = [73,"N/A",78,15,"N/A",26]; %UTS in MPa

c1 = 1; c2 = 0.05; c3 = 0.3; c4 = 0.2; c5 = 3/8;

if material == "PLA" %Material specified in the function has corresponding
density stored in the workspace for later calculations.

    i = 1;

    E = str2num(Youngs_Modulus(i)); %#ok<*ST2NM> %Youngs in SI units.

    rho = densities(i); %Density in g/cm^3
```

```
    YS = str2num(yield_stress(i)); %yield stress in MPa

    FS = str2num(fracture_stress(i)); %fracture stress/force at break in
MPa

elseif material == "PCL" %Material specified in the function has
corresponding density stored in the workspace for later calculations.

    i = 2;

    E = str2num(Youngs_Modulus(i)); %Youngs in SI units.

    rho = densities(i); %Density in g/cm^3

    YS = str2num(yield_stress(i)); %yield stress in MPa

    FS = str2num(fracture_stress(i)); %fracture stress/force at break in
MPa

elseif material == "PVA" %Material specified in the function has
corresponding density stored in the workspace for later calculations.

    i = 3;

    E = str2num(Youngs_Modulus(i)); %Youngs in SI units.

    rho = densities(i); %Density in g/cm^3

    YS = str2num(yield_stress(i)); %yield stress in MPa

    FS = str2num(fracture_stress(i)); %fracture stress/force at break in
MPa

elseif material == "Conductive_TPU" %Material specified in the function
has corresponding density stored in the workspace for later calculations.

    i = 4;

    E = str2num(Youngs_Modulus(i)); %Youngs in SI units.

    rho = densities(i); %Density in g/cm^3

    YS = str2num(yield_stress(i)); %yield stress in MPa

    FS = str2num(fracture_stress(i)); %fracture stress/force at break in
MPa

elseif material == "Conductive_PLA" %Material specified in the function
has corresponding density stored in the workspace for later calculations.

    i = 5;
```

```
    E = str2num(Youngs_Modulus(i)); %Youngs in SI units.

    rho = densities(i); %Density in g/cm^3

    YS = str2num(yield_stress(i)); %yield stress in MPa

    FS = str2num(fracture_stress(i)); %fracture stress/force at break in
MPa

elseif material == "NinjaFlex" %Material specified in the function has
corresponding density stored in the workspace for later calculations.

    i = 6;

    E = str2num(Youngs_Modulus(i)); %Youngs in SI units.

    rho = densities(i); %Density in g/cm^3

    YS = str2num(yield_stress(i)); %yield stress in MPa

    FS = str2num(fracture_stress(i)); %fracture stress/force at break in
MPa

end


relative_density1 = d3/rho; %Relative density of scaffold

YM_1 = E * (relative_density1)^2 * c1; %Youngs modulus of scaffold
calculated with first density value

El_1 = E * (relative_density1)^2 * c2; %

Pl_1 = YS * (relative_density1)^(3/2) * c3;

Cr_1 = FS * (relative_density1)^(3/2) * c4;

G_1 = E * (relative_density1)^2 * c5;

ED_1 = 1 - (1.4 * relative_density1);


relative_density2 = d4/rho; %Relative density of scaffold

YM_2 = E * (relative_density2)^2 * c1; %Youngs modulus of scaffold
calculated with second density value

El_2 = E * (relative_density2)^2 * c2;

Pl_2 = YS * (relative_density2)^(3/2) * c3;
```

```
Cr_2 = FS * (relative_density2)^(3/2) * c4;

G_2 = E * (relative_density2)^2 * c5;

ED_2 = 1 - (1.4 * relative_density2);


relative_density3 = (1-(p6/100)); %Relative density of scaffold

YM_3 = E * (relative_density3)^2 * c1; %Youngs modulus of scaffold
calculated with second density value

El_3 = E * (relative_density3)^2 * c2;

Pl_3 = YS * (relative_density3)^(3/2) * c3;

Cr_3 = FS * (relative_density3)^(3/2) * c4;

G_3 = E * (relative_density3)^2 * c5;

ED_3 = 1 - (1.4 * relative_density3);


YM_4 = (E * (relative_density3^5))*63.07419497278; %Young's Modulus
calculation based Ashby and Gibson's model

YM_5 = min([YM_3 YM_4]); %Takes mimimum of 2 young's modulus values


Mdata1 =["Properties based on density 1";" - calculated using the
relationships listed appendix II, figure 10 of the report";'';

        "Relative density of scaffold is "; relative_density1; "";

        "The predicted Youngs Modulus is "; YM_1; "MPa";

        "The predicted elastic collapse stress is ";El_1 ; "MPa";

        "The predicted plastic collapse stress is ";Pl_1 ; "MPa";

        "The predicted brittle crushing strength is ";Cr_1 ; "MPa";

        "The predicted shear modulus is ";G_1 ; "MPa";

        "The predicted densification strain is ";ED_1 ; "";

        " "; " "; " ";

        ];
```

```
Mdata2 =["Properties based on density 2";" - calculated using the
relationships listed appendix II, figure 10 of the report";'';

        "Relative density of scaffold is "; relative_density2; "";

        "The predicted Youngs Modulus is "; YM_2 ;"MPa";

        "The predicted elastic collapse stress is ";El_2 ; "MPa";

        "The predicted plastic collapse stress is ";Pl_2 ; "MPa";

        "The predicted brittle crushing strength is ";Cr_2 ; "MPa";

        "The predicted shear modulus is ";G_2 ; "MPa";

        "The predicted densification strain is ";ED_2 ; "";

        " "; " "; " ";

        ];


Mdata3 =['';'';'';'';

        "THE MECHANICAL PROPERTIES OF THE SCAFFOLD ARE";" - most are
calculated using the relationships listed appendix II, figure 10 of the
report";

        '';'';

        "Relative density of scaffold is "; relative_density3; "";"";

        "The predicted Young's Modulus is "; YM_5 ;"MPa";" - Taken as the
lower value when the young's modulus is calculated using an adapted version
of Ashby and Gibson's relationship";

        "The predicted elastic collapse stress is ";El_3 ; "MPa";"";

        "The predicted plastic collapse stress is ";Pl_3 ; "MPa";"";

        "The predicted brittle crushing strength is ";Cr_3 ; "MPa";"";

        "The predicted shear modulus is ";G_3 ; "MPa";"";

        "The predicted densification strain is ";ED_3 ;"";"";

        "";"";"";"";

        ];
```

```
fprintf(fig,'%1s %6s %2s \r\n',Mdata1);

fprintf(fig,'%1s %6s %2s \r\n',Mdata2);

fprintf(fig,'%1s %6s %2s %6s \r\n',Mdata3);


fclose(fig); %Closing the prediction file.
```

A.3 Functions

Original concept developed by Hazel Mitchell

Plots GCode for rectangle or square shape

All units are in mm

Meaning of the input variables:

- bed_x = width of the bed/dimension in the x direction
- bed_y = depth of the bed/dimension in the y direction
- w = width of your part
- d = depth of your part See 'cube pic.jpg' for a better visualisation
- gap = gap between the printed lines
- angle = angle between the printed lines. See 'angle_pic.jpg' for a better visualisation
- offset_x = offset of the layer from the origin in the x direction
- offset_y = offset of the layer from the origin in the y direction
- fid = variable that opens/creates the file you request to write the gcode to
- e = e factor value which controls the thickness of the printed line
- layerheight = layer height, used to determine if the initial purging line is required at this height.

A.3.1 onelayer-acute

```
function                                    []                                    =
onelayer_acute(bed_x,bed_y,w,d,gap,angle,offset_x,offset_y,fid,e,layerhei
ght)
```

Derived values

```
F_speed = (e - 0.0920216)/(-0.000027156);
```

Drawing of the desired shape:

```
xlimit = [(((bed_x/2)-(w/2))) (((bed_x/2)+(w/2)))];
ylimit = [(((bed_y/2)-(d/2))) (((bed_y/2)+(d/2)))];
xbox = xlimit([1 1 2 2 1]);
ybox = ylimit([1 2 2 1 1]);
```

Visualisation of shape that you draw, remove the '%' to show it. It's a popup.

```
%mapshow(xbox,ybox,'DisplayType','polygon','LineStyle','none')
```

Visualisation of shape that you draw, remove the '%' to show it. It's a popup.

Finding the coordinates:

```
angle = deg2rad(angle);
a = min((floor((w*2)/gap)),(floor((d*2)/gap)));
x = zeros(1, a); %setting up the initial matrices
y = zeros(1, a);%setting up the initial matrices
```

```
i = 2;

for a = -bed_y/tan(angle):(gap/(sin(angle))):bed_x

    if angle == deg2rad(90)

        xm   =   ((((bed_x/2)-(w/2)))   -   (gap   *   ceil((((bed_x/2)-
(w/2)))/gap)))++0.01;

    else

        xm = 0;

    end

    x(i) = a+xm; %Start of line

    y(i) = 0; %Start of line

    i = i + 1;

    x(i) = a + bed_y/tan(angle)+xm; %End of line

    y(i) = bed_y; %End of line

    i = i + 1;

    x(i) = NaN; %Skips a line

    y(i) = NaN; %Skips a line

    i = i + 1;

end

% if (rem(w,gap)) == 0

%     %do nothing

% else

    x(i) = (((bed_x/2)+(w/2)));

    y(i) = (((bed_y/2)-(d/2)));

    i = i + 1;

    x(i) = (((bed_x/2)+(w/2)));

    y(i) = (((bed_y/2)+(d/2)));

% end
```

```
%mapshow(x,y,'Marker','+')

[xi,yi,ii] = polyxpoly(x,y,xbox,ybox);



xi(numel(xi)+1) = xlimit(2) ;

yi(numel(yi)+1) = ylimit(1) ;

%mapshow(xi,yi,'DisplayType','point','Marker','o')

ii = ii(:,1);

co_x = zeros(1, (numel(xi)+1)); %zeros matrix for unordered x coordinates

co_y = zeros(1, (numel(yi)+1)); %zeros matrix for unordered y coordinates

num = zeros(1, (numel(ii)+2));

co_x(1) = xlimit(1) + offset_x;

co_y(1) = ylimit(2) + offset_y;

num(1)  = (min(ii)-1);

for i = 2:(numel(xi))+1

    co_x(i) = xi((i-1)) + offset_x;

    co_y(i) = yi((i-1)) + offset_y;

    if i == (numel(xi))+1

        break;

    end

    num(i) = ii((i-1));

end

num(numel(num)) = ii((numel(ii)))+1;

co_x_order = zeros(1, (numel(xi)+1)); %zeros matrix for ordered matrix for
x coordinates

co_y_order = zeros(1, (numel(yi)+1)); %zeros matrix for ordered matrix for
y coordinates
```

```
[b,c] = sort(num,2); %#ok<ASGLU> %b is an array of the sorted values of
the num matrix, c is an array of the original indexing for the sorted
array. Tells us which order to have stuff in.

ygap = 0;

for i = 1:3

    co_x_order(i) = co_x((c(i)));

    co_y_order(i) = co_y((c(i)));

end

agap = (co_y_order(1) - co_y_order(2));

ygap = ygap + agap;

i = 4;

while (d - ygap) > gap

    co_x_order(i) = co_x((c(i+1)));

    co_y_order(i) = co_y((c(i+1))); % 4

    i = i + 1;

    if i == numel(c)

        break;

    end

    co_x_order(i) = co_x((c(i-1)));

    co_y_order(i) = co_y((c(i-1))); %5

    ygap = ygap + (co_y_order(i-3) - co_y_order(i));

    i = i + 1;

    if i == numel(c) || (d-ygap) < ((co_y_order(i-4) - co_y_order(i-1))*1)

        break;

    end

    co_x_order(i) = co_x((c(i)));

    co_y_order(i) = co_y((c(i))); %6

    ygap = ygap + (co_y_order(i-1) - co_y_order(i));
```

```
    i = i + 1;
    if i == numel(c)
        break;
    end
    co_x_order(i) = co_x((c(i)));
    co_y_order(i) = co_y((c(i))); %7
    i = i + 1;
    if i == numel(c) || (d-ygap) < ((co_y_order(i-3) - co_y_order(i-2))*1)
        break;
    end
end
if (co_y_order(i-2)) > (co_y_order(i-1)) && (i ~= numel(c))
    co_x_order(i) = co_x((c(i+1)));
    co_y_order(i) = co_y((c(i+1))); %1
    i = i + 1;
    co_x_order(i) = co_x((c(i-1)));
    co_y_order(i) = co_y((c(i-1))); %2
    i = i + 1;
end
for j = i:numel(c)-1
    co_x_order(i) = co_x((c(i)));
    co_y_order(i) = co_y((c(i))); %1
    i = i + 1;
    if i == numel(c)
        break;
    end
    co_x_order(i) = co_x((c(i)));
```

```
    co_y_order(i) = co_y((c(i))); %2
    i = i + 1;
    if i == numel(c)
        break;
    end
    co_x_order(i) = co_x((c(i+1)));
    co_y_order(i) = co_y((c(i+1))); %3
    i = i + 1;
    if i == numel(c)
        break;
    end
    co_x_order(i) = co_x((c(i-1)));
    co_y_order(i) = co_y((c(i-1))); %4
    i = i + 1;
    if i == numel(c)
        break;
    end
end
co_x_order(i) = co_x((c(i)));
co_y_order(i) = co_y((c(i)));
```

Extruder value calculation

New empty matrix for extruder movement coordinates

```
E_order = zeros(1, (numel(xi)));
```

```
for i = 2:numel(c)

    E_order(i-1)          =          e*(sqrt(((co_x_order(i)-co_x_order(i-
1))^2)+((co_y_order(i)-co_y_order(i-1))^2)));    %Adding    the    extruder
movement values to the matrix

    i = i + 1;

end
```

New empty matrix for extruder movement coordinates without excess movement.

```
E_order_revised = zeros (1, (numel(xi)));

for i = 2:numel(c)

    if rem(i-1,2) == 0

        E_order_revised(i-1) = E_order(i-1);

    else

        E_order_revised(i-1) = 0;

    end

end
```

Initial movement of the printer head

```
global totale; %Global variable defined in pattern function to calculate
the total movement of the extruder for material use and time calculation
in material properties function.

global lh; %Global variable defined in pattern function to determine the
actual layer height of the print. Used when moving in the Z direction.

global move; %Global variable defined in pattern function to determine the
movement of the extruder head.
```

```
Gkey = ["G1", "G1 X100 E12.5 F1000", "G1 X113 Y105", "G1 X60 E9 F1000",
"G1 Y-3 F1000", "G21", "G28 W", "G80", "G90", "G91", "G92", "G92 E0"]; %
Array of all the G codes to be used.

Gdef = [" ; Linear Movement", " ; Initial thicker line to clear extruder",
" ; Move extruder to middle of the bed", " ; Initial thinner line to clear
extruder", " ; Extruder goes outside the print area", " ; Sets units to
mm", " ; Homes all axis (W=without mesh bed level)", " ; Mesh bed
levelling", " ; Sets coordinates such that they are defined from the origin
of the bed", " ; Sets coordinates such that they are defined relative to
each other", " ; Resets axis position to 0", ";Resets extruder position to
0"]; % Array of the definitions of the corresponding G code in the previous
array.

Reset = [Gkey(1);' Z';lh + 0.6;' E';'-0.8';Gdef(1); Gkey(1);'
X';co_x_order(1);' Y';co_y_order(1);Gdef(1);Gkey(1);' Z';lh;'
E';'0.8';Gdef(1);Gkey(12);'';'';'';'';Gdef(12);Gkey(1);'
F';F_speed;'';'';Gdef(1);]; % Resets the position of the extruder head to
the starting point of the track it will take.

fprintf(fid,'%1s %6s %6s %6s %6s %12s \r\n',Reset); %Prints the extruder
position reset commands in the gcode script.



%%

%Actual movement

i = 2;

%Purging line

if lh == layerheight

    Purging = [Gkey(1);' X';co_x_order(2);' Y';co_y_order(2)-10;'
E';0;Gdef(1);

               Gkey(1);' X';co_x_order(2)+25;';co_y_order(2)-10;'
E';e*25;Gdef(1);

               Gkey(1);' X';co_x_order(1);' Y';co_y_order(1);'';'';'';];

    fprintf(fid,'%1s %6s %6s %6s %6s %6s %6s %12s \r\n',Purging);%Printing
the purging line

end
```

```
%Printing the scaffold

while i < (numel(c)+1)

    if i == 2

        Blob = [Gkey(1);' E-0.8';Gdef(1);];

        fprintf(fid,'%1s %6s %12s \r\n',Blob); %Printing the material blob
retraction

    end

    Actual_Print  =  [Gkey(1);'  X';co_x_order(i);'  Y';co_y_order(i);'
E';E_order_revised(i-1);Gdef(1);];

    fprintf(fid,'%1s    %6s    %6s    %6s    %6s    %6s    %6s    %12s
\r\n',Actual_Print); %printing line

    totale    =    totale    +    (e*(sqrt(((co_x_order(i)-co_x_order(i-
1))^2)+((co_y_order(i)-co_y_order(i-1))^2))));

    move     =     move     +     ((sqrt(((co_x_order(i)-co_x_order(i-
1))^2)+((co_y_order(i)-co_y_order(i-1))^2))));

    Reposition  =  [Gkey(1);'  Z';lh;Gkey(1);'  E0.8';'  F2100';Gkey(1);'
F';F_speed;' ;Reposition';];

    fprintf(fid,'%1s  %3s  %3s  %3s  %3s  %3s  %3s  %3s  %3s  %3s  %12s
\r\n',Reposition); %Printing reposition commands

    NP = [''];

    fprintf(fid,'%1s \r\n',NP); %New line

    i = i + 1;

    if i == (numel(c)+1)

        break

    end

    Actual_Print  =  [Gkey(1);'  X';co_x_order(i);'  Y';co_y_order(i);'
E';E_order_revised(i-1);Gdef(1);];

    fprintf(fid,'%1s    %6s    %6s    %6s    %6s    %6s    %6s    %12s
\r\n',Actual_Print); %printing line

    totale    =    totale    +    (e*(sqrt(((co_x_order(i)-co_x_order(i-
1))^2)+((co_y_order(i)-co_y_order(i-1))^2))));
```

```
    move      =      move      +      ((sqrt(((co_x_order(i)-co_x_order(i-
1))^2)+((co_y_order(i)-co_y_order(i-1))^2))));

    if co_y_order(i-1)>co_y_order(i)

        n_coord = co_y_order(i)-5;

    else

        n_coord = co_y_order(i)+5;

    end

    Retract = [Gkey(1);' F8640';' Y';n_coord;' E-0.76';Gkey(1);' E-0.04';'
F2100';Gkey(1);' Z';lh+0.6;' F10800';' ;Retract';];

    fprintf(fid,'%1s %3s %3s %3s %3s %3s %3s %3s %3s %3s %3s %3s %12s
\r\n',Retract); %Printing retraction commands

    i = i + 1;

end

assignin('base', 'totale', totale); %Returns the total movement of the
extruder to the main/base workspace.

assignin('base','move', move); %Returns the total movement of the extruder
head to the main/base workspace.

assignin('base', 'e', e); %Returns the e factor to the main/base workspace.
For calculating the road width.

%%

%resetting the extruder head

nozzle = [Gkey(1);' E';'-1.0';Gdef(1);Gkey(1);' E';'1.0';Gdef(1);];

fprintf(fid,'%1s %6s %6s %12s \r\n',nozzle); %Prints the resetting of the
extruded material.
```

A.3.2 onelayer-obtuse

```
function [] = onelayer_obtuse(bed_x,bed_y,w,d,gap,angle,offset_x,offset_y,fid,e,layerheight)
```

Original concept developed by Hazel Mitchell

Plots GCode for rectangle or square shape

All units are in mm

Meaning of the input variables:

- bed_x = width of the bed/dimension in the x direction
- bed_y = depth of the bed/dimension in the y direction
- w = width of your part
- d = depth of your part See 'cube pic.jpg' for a better visualisation
- gap = gap between the printed lines
- angle = angle between the printed lines. See 'angle_pic.jpg' for a better visualisation
- offset_x = offset of the layer from the origin in the x direction
- offset_y = offset of the layer from the origin in the y direction
- fid = variable that opens/creates the file you request to write the gcode to
- e = e factor value which controls the thickness of the printed line
- layerheight = layer height, used to determine if the initial purging line is required at this height.

Derived values

```
F_speed = (e - 0.0920216)/(-0.000027156);
```

Drawing the desired shape (here rectangle or square):

```
xlimit = [(((bed_x/2)-(w/2))) (((bed_x/2)+(w/2)))];

ylimit = [(((bed_y/2)-(d/2))) (((bed_y/2)+(d/2)))];

xbox = xlimit([1 1 2 2 1]);

ybox = ylimit([1 2 2 1 1]);

%mapshow(xbox,ybox,'DisplayType','polygon','LineStyle','none')
```

Finding the coordinates

```
angle = 180 - angle;

angle = deg2rad(angle);

a = min((floor((w*2)/gap)),(floor((d*2)/gap)));
```

Set up of the initial matrices for the coordinates:

```
x = zeros(1, a); %setting up the initial matrices

y = zeros(1, a);%setting up the initial matrices

i = 2;

for a = (bed_x+bed_y/tan(angle)):-(gap/(sin(angle))):0

    x(i) = a; %Start of line

    y(i) = 0; %Start of line

    i = i + 1;

    x(i) = a - bed_y/tan(angle); %End of line

    y(i) = bed_y; %End of line

    i = i + 1;

    x(i) = NaN; %Skips a line

    y(i) = NaN; %Skips a line

    i = i + 1;

end
```

To show the start and end points of the lines

```
%mapshow(x,y,'Marker','+')
```

To find the intersection of the lines and the box

```
[xi,yi,ii] = polyxpoly(x,y,xbox,ybox);
```

Final x and y coordinates

```
xi(numel(xi)+1) = xlimit(1) ;

yi(numel(yi)+1) = ylimit(1) ;

%mapshow(xi,yi,'DisplayType','point','Marker','o')

ii = ii(:,1);

co_x = zeros(1, (numel(xi)+1)); %zeros matrix for unordered x coordinates

co_y = zeros(1, (numel(yi)+1)); %zeros matrix for unordered y coordinates

num = zeros(1, (numel(ii)+2));

co_x(1) = xlimit(2) + offset_x; %initial x coordinate

co_y(1) = ylimit(2) + offset_y; %initial y coordinate

num(1)  = (min(ii)-1);

for i = 2:(numel(xi))+1

    co_x(i) = xi((i-1)) + offset_x;

    co_y(i) = yi((i-1)) + offset_y;

    if i == (numel(xi))+1

        break;

    end

    num(i) = ii((i-1));

end

num(numel(num)) = ii((numel(ii)))+1;

co_x_order = zeros(1, (numel(xi)+1));

%zeros matrix for ordered matrix for x coorindates

co_y_order = zeros(1, (numel(yi)+1));

%zeros matrix for ordered matrix for y coorindates
```

```
[b,c] = sort(num,2);
```

% %b is an array of the sorted values of the num matrix, c is an array of the original indexing for the sorted array. Tells us which order to have stuff in.

```
ygap = 0;
for i = 1:3
    co_x_order(i) = co_x((c(i)));
    co_y_order(i) = co_y((c(i)));
end
agap = (co_y_order(1) - co_y_order(2));
ygap = ygap + agap;
i = 4;
while (d - ygap) > gap
    co_x_order(i) = co_x((c(i+1)));
    co_y_order(i) = co_y((c(i+1))); %4
    i = i + 1;
    if i == numel(c)
        break;
    end
    co_x_order(i) = co_x((c(i-1)));
    co_y_order(i) = co_y((c(i-1))); %5
    ygap = ygap + (co_y_order(i-3) - co_y_order(i));
    i = i + 1;
    if i == numel(c) || (d-ygap) < ((co_y_order(i-4) - co_y_order(i-1))*1)
        break;
    end
    co_x_order(i) = co_x((c(i)));
```

```
    co_y_order(i) = co_y((c(i))); %6
    ygap = ygap + (co_y_order(i-1) - co_y_order(i));
    i = i + 1;
    if i == numel(c)
        break;
    end
    co_x_order(i) = co_x((c(i)));
    co_y_order(i) = co_y((c(i))); %7
    i = i + 1;
    if i == numel(c) || (d-ygap) < ((co_y_order(i-3) - co_y_order(i-2))*1)
        break;
    end
end
if (co_y_order(i-2)) > (co_y_order(i-1)) && (i ~= numel(c))
    co_x_order(i) = co_x((c(i+1)));
    co_y_order(i) = co_y((c(i+1))); %1
    i = i + 1;
    co_x_order(i) = co_x((c(i-1)));
    co_y_order(i) = co_y((c(i-1))); %2
    i = i + 1;
end
for j = i:numel(c)-1
    co_x_order(i) = co_x((c(i)));
    co_y_order(i) = co_y((c(i))); %1
    i = i + 1;
    if i == numel(c)
        break;
```

```
    end
    co_x_order(i) = co_x((c(i)));
    co_y_order(i) = co_y((c(i))); %2
    i = i + 1;
    if i == numel(c)
        break;
    end
    co_x_order(i) = co_x((c(i+1)));
    co_y_order(i) = co_y((c(i+1))); %3
    i = i + 1;
    if i == numel(c)
        break;
    end
    co_x_order(i) = co_x((c(i-1)));
    co_y_order(i) = co_y((c(i-1))); %4
    i = i + 1;
    if i == numel(c)
        break;
    end
end
co_x_order(i) = co_x((c(i)));
co_y_order(i) = co_y((c(i)));
```

Extruder value calculation:

Creation of a new empty matrix for extruder movement coordinates

```
E_order = zeros(1, (numel(xi)));

for i = 2:numel(c)

    E_order(i-1)          =          e*(sqrt(((co_x_order(i)-co_x_order(i-
1))^2)+((co_y_order(i)-co_y_order(i-1))^2)));
```

%Adding the extruder movement values to the matrix

```
    i = i + 1;

end

E_order_revised = zeros (1, (numel(xi)));
```

%new empty matrix for extruder movement coordinates without excess movement.

```
for i = 2:numel(c)

    if rem(i-1,2) == 0

        E_order_revised(i-1) = E_order(i-1);

    else

        E_order_revised(i-1) = 0;

    end

end



%%
```

Initial movement of the printer head

```
global totale;
```

%Global variable defined in pattern function to calculate the total movement of the extruder for material use and time calculation in material properties function.

```
global lh;
```

%Global variable defined in pattern function to determine the actual layer height of the print. Used when moving in the Z direction.

```
global move;
```

%Global variable defined in pattern function to determine the movement of the extruder head.

% Array of all the G codes to be used. G-keys are used for movement

```
Gkey = ["G1", "G1 X100 E12.5 F1000", "G1 X113 Y105", "G1 X60 E9 F1000",
"G1 Y-3 F1000", "G21", "G28 W", "G80", "G90", "G91", "G92", "G92 E0"];
```

.

% Array of the definitions of the corresponding G code in the previous array.

```
Gdef = [" ; Linear Movement", " ; Initial thicker line to clear extruder",
" ; Move extruder to middle of the bed", " ; Initial thinner line to clear
extruder", " ; Extruder goes outside the print area", " ; Sets units to
mm", " ; Homes all axis (W=without mesh bed level)", " ; Mesh bed
levelling", " ; Sets coordinates such that they are defined from the origin
of the bed", " ; Sets coordinates such that they are defined relative to
each other", " ; Resets axis position to 0", ";Resets extruder position to
0"];
```

% Resets the position of the extruder head to the starting point of the track it will take.

```
Reset = [Gkey(1);' Z';lh + 0.6;' E';'-0.8';Gdef(1); Gkey(1);'
X';co_x_order(1);' Y';co_y_order(1);Gdef(1);Gkey(1);' Z';lh;'
E';'0.8';Gdef(1);Gkey(12);'';'';'';'';Gdef(12);Gkey(1);'
F';F_speed;'';'';Gdef(1);];
```

%Prints the extruder position reset commands in the gcode script.

```
fprintf(fid,'%1s %6s %6s %6s %6s %12s \r\n',Reset);
```

```
%%
```

%Actual movement

```
i = 2;
```

```
%Purging line

if lh == layerheight

    Purging   =   [Gkey(1);'   X';co_x_order(2);'   Y';co_y_order(2)-10;'
E';0;Gdef(1);

               Gkey(1);'         X';co_x_order(2)+25;';co_y_order(2)-10;'
E';e*25;Gdef(1);

               Gkey(1);' X';co_x_order(1);' Y';co_y_order(1);'';'';'';];

    fprintf(fid,'%1s %6s %6s %6s %6s %6s %6s %12s \r\n',Purging);

%Printing the purging line

end


%Printing the scaffold


while i < (numel(c)+1)

    if i == 2

        Blob = [Gkey(1);' E-0.8';Gdef(1);];

        fprintf(fid,'%1s %6s %12s \r\n',Blob);

%Printing the material blob retraction

    end

    Actual_Print   =   [Gkey(1);'   X';co_x_order(i);'   Y';co_y_order(i);'
E';E_order_revised(i-1);Gdef(1);];

    fprintf(fid,'%1s     %6s     %6s     %6s     %6s     %6s     %6s     %12s
\r\n',Actual_Print); %printing line

    totale     =     totale     +     (e*(sqrt(((co_x_order(i)-co_x_order(i-
1))^2)+((co_y_order(i)-co_y_order(i-1))^2))));

    move      =      move      +      ((sqrt(((co_x_order(i)-co_x_order(i-
1))^2)+((co_y_order(i)-co_y_order(i-1))^2))));

    Reposition   =   [Gkey(1);'   Z';lh;Gkey(1);'   E0.8';'   F2100';Gkey(1);'
F';F_speed;' ;Reposition';];
```

```
    fprintf(fid,'%1s  %3s  %3s  %3s  %3s  %3s  %3s  %3s  %3s  %3s  %12s
\r\n',Reposition); %Printing reposition commands

    NP = [''];];

    fprintf(fid,'%1s \r\n',NP); %New line

    i = i + 1;

    if i == (numel(c)+1)

        break

    end

    Actual_Print  =  [Gkey(1);'  X';co_x_order(i);'  Y';co_y_order(i);'
E';E_order_revised(i-1);Gdef(1);];

    fprintf(fid,'%1s    %6s    %6s    %6s    %6s    %6s    %6s    %12s
\r\n',Actual_Print); %printing line

    totale    =    totale    +    (e*(sqrt(((co_x_order(i)-co_x_order(i-
1))^2)+((co_y_order(i)-co_y_order(i-1))^2))));

    move     =     move     +     ((sqrt(((co_x_order(i)-co_x_order(i-
1))^2)+((co_y_order(i)-co_y_order(i-1))^2))));

    if co_y_order(i-1)>co_y_order(i)

        n_coord = co_y_order(i)+3;

    else

        n_coord = co_y_order(i)-3;

    end

    Retract = [Gkey(1);' F8640';' Y';n_coord;' E-0.76';Gkey(1);' E-0.04';'
F2100';Gkey(1);' Z';lh+0.6;' F10800';' ;Retract';];

    fprintf(fid,'%1s %3s %3s %3s %3s %3s %3s %3s %3s %3s %3s %3s %12s
\r\n',Retract); %Printing retraction commands

    i = i + 1;

end
```

%Returns the total movement of the extruder to the main/base workspace.

```
assignin('base', 'totale', totale);
```

%Returns the total movement of the extruder head to the main/base workspace.

```
assignin('base','move', move);
```

%Returns the e factor to the main/base workspace. For calculating the road width.

```
assignin('base', 'e', e);
%%
```

%resetting the extruder head

```
nozzle = [Gkey(1);' E';'-1.0';Gdef(1);Gkey(1);' E';;'1.0';Gdef(1);];
```

%Prints the resetting of the extruded material.

```
fprintf(fid,'%1s %6s %6s %12s \r\n',nozzle);
```

A.3.3 onelayer-zero

```
function [] = onelayer_zero(bed_x,bed_y,w,d,gap,offset_x,offset_y,fid,e,layerheight)
%Original concept developed by Hazel Mitchell
%Plots GCode for rectangle or square shape
%all units are in mm
%%
%Meaning of the input variables
% bed_x = width of the bed/dimension in the x direction
% bed_y = depth of the bed/dimension in the y direction
```

```
% w = width of your part

% d = depth of your part See 'cube pic.jpg' for a better visualisation

% gap = gap between the printed lines

% offset_x = offset of the layer from the origin in the x direction

% offset_y = offset of the layer from the origin in the y direction

% fid = variable that opens/creates the file you request to write the

% gcode to

% e = e factor value which controls the thickness of the printed line

% layerheight = layer height, used to determine if the initial purging
line

% is required at this height.


%%

%Derived values

F_speed = (e - 0.0920216)/(-0.000027156);


%%

%%drawing your shape

xlimit = [(((bed_x/2)-(w/2))) (((bed_x/2)+(w/2)))];

ylimit = [(((bed_y/2)-(d/2))) (((bed_y/2)+(d/2)))];

xbox = xlimit([1 1 2 2 1]);

ybox = ylimit([1 2 2 1 1]);

%mapshow(xbox,ybox,'DisplayType','polygon','LineStyle','none')

xlimit(2);

ylimit(1);

%%

%finding the coordinates
```

```
a = min((floor((w*2)/gap)),(floor((d*2)/gap)));

x = zeros(1, a); %setting up the initial matrices

y = zeros(1, a);%setting up the initial matrices

i = 2;

for a = (((bed_y/2)-(d/2)))-gap:-gap:0

    x(i) = 0; %Start of line

    y(i) = a; %Start of line

    i = i + 1;

    x(i) = bed_x; %End of line

    y(i) = a; %End of line

    i = i + 1;

    x(i) = NaN; %Skips a line

    y(i) = NaN; %Skips a line

    i = i + 1;

end

for a = (((bed_y/2)-(d/2))):gap:bed_y

    x(i) = 0; %Start of line

    y(i) = a; %Start of line

    i = i + 1;

    x(i) = bed_x; %End of line

    y(i) = a; %End of line

    i = i + 1;

    x(i) = NaN; %Skips a line

    y(i) = NaN; %Skips a line

    i = i + 1;

end

if (rem(d,gap)) == 0
```

```
    %do nothing

else

    x(i) = (((bed_x/2)-(w/2)));

    y(i) = (((bed_y/2)+(d/2)));

    i = i + 1;

    x(i) = (((bed_x/2)+(w/2)));

    y(i) = (((bed_y/2)+(d/2)));

end



%mapshow(x,y,'Marker','+') %showing the start and end points of line the
lines

[xi,yi,ii] = polyxpoly(x,y,xbox,ybox); %finding the intersection of the
lines and the box



%mapshow(xi,yi,'DisplayType','point','Marker','o')

ii = ii(:,1);

xi(numel(xi)) = [];

yi(numel(yi)) = [];

ii(numel(ii)) = [];

co_x = zeros(1, (numel(xi))); %zeros matrix for unordered x coordinates

co_y = zeros(1, (numel(yi))); %zeros matrix for unordered y coordinates

num = zeros(1, (numel(ii)));

% co_x(1) = xlimit(2); %initial x coordinate

% co_y(1) = ylimit(1); %initial y coordinate

% num(1)  = (min(ii)-1);

for i = 1:(numel(xi))

    co_x(i) = xi((i)) + offset_x;

    co_y(i) = yi((i)) + offset_y;
```

```
    if i == (numel(xi))+1

        break;

    end

    num(i) = ii((i));

end

%num(numel(num)) = ii((numel(ii)))+1;

co_x_order = zeros(1, (numel(xi))); %zeros matrix for ordered matrix for
x coorindates

co_y_order = zeros(1, (numel(yi))); %zeros matrix for ordered matrix for
y coorindates

[b,c] = sort(num,2); %#ok<ASGLU> %b is an array of the sorted values of
the num matrix, c is an array of the original indexing for the sorted
array. Tells us which order to have stuff in.

i = 1;

for j = 1:(numel(c))/4+1

    co_x_order(i) = co_x((c(i)));

    co_y_order(i) = co_y((c(i))); %1

    i = i + 1;

    if i == numel(c)

        break;

    end

    co_x_order(i) = co_x((c(i)));

    co_y_order(i) = co_y((c(i))); %2

    i = i + 1;

    if i == numel(c)

        break;

    end

    co_x_order(i) = co_x((c(i+1)));

    co_y_order(i) = co_y((c(i+1))); %3
```

```
    i = i + 1;

    if i == numel(c)

        break;

    end

    co_x_order(i) = co_x((c(i-1)));

    co_y_order(i) = co_y((c(i-1))); %4

    i = i + 1;

    if i == numel(c)

        break;

    end

end

co_x_order(i) = co_x((c(i)));

co_y_order(i) = co_y((c(i)));

%%

%Extruder value calculation

E_order = zeros(1, (numel(xi))); %new empty matrix for extruder movement
coordinates

for i = 2:numel(c)

    E_order(i-1)          =          e*(sqrt(((co_x_order(i)-co_x_order(i-
1))^2)+((co_y_order(i)-co_y_order(i-1))^2)));    %Adding    the    extruder
movement values to the matrix

    i = i + 1;

end

E_order_revised = zeros (1, (numel(xi))); %new empty matrix for extruder
movement coordinates without excess movement.

for i = 2:numel(c)

    if rem(i-1,2) == 0

        E_order_revised(i-1) = 0;

    else
```

```
        E_order_revised(i-1) = E_order(i-1);
    end
end
```

```
%%
%Initial movement of the printer head
global totale; %Global variable defined in pattern function to calculate the total movement of the extruder for material use and time calculation in material properties function.
global lh; %Global variable defined in pattern function to determine the actual layer height of the print. Used when moving in the Z direction.
global move; %Global variable defined in pattern function to determine the movement of the extruder head.

Gkey = ["G1", "G1 X100 E12.5 F1000", "G1 X113 Y105", "G1 X60 E9 F1000", "G1 Y-3 F1000", "G21", "G28 W", "G80", "G90", "G91", "G92", "G92 E0"]; % Array of all the G codes to be used.
Gdef = [" ; Linear Movement", " ; Initial thicker line to clear extruder", " ; Move extruder to middle of the bed", " ; Initial thinner line to clear extruder", " ; Extruder goes outside the print area", " ; Sets units to mm", " ; Homes all axis (W=without mesh bed level)", " ; Mesh bed levelling", " ; Sets coordinates such that they are defined from the origin of the bed", " ; Sets coordinates such that they are defined relative to each other", " ; Resets axis position to 0", ";Resets extruder position to 0"]; % Array of the definitions of the corresponding G code in the previous array.
Reset = [Gkey(1);' Z';lh + 0.6;' E';'-0.8';Gdef(1); Gkey(1);' X';co_x_order(1);' Y';co_y_order(1);Gdef(1);Gkey(1);' Z';lh;' E';'0.8';Gdef(1);Gkey(12);'';'';'';'';Gdef(12);Gkey(1);' F';F_speed;'';'';Gdef(1);]; % Resets the position of the extruder head to the starting point of the track it will take.
fprintf(fid,'%1s %6s %6s %6s %6s %12s \r\n',Reset); %Prints the extruder position reset commands in the gcode script.
```

```
%%

%Actual movement

i = 2;

%Purging line

if lh == layerheight

    Purging   =   [Gkey(1);'   X';co_x_order(2);'   Y';co_y_order(2)-10;'
E';0;Gdef(1);

               Gkey(1);'    X';co_x_order(2)+25;'    Y';co_y_order(2)-10;'
E';e*25;Gdef(1);

               Gkey(1);'       X';co_x_order(1);'       Y';co_y_order(1);'
E';e*(sqrt((((co_x_order(2)+25)-co_x_order(1))^2)+(((co_y_order(2)-10)-
co_y_order(1))^2)));Gdef(1);];

    fprintf(fid,'%1s %6s %6s %6s %6s %6s %6s %12s \r\n',Purging);%Printing
the purging line

end



%Printing the scaffold

while i < (numel(c)+1)

    Actual_Print   =   [Gkey(1);'   X';co_x_order(i);'   Y';co_y_order(i);'
E';E_order_revised(i-1);Gdef(1);];

    fprintf(fid,'%1s     %6s     %6s     %6s     %6s     %6s     %6s     %12s
\r\n',Actual_Print); %printing line

    totale     =     totale     +     (e*(sqrt(((co_x_order(i)-co_x_order(i-
1))^2)+((co_y_order(i)-co_y_order(i-1))^2))));

    move      =      move      +      ((sqrt(((co_x_order(i)-co_x_order(i-
1))^2)+((co_y_order(i)-co_y_order(i-1))^2))));

    if i == 2

        n_coord = co_x_order(i)+5;

    elseif co_y_order(i-1)>co_x_order(i)

        n_coord = co_x_order(i)-5;
```

```
    else

        n_coord = co_x_order(i)+5;

    end

    Retract = [Gkey(1);' F8640';' X';n_coord;' E-0.76';Gkey(1);' E-0.04';'
F2100';Gkey(1);' Z';lh+0.6;' F10800';' ;Retract';];

    fprintf(fid,'%1s %3s %3s %3s %3s %3s %3s %3s %3s %3s %3s %3s %12s
\r\n',Retract); %Printing retraction commands

    i = i + 1;

    if i == (numel(c)+1)

        break

    end

    Actual_Print  =  [Gkey(1);'  X';co_x_order(i);'  Y';co_y_order(i);'
E';E_order_revised(i-1);Gdef(1);];

    fprintf(fid,'%1s    %6s    %6s    %6s    %6s    %6s    %6s    %12s
\r\n',Actual_Print); %printing line

    totale    =    totale    +    (e*(sqrt(((co_x_order(i)-co_x_order(i-
1))^2)+((co_y_order(i)-co_y_order(i-1))^2))));

    move     =     move     +     ((sqrt(((co_x_order(i)-co_x_order(i-
1))^2)+((co_y_order(i)-co_y_order(i-1))^2))));

    Reposition  =  [Gkey(1);'  Z';lh;Gkey(1);'  E0.8';'  F2100';Gkey(1);'
F';F_speed;' ;Reposition';];

    fprintf(fid,'%1s  %3s  %3s  %3s  %3s  %3s  %3s  %3s  %3s  %3s  %12s
\r\n',Reposition); %Printing reposition commands

    NP = [''];];

    fprintf(fid,'%1s \r\n',NP); %New line

    i = i + 1;

end

assignin('base', 'totale', totale); %Returns the total movement of the
extruder to the main/base workspace.

assignin('base','move', move); %Returns the total movement of the extruder
head to the main/base workspace.
```

```
assignin('base', 'e', e); %Returns the e factor to the main/base workspace.
For calculating the road width.

%%

%resetting the extruder head

nozzle = [Gkey(1);' E';'-1.0';Gdef(1);Gkey(1);' E';'1.8';Gdef(1);];

fprintf(fid,'%1s %6s %6s %12s \r\n',nozzle); %Prints the resetting of the
extruded material.
```

Appendix B Young's Modulus Calculator

Author: Maria Stagno-Navarra

```
%%

%Sample name and data

%filename = 'Specimen_RawData_3.csv'; %Filename of data you want to analyse

Area = 669.77; %Surface area of face in contact with the cross head

Height = 24.68; %Height of the cube in the dimension that is reducing due to be being compressed

samplename = 'LHL, gradient, sample 1'; %Name you want to give to the sample. This will make the title of the graph produced and the row heading for the excel data file

graphname = 'LHL, gradient, sample_one'; %Name you want to give to the graphs that save. It can't contain numbers.

number = 14; %Sample number that you're analysing


%%

%Initialising the data file that you save res+ults to

M = ["Sample Name","Youngs Modulus (MPa)","R Squared","Yield Stress (MPa)","Yield Strain"]; %Matrix to create titles of the columns in excel


name = 'testdata_results_LHLgradient_one.xlsx'; %filename for file which you are saving the Young's modulus data to.

%writematrix(M,name,'Sheet',1,'Range','A1:E1');%Writing the column names in the excel file


%%
```

```
%Plotting the data to decide the linear region

A = SpecimenRawData3; %Reading the file and making it into an array

A(1:6,:) = []; %Removing the unnecessary data

%A = array2table(A); %Converting the array into a table

A.Properties.VariableNames = {'Time' 'Extension' 'Load'}; %Adding labels
to the columns

A.Properties.VariableUnits = {'s' 'mm' 'N'}; %Adding units ot the columnns

A.Extension = A.Extension/Area; %- ((T.Load-0)/77117.45859);

figure(1);%Calling the first plot the first figure so the graphs will be
plotted in different figures

plot(A.Extension, A.Load); %Plotting graph so you can visually see roughly
where the linear region beings



%%

%Determining the middle window - this will require some manual input

%(though this does make it partially subjective the minimal affect that

%this subjectiveness has is appropriate given that the other alternative

%would require more computing time and power.

EX = 0.0047; %Value for extension which roughly indicates the middle of
the linear region

middle = dsearchn(A.Extension,EX); %Finding the coordinate which is closest
to your rough estimation of the middle

Tnew_1 = table; %Creation of new table which will calculate the upper yield
limit

Tnew_2 = table; %Creation of new table which will calculate the beginning
point of the linear region

j = 1; %Counter variable

k = 1; %Counter variable

for c = middle-100:middle+100
```

```
    Tnew_1(j,:) = A(c,{'Extension', 'Load'}); %Copying the data points from
the original file to create your initial window

    j = j + 1;

end

for c = middle-100:middle+100 %Copying the data points from the original
file to create your initial window

    Tnew_2(k,:) = A(c,{'Extension', 'Load'});

    k = k + 1;

end

%%

%Calculting the upper bound of the linear region

Rsq = 0.99; %Initial Rsquared value to start at.

lim_R = 0.995; %Rsquared value where you cut-off the data

for i = middle+100:25:height(A) %Loop which calculates when the data
exceeds the yield point

    Tnew_1(j,:) = A(i,{'Extension','Load'});

    mdl_1 = fitlm(Tnew_1.Extension,Tnew_1.Load);

    Rsq = mdl_1.Rsquared.Ordinary;

    j = j + 1;

    if Rsq < lim_R

        break;

    end

end

Upper_Yield = Tnew_1{height(Tnew_1),{'Extension'}};%Value of extension
which is the upper yield point

Upper = dsearchn(A.Extension,Upper_Yield); %Index value which corresponds
to the upper yield

hold on %Allows you to plot on the previous graph

mdl_1.plot %Plots the data onto a graph
```

```
%%

%Calculating the lower bound of linear region

lim_R_1 = 0.995;

for i = middle-100:-25:1  %Loop which calculates when the data exceeds the
yield point

    Tnew_2(k,:) = A(i,{'Extension','Load'});

    mdl = fitlm(Tnew_2.Extension,Tnew_2.Load);

    Rsq = mdl.Rsquared.Ordinary;

    k = k + 1;

    if Rsq < lim_R_1

        break;

    end

end

Lower_Yield = Tnew_2{height(Tnew_2),{'Extension'}}; %Value of extension
which is the initial value of the linear region

Lower = dsearchn(A.Extension,Lower_Yield); %Index value which corresponds
to the initial value of the linear region

hold on %Allows you to plot on the previous graph

mdl.plot %Plots the data onto a graph



%%

%Calculating stress vs strain

Strain_S = A{Lower,2}; %Initial value at which the graph should be at 0
strain

Stress_S = A{Lower,3}; %Initial value at which the graph should be at 0
stress

A.Strain = (A.Extension - Strain_S)/Height; %Calculation of strain

A.Properties.VariableUnits{'Strain'} = 'mm/mm';
```

```
A.Stress = (A.Load - Stress_S)/Area; %Calculation of stress

A.Properties.VariableUnits{'Stress'} = 'MPa';



%%

%Calculating Young's Modulus

Tnew_3 = table; %Creation of new table which will plot the relevent stress vs strain and therefore calculate YOung's modulus

j = 1;

for i = Lower:1:Upper %Copying relevant stress and strain data

    Tnew_3(j,:) = A(i,{'Strain','Stress'});

    j = j + 1;

end

mdl_Y = fitlm(Tnew_3.Strain,Tnew_3.Stress); %Linear fit to the copied data

figure(2); %Plot a near graph which will show you stress vs strain and where you took your Young's modulus from

plot(A.Strain,A.Stress); %Plotting Stress vs Strain

hold on; %Allow you to plot on previous graph

mdl_Y.plot; %Plotting data for Young's modulus

title(samplename); %Naming graph

xlabel('Strain'); %Adding axis name

ylabel('Stress (MPa)'); %Adding axis name



Youngs = string(num2str(mdl_Y.Coefficients{2,1})); %Extracting the relevant value for Young's modulus in the format required for writing to the excel file

RSQ = string(num2str(mdl_Y.Rsquared.Ordinary)); %Extracting the relevant R squared value in the format required for writing to the excel file

YSTRESS = string(num2str(A{Upper,{'Stress'}}));

YSTRAIN = string(num2str(A{Upper,{'Strain'}}));
```

```
%%

%Presenting the data in an easy format

i = num2str(number+1); %samplenumber + 1

R = strcat('A',i,':','E',i); %Creating a string which dictactes where the
data will be written

D = [samplename,Youngs,RSQ,YSTRESS,YSTRAIN]; %Matrix with tha relevant
data

writematrix(D,name); %Writing the relevant data to the excel file

saveas(gcf,graphname,'fig');

saveas(gcf,graphname,'png');

ans_1 = convertCharsToStrings(graphname);

str = strcat(ans_1,".xlsx");

str = char(str);

writetable(A,str);
```

List of References

1. Kinaci, A., Neuhaus, V. & Ring, D. C. Trends in Bone Graft Use in the United States. *Orthopedics* **37**, e783–e788 (2014).

2. Sobral, J. M., Caridade, S. G., Sousa, R. A., Mano, J. F. & Reis, R. L. Three-dimensional plotted scaffolds with controlled pore size gradients: Effect of scaffold geometry on mechanical performance and cell seeding efficiency. *Acta Biomater.* **7**, 1009–1018 (2011).

3. Giannoudis, P. V., Dinopoulos, H. & Tsiridis, E. Bone substitutes: An update. *Injury* **36**, S20–S27 (2005).

4. Di Luca, A. *et al.* Gradients in pore size enhance the osteogenic differentiation of human mesenchymal stromal cells in three-dimensional scaffolds. *Sci. Rep.* **6**, (2016).

5. Lakes, R. Materials with structural hierarchy. *Nature* **361**, 511–515 (1993).

6. Paredes, C., Martínez-Vázquez, F. J., Pajares, A. & Miranda, P. Development by robocasting and mechanical characterization of hybrid HA/PCL coaxial scaffolds for biomedical applications. *J. Eur. Ceram. Soc.* **39**, 4375–4383 (2019).

7. Paredes, C., Martínez-Vázquez, F. J., Pajares, A. & Miranda, P. Novel strategy for toughening robocast bioceramic scaffolds using polymeric cores. *Ceram. Int.* **45**, 19572–19576 (2019).

8. Hutmacher, D. W. Sca!olds in tissue engineering bone and cartilage. 15 (2000).

9. Ziminska, M., Dunne, N. & Hamilton, A. R. Porous Materials with Tunable Structure and Mechanical Properties via Templated Layer-by-Layer Assembly. *ACS Appl. Mater. Interfaces* **8**, 21968–21973 (2016).

10. Amin Yavari, S. *et al.* Layer by layer coating for bio-functionalization of additively manufactured meta-biomaterials. *Addit. Manuf.* **32**, 100991 (2020).

11. Yang, S., Leong, K.-F., Du, Z. & Chua, C.-K. The Design of Scaffolds for Use in Tissue Engineering. Part I. Traditional Factors. *Tissue Eng.* **7**, 679–689 (2001).

12. Polo-Corrales, L., Latorre-Esteves, M. & Ramirez-Vick, J. E. Scaffold Design for Bone Regeneration. *J. Nanosci. Nanotechnol.* **14**, 15–56 (2014).

13. Baptista, R. & Guedes, M. Morphological and mechanical characterization of 3D printed PLA scaffolds with controlled porosity for trabecular bone tissue replacement. *Mater. Sci. Eng. C* **118**, 111528 (2021).

14. Flemming, R. G., Murphy, C. J., Abrams, G. A., Goodman, S. L. & Nealey, P. F. Effects of synthetic micro- and nano-structured surfaces on cell behavior. *Biomaterials* **20**, 573–588 (1999).

15. Desai, T. A. Micro- and nanoscale structures for tissue engineering constructs. *Med. Eng. Phys.* **22**, 595–606 (2000).

16. Khaliq, M. H. *et al.* On the use of high viscosity polymers in the fused filament fabrication process. *Rapid Prototyp. J.* **23**, 727–735 (2017).

17. Papon, E. A. & Haque, A. Review on process model, structure-property relationship of composites and future needs in fused filament fabrication. *J. Reinf. Plast. Compos.* **39**, 758–789 (2020).

18. Abbott, A. C., Tandon, G. P., Bradford, R. L., Koerner, H. & Baur, J. W. Process-structure-property effects on ABS bond strength in fused filament fabrication. *Addit. Manuf.* **19**, 29–38 (2018).

19. Naghieh, S., Karamooz Ravari, M. R., Badrossamay, M., Foroozmehr, E. & Kadkhodaei, M. Numerical investigation of the mechanical properties of the additive manufactured bone scaffolds fabricated by FDM: The effect of layer penetration and post-heating. *J. Mech. Behav. Biomed. Mater.* **59**, 241–250 (2016).

20. Sood, A. K., Ohdar, R. K. & Mahapatra, S. S. Parametric appraisal of mechanical property of fused deposition modelling processed parts. *Mater. Des.* **31**, 287–295 (2010).

21. Casavola, Cazzato, Moramarco, & Renna. Mechanical Behaviour of ABS-Fused Filament Fabrication Compounds under Impact Tensile Loadings. *Materials* **12**, 1295 (2019).

22. Robinson, R., A. Physicochemical Structure of Bone. *Clin. Orthop.* **112**, 263–315 (1975).

23. Liu, X. S. *et al.* Complete Volumetric Decomposition of Individual Trabecular Plates and Rods and Its Morphological Correlations With Anisotropic Elastic Moduli in Human Trabecular Bone. *J. Bone Miner. Res.* **23**, 223–235 (2007).

24. Wilson-Hench, J. Osteoinduction. *Prog. Biomed. Eng.* **4**, 29.

25. Gong, J. K., Arnold, J. S. & Cohn, S. H. Composition of trabecular and cortical bone. *Anat. Rec.* **149**, 325–331 (1964).

26. Morgan, E. F. & Keaveny, T. M. Dependence of yield strain of human trabecular bone on anatomic site. *J. Biomech.* **34**, 569–577 (2001).

27. Mirzaali, M. J. *et al.* Mechanical properties of cortical bone and their relationships with age, gender, composition and microindentation properties in the elderly. *Bone* **93**, 196–211 (2016).

28. Dong, X. N., Acuna, R. L., Luo, Q. & Wang, X. Orientation dependence of progressive post-yield behavior of human cortical bone in compression. *J. Biomech.* **45**, 2829–2834 (2012).

29. Goldstein, S. A., Wilson, D. L., Sonstegard, D. A. & Matthews, L. S. The mechanical properties of human tibial trabecular bone as a function of metaphyseal location. *J. Biomech.* **16**, 965–969 (1983).

30. Ciarelli, M. J., Goldstein, S. A., Kuhn, J. L., Cody, D. D. & Brown, M. B. Evaluation of orthogonal mechanical properties and density of human trabecular bone from the major metaphyseal regions with materials testing and computed tomography. *J. Orthop. Res.* **9**, 674–682 (1991).

31. Keaveny, T. M., Wachtel, E. F., Ford, C. M. & Hayes, W. C. Differences between the tensile and compressive strengths of bovine tibial trabecular bone depend on modulus. *J. Biomech.* **27**, 1137–1146 (1994).

32. Hernandez, C. J. Chapter A2 Cancellous Bone. in *Handbook of Biomaterial Properties* (eds. Murphy, W., Black, J. & Hastings, G.) 15–21 (Springer New York, 2016). doi:10.1007/978-1-4939-3305-1_2.

33. Sfeir, C., Ho, L., Doll, B. A., Azari, K. & Hollinger, J. O. Fracture Repair. in *Bone Regeneration and Repair* (eds. Lieberman, J. R. & Friedlaender, G. E.) 21–44 (Humana Press, 2005). doi:10.1385/1-59259-863-3:021.

34. Schmidt-Bleek, K., Kwee, B. J., Mooney, D. J. & Duda, G. N. Boon and Bane of Inflammation in Bone Tissue Regeneration and Its Link with Angiogenesis. *Tissue Eng. Part B Rev.* **21**, 354–364 (2015).

35. Weinkamer, R., Eberl, C. & Fratzl, P. Mechanoregulation of Bone Remodeling and Healing as Inspiration for Self-Repair in Materials. *Biomimetics* **4**, 46 (2019).

36. Baker, C. E. *et al.* Bone Fracture Acute Phase Response—A Unifying Theory of Fracture Repair: Clinical and Scientific Implications. *Clin. Rev. Bone Miner. Metab.* **16**, 142–158 (2018).

37. Palomares, K. T. S. *et al.* Mechanical stimulation alters tissue differentiation and molecular expression during bone healing: STIMULATION ALTERS SKELETAL TISSUE DIFFERENTIATION. *J. Orthop. Res.* **27**, 1123–1132 (2009).

38. Bayraktar, H. H. *et al.* Comparison of the elastic and yield properties of human femoral trabecular and cortical bone tissue. *J. Biomech.* **37**, 27–35 (2004).

39. Torres, A. M. *et al.* Material heterogeneity in cancellous bone promotes deformation recovery after mechanical failure. *Proc. Natl. Acad. Sci.* **113**, 2892–2897 (2016).

40. Wang, W. & Yeung, K. W. K. Bone grafts and biomaterials substitutes for bone defect repair: A review. *Bioact. Mater.* **2**, 224–247 (2017).

41. Ge, J. *et al.* The Size of Mesenchymal Stem Cells is a Significant Cause of Vascular Obstructions and Stroke. *Stem Cell Rev. Rep.* **10**, 295–303 (2014).

42. Shibuya, N. & Jupiter, D. C. Bone Graft Substitute. *Clin. Podiatr. Med. Surg.* **32**, 21–34 (2015).

43. Itälä, A. I., Ylänen, H. O., Ekholm, C., Karlsson, K. H. & Aro, H. T. Pore diameter of more than 100 μm is not requisite for bone ingrowth in rabbits: Optimum Pore Size for New Bone Ingrowth. *J. Biomed. Mater. Res.* **58**, 679–683 (2001).

44. Karageorgiou, V. & Kaplan, D. Porosity of 3D biomaterial scaffolds and osteogenesis. *Biomaterials* **26**, 5474–5491 (2005).

45. Grémare, A. *et al.* Characterization of printed PLA scaffolds for bone tissue engineering: CHARACTERIZATION OF PRINTED PLA SCAFFOLDS. *J. Biomed. Mater. Res. A* **106**, 887–894 (2018).

46. Gregor, A. *et al.* Designing of PLA scaffolds for bone tissue replacement fabricated by ordinary commercial 3D printer. *J. Biol. Eng.* **11**, (2017).

47. Cavo, M. & Scaglione, S. Scaffold microstructure effects on functional and mechanical performance: Integration of theoretical and experimental approaches for bone tissue engineering applications. *Mater. Sci. Eng. C* **68**, 872–879 (2016).

48. Hutmacher, D. W. *et al.* Mechanical properties and cell cultural response of polycaprolactone scaffolds designed and fabricated via fused deposition modeling. *J. Biomed. Mater. Res.* **55**, 203–216 (2001).

49. Elomaa, L. *et al.* Preparation of poly(ε-caprolactone)-based tissue engineering scaffolds by stereolithography. *Acta Biomater.* **7**, 3850–3856 (2011).

50. Clarke, P. D. R. Cambridge Solid State Science Series. *B A* 524.

51. Bobbert, F. S. L. *et al.* Additively manufactured metallic porous biomaterials based on minimal surfaces: A unique combination of topological, mechanical, and mass transport properties. *Acta Biomater.* **53**, 572–584 (2017).

52. Rider, P. *et al.* Additive Manufacturing for Guided Bone Regeneration: A Perspective for Alveolar Ridge Augmentation. *Int. J. Mol. Sci.* **19**, 3308 (2018).

53. Kawai, T. *et al.* Customized, degradable, functionally graded scaffold for potential treatment of early stage osteonecrosis of the femoral head: TREATMENT OF EARLY STAGE OSTEONECROSIS OF THE FEMORAL HEAD. *J. Orthop. Res.* **36**, 1002–1011 (2018).

54. Zwingenberger, S. *et al.* Recommendations and Considerations for the Use of Biologics in Orthopedic Surgery. 12 (2012).

55. Williams, D. F. There is no such thing as a biocompatible material. *Biomaterials* **35**, 10009–10014 (2014).

56. Mondschein, R. J., Kanitkar, A., Williams, C. B., Verbridge, S. S. & Long, T. E. Polymer structure-property requirements for stereolithographic 3D printing of soft tissue engineering scaffolds. *Biomaterials* **140**, 170–188 (2017).

57. Morris, V. B., Nimbalkar, S., Younesi, M., McClellan, P. & Akkus, O. Mechanical Properties, Cytocompatibility and Manufacturability of Chitosan:PEGDA Hybrid-Gel Scaffolds by Stereolithography. *Ann. Biomed. Eng.* **45**, 286–296 (2017).

58. Eshraghi, S. & Das, S. Mechanical and microstructural properties of polycaprolactone scaffolds with one-dimensional, two-dimensional, and three-dimensional orthogonally oriented porous architectures produced by selective laser sintering. *Acta Biomater.* **6**, 2467–2476 (2010).

59. Kruth, J. P., Wang, X., Laoui, T. & Froyen, L. Lasers and materials in selective laser sintering. *Assem. Autom.* **23**, 357–371 (2003).

60. Hassanajili, S., Karami-Pour, A., Oryan, A. & Talaei-Khozani, T. Preparation and characterization of PLA/PCL/HA composite scaffolds using indirect 3D printing for bone tissue engineering. *Mater. Sci. Eng. C* **104**, 109960 (2019).

61. Andani, M. T. *et al.* Metals for bone implants. Part 1. Powder metallurgy and implant rendering. *Acta Biomater.* **10**, 4058–4070 (2014).

62. Ravichandran, A. *et al.* In vitro cyclic compressive loads potentiate early osteogenic events in engineered bone tissue. *J. Biomed. Mater. Res. B Appl. Biomater.* **105**, 2366–2375 (2017).

63. Moroni, L. *et al.* Biofabrication: A Guide to Technology and Terminology. *Trends Biotechnol.* **36**, 384–402 (2018).

64. Gibson, L. J. & Ertsoni, C. I. R. The Mechanics of Two-Dimensional Cellular Materials. 19 (2020).

65. The mechanics of three-dimensional cellular materials. 19.

66. Hendrikson, Wim. J., van Blitterswijk, Clemens. A., Rouwkema, J. & Moroni, L. The Use of Finite Element Analyses to Design and Fabricate Three-Dimensional Scaffolds for Skeletal Tissue Engineering. *Front. Bioeng. Biotechnol.* **5**, 30 (2017).

67. Truscello, S. *et al.* Prediction of permeability of regular scaffolds for skeletal tissue engineering: A combined computational and experimental study. *Acta Biomater.* **8**, 1648–1658 (2012).

68. Cuan-Urquizo, E., Shalchy, F. & Bhaskar, A. Compressive stiffness of staggered woodpile lattices: Mechanics, measurement, and scaling laws. *Int. J. Mech. Sci.* **187**, 105932 (2020).

69. Norato, J. A. & Wagoner Johnson, A. J. A Computational and Cellular Solids Approach to the Stiffness-Based Design of Bone Scaffolds. *J. Biomech. Eng.* **133**, 091003 (2011).

70. McKown, S. *et al.* The quasi-static and blast loading response of lattice structures. *Int. J. Impact Eng.* **35**, 795–810 (2008).

71. Karamooz Ravari, M. R., Kadkhodaei, M., Badrossamay, M. & Rezaei, R. Numerical investigation on mechanical properties of cellular lattice structures fabricated by fused deposition modeling. *Int. J. Mech. Sci.* **88**, 154–161 (2014).

72. Rodríguez, J. F., Thomas, J. P. & Renaud, J. E. Mechanical behavior of acrylonitrile butadiene styrene (ABS) fused deposition materials. Experimental investigation. *Rapid Prototyp. J.* **7**, 148–158 (2001).

73. Kuznetsov, V. E., Solonin, A. N., Urzhumtsev, O. D., Schilling, R. & Tavitov, A. G. Strength of PLA Components Fabricated with Fused Deposition Technology Using a Desktop 3D Printer as a Function of Geometrical Parameters of the Process. 11 (2018).

74. Bellini, A. & Güçeri, S. Mechanical characterization of parts fabricated using fused deposition modeling. *Rapid Prototyp. J.* **9**, 252–264 (2003).

75. Coogan, T. J. & Kazmer, D. O. Modeling of interlayer contact and contact pressure during fused filament fabrication. *J. Rheol.* **63**, 655–672 (2019).

76. Montero, M., Roundy, S., Odell, D., Ahn, S.-H. & Wright, P. K. Material Characterization of Fused Deposition Modeling (FDM) ABS by Designed Experiments. 21 (2001).

77. Ahn, S., Montero, M., Odell, D., Roundy, S. & Wright, P. K. Anisotropic material properties of fused deposition modeling ABS. *Rapid Prototyp. J.* **8**, 248–257 (2002).

78. Zhang, J. Numerical investigation of the influence of process conditions on the temperature variation in fused deposition modeling. 10 (2017).

79. Faes, M., Ferraris, E. & Moens, D. Influence of Inter-layer Cooling time on the Quasi-static Properties of ABS Components Produced via Fused Deposition Modelling. *Procedia CIRP* **42**, 748–753 (2016).

80. Schindelin, J. *et al.* Fiji: an open-source platform for biological-image analysis. *Nat. Methods* **9**, 676–682 (2012).

81. Alizadeh-Osgouei, M., Li, Y., Vahid, A., Ataee, A. & Wen, C. High strength porous PLA gyroid scaffolds manufactured via fused deposition modeling for tissue-engineering applications. *Smart Mater. Med.* **2**, 15–25 (2021).

82. Ashby, M. F. & Medalist, R. F. M. The mechanical properties of cellular solids. *Metall. Trans. A* **14**, 1755–1769 (1983).

83. Jamshidian, M., Tehrany, E. A., Imran, M., Jacquot, M. & Desobry, S. Poly-Lactic Acid: Production, Applications, Nanocomposites, and Release Studies. *Compr. Rev. Food Sci. Food Saf.* **9**, 552–571 (2010).

84. Cuan-Urquizo, E. *et al.* Characterization of the Mechanical Properties of FFF Structures and Materials: A Review on the Experimental, Computational and Theoretical Approaches. *Materials* **12**, 895 (2019).

85. Gao, X. Fused filament fabrication of polymer materials: A review of interlayer bond. *Addit. Manuf.* 15 (2021).

86. Aid, S., Eddhahak, A., Ortega, Z., Froelich, D. & Tcharkhtchi, A. Predictive coalescence modeling of particles from different polymers: application to PVDF and PMMA pair. *J. Mater. Sci.* **52**, 11725–11736 (2017).

87. Naghieh, S., Karamooz Ravari, M. R., Badrossamay, M., Foroozmehr, E. & Kadkhodaei, M. Numerical investigation of the mechanical properties of the additive manufactured bone scaffolds fabricated by FDM: The effect of layer penetration and post-heating. *J. Mech. Behav. Biomed. Mater.* **59**, 241–250 (2016).

88. Carneiro, O. S., Silva, A. F. & Gomes, R. Fused deposition modeling with polypropylene. *Mater. Des.* **83**, 768–776 (2015).

89. González Díaz, E. C., Sinha, S., Avedian, R. S. & Yang, F. Tissue-engineered 3D models for elucidating primary and metastatic bone cancer progression. *Acta Biomater.* **99**, 18–32 (2019).

90. Ban, J., Fock, V., Aryee, D. N. T. & Kovar, H. Mechanisms, Diagnosis and Treatment of Bone Metastases. *Cells* **10**, 2944 (2021).

91. Valtanen, R. S., Yang, Y. P., Gurtner, G. C., Maloney, W. J. & Lowenberg, D. W. Synthetic and Bone tissue engineering graft substitutes: What is the future? *Injury* **52**, S72–S77 (2021).

92. Choi, W.-Y., Kim, H.-E., Moon, Y.-W., Shin, K.-H. & Koh, Y.-H. Production of porous Calcium Phosphate (CaP) ceramics with aligned pores using ceramic/camphene-based co-extrusion. *Biomater. Res.* **19**, 16 (2015).

93. Kabel, J., Odgaard, A., van Rietbergen, B. & Huiskes, R. Connectivity and the elastic properties of cancellous bone. *Bone* **24**, 115–120 (1999).

94. Arifvianto, B., Wirawan, Y. B., Salim, U. A., Suyitno, S. & Mahardika, M. Effects of extruder temperatures and raster orientations on mechanical properties of the FFF-processed polylactic-acid (PLA) material. *Rapid Prototyp. J.* **27**, 1761–1775 (2021).